HETE, the High Energy Transient Explorer: Unlocking the Mysteries of Gamma Ray Bursts

by

Glen Pickslay Monnelly

A.B. Physics, Princeton University (1996)

Submitted to the Department of Physics
in partial fulfillment of the requirements for the degree of

Doctor of Philosophy in Physics

at the

MASSACHUSETTS INSTITUTE OF TECHNOLOGY

September 2002

Author ..... Glen Monnelly .....
Department of Physics
July 11, 2002

Certified by ..... George R Ricker .....
George Ricker
Senior Research Scientist, Center for Space Research
Thesis Supervisor

Certified by ..... Saul Rappaport .....
Saul Rappaport
Professor of Physics
Thesis Supervisor

Accepted by ..... Thomas J. Greytak .....
Thomas J. Greytak
Chairman, Department Committee on Graduate Students

HETE, the High Energy Transient Explorer: Unlocking the Mysteries of Gamma Ray Bursts

by

Glen Pickslay Monnelly

Submitted to the Department of Physics
on July 11, 2002, in partial fulfillment of the
requirements for the degree of
Doctor of Philosophy in Physics

Abstract

The High Energy Transient Explorer (HETE), was built primarily at MIT and launched in October 2000 with the goal of studying Gamma Ray Bursts (GRBs) at X-ray and gamma-ray energies. A suite of instruments aboard HETE provide broadband sensitivity to GRBs: the French Gamma Telescope (FREGATE; 6 keV to $>$ 400 keV) instrument provides sensitive detections at gamma-ray energies, the Wide-Field X-Ray Monitor (WXM; 2 to 28 keV) provides detection and localization (5-10 $'$ radius) at X-ray energies, and the Soft X-ray Camera (SXC; 1.3 to 14 keV) provides refined localization ($<$ 1 $'$ radius) capabiities at soft X-ray energies. GRB positions, determined in-flight, are promptly transmitted to the ground via the Burst Alert Network (BAN), and disseminated to interested observers for X-ray, optical, and radio follow-up observations. The HETE Operations center is located at MIT. This dissertation provides an overview of HETE with a particular focus on the building, testing, and performance of the SXC.

To date the WXM has localized 18 GRBs, which have among them a number of interesting properties. Six are X-ray rich, which are of particular interest because they are not as well studied as classical GRBs. Beginning with the discovery of an optical transient at z = 0.45 for GRB 010921, five WXM GRB localizations have led to the identification of an afterglow transient (GRB 010921, GRB 020124, GRB 020305, and GRB 020331 in optical; GRB 020127 in radio). Optical follow-up observations with the Magellan 6.5m Baade Telescope of GRB 011130, GRB 011212, and GRB 020331 are described, including the discovery of the host galaxy of GRB 020331. X-ray observations of GRB 011130 with the Chandra X-ray Observatory at two different epochs have not conclusively revealed an X-ray counterpart among 61 detected X-ray point sources.

Thesis Supervisor: George Ricker
Title: Senior Research Scientist, Center for Space Research

Thesis Supervisor: Saul Rappaport
Title: Professor of Physics

Acknowledgments

The past five years at MIT have been an intense training in deeply scientific thought. At MIT, hard work doesn't rule alone; we learn and progress through creativity, rigorous thought, perseverance, confidence, perspective, experience, and above all collaboration and teamwork. The list goes on but the common theme of the MIT process is that the people you work with are the most important resource. I gratefully acknowledge every hallway conversation about science, every blackboard discussion about data analysis, every lunchtime argument about spacecraft operations, every cautionary tale offered at a science meeting, and every almost-too-long-to-read e-mail circulated to present a careful analysis of an important problem.

I thank my advisor George Ricker for providing the valuable opportunities I have had at MIT. George is the *HETE* principal investigator, and his leadership of the *HETE* team has been steady, determined, and inspired. In giving me a chance to face the challenges of building and operating *HETE*, he has given me the experience and confidence to meet any challenge my career may bring.

I thank my thesis committee members, Deepto Chakrabarty and Saul Rappaport, who is also my thesis co-supervisor. They have exemplified the value of the thesis committee by advising me at critical times and offering their wisdom to help me find the path to graduation.

The *HETE* mission is a broad international collaboration with a core group of dedicated people who have worked tirelessly to make the mission a success. I acknowledge the whole *HETE* team with special thanks to a number of people who have been coworkers and friends: Tye Brady, David Breslau, Nat Butler, Geoff Crew, Bob Dill, John Doty, Mike Doucette, Allyn Dullighan, Jean Farewell, Kelley Fischer, Rick Foster, Rosemary Hanlon, Garrett Jernigan, Al Levine, Fred Miller, Gregory Prighozin, Roland Vanderspek, and Joel Villasenor.

Beyond the *HETE* group I offer my appreciation to the Center for Space Research, which is full of people who were always generous to me with their time and energy. In particular, I thank Mark Bautz who was always right across the hall ready to

give advice or offer assistance, Mark Schattenburg who had so many big ideas about very tiny things and also Fred Baganoff, Dick Benford, Arlyn Hertz, Steve Kissel, Jimmy Marolda, Ed Murphy, Teresa Santiago, Ray Scuzzarella, and the Astrophysics Division Faculty.

I offer thanks to my fellow graduate students, who worked along side me in the trenches. Mike Pivovaroff, DJ of the office, whose advice was usually delivered with humor, but when I was done laughing I often had the urge to etch it in stone. Jon Miller who like a true friend never asked if I wanted his opinion, didn't sugar coat it when he gave it to me, and never stopped looking out for me. Michael Malm who vouched for me when it mattered. Duncan Galloway who teamed with me to solve most of the World's problems over countless cups of Toscinin's coffee or pints of beer. Bryan Gaensler who showed us all how to do it right. And a few others who shaped my graduate experience: Carl Chen, Froney Crawford, Derek Fox, Moly Hicks, Paul Konkola, Olivier Mongrard, Mike Muno, and Patrick Wojdowski.

I am deeply grateful to the friends who have been there along the way to share with me the joys of life. Rich Holland always made things more fun when he was around. My uncle Frank Monnelly was always a *HETE* fan and even tried to attend the launch. Ivy Ingram taught me how to breathe. Eric Emmons supplied our apartment with "old brownie". My life outside MIT has been very important to me, and it has been a pleasure to share good times with Allison Alessi, Blake Courter, Kirsten Hornby, Kristi Johnson, Beth Lauritsen, Catherine Mayotte, Maggie Partilla, Alec Randall, Eliza Richardson, Bryan Schenck, Yuri Stern, Jessica Stokes, and Jim Von der Heydt.

I close by acknowledging with deep gratitude and love my parents Dorothy and Ed, and my sister Anne for their unconditional and unwavering support. My mother was the center of so many wonderful family weekends in Ipswich. She fostered a strong family environment as she strove to preserve the the character of the natural environment while capturing its intrinsic beauty with her photography. My education has brought a world of experiences but I have yet to find a better role model than my father. I hope some of his ability to think clearly has rubbed off. My sister is an inspiration to me with her ability to apply caring, judgment, and wisdom to

make better everything she touches. My family has always provided a supportive foundation from which to grow, instilling values that have shaped and guided my life.

Contents

List of Figures

List of Tables

Chapter 1

Introduction

In the past five years, Gamma-Ray Bursts (GRB) have gone from being one of the biggest mysteries in astrophysics, to being the greatest success of multi-wavelength astronomy. After their discovery in 1969[1], for decades the most basic properties of GRBs were not known; theories placed their distance anywhere between the solar system and cosmological distances, estimates of their energy release showed comparable variation.

Following a string of recent discoveries in the past decade, our knowledge of GRBs has expanded rapidly. The BATSE instrument (Section 1.1) demonstrated that GRBs have an isotropic distribution on the sky, ruling out almost every model that does not place their origin at cosmological distances (Section 1.1.4). In 1997, *BeppoSAX* discovered and localized to arcminute accuracy a fading X-ray afterglow from GRB 970228 (Costa et al., 1997b), leading to discovery of fading optical afterglow (Galama et al., 1997) coincident with a galaxy. A few months later, a redshift of $z = 0.85$ was measured for the host galaxy of GRB 970508 (Metzger et al., 1997). These discoveries (Section 1.2) placed GRBs at cosmological distances, and led to estimates of total energies of $10^{51} - 10^{54}$ erg, suggesting that GRBs are the brightest explosions in the universe.

[1]GRBs were discovered by the VELA satellite (Klebesedal et al., 1973) in 1969. VELA was designed to detect $\sim$ MeV gamma-rays from nuclear explosions in space that violated the nuclear test ban treaty.

The true nature of GRBs remains a mystery, but a large body of evidence is beginning to address some fundamental questions. Recent results of Frail et al. (2001) suggests that GRBs have a constant "energy reservoir" of a few $\times 10^{51}$ erg and are beamed into $\sim$1/500 of the sky (Section 1.2.6). They are likely related to the death of a massive star and the formation of a black hole (Section 1.4); increasing evidence points to an association with supernova explosions (Section 1.3). This Chapter will describe our current state of knowledge of GRBs, and will show how the High Energy Transient Explorer (*HETE*) is addressing basic and important questions related to the nature of GRBs.

The *HETE* satellite, launched in October 2000, is the first satellite devoted to the study of GRBs. *HETE* detects and localizes GRBs using a broadband suite of instruments consisting of: the FREnch GAmma-ray Telescope (FREGATE; $6 - 400$ keV), the Wide-field X-ray Monitor (WXM; $2 - 25$ keV), and the Soft X-ray Camera (SXC; $1.3 - 14$ keV). Localizations are provided in near real-time via a network of Burst Alert Stations, allowing immediate followup of *HETE* GRBs. *HETE* is currently localizing GRBs at a rate of $\sim 15 - 20$ yr^{-1} with sufficient accuracy to allow optical, radio, and X-ray followup observations. An overview of *HETE* is presented in Chapter 2, including a description of the instrument suite, ground stations, mission operations, and a catalog of GRBs detected thus far. Chapter 3 focuses on the SXC design and performance, and Chapter 4 describes SXC imaging. Chapter 5 discusses optical follow-up observation of two *HETE* GRBs, GRB 011212 and GRB 020331. Chapter 6 discusses optical and X-ray follow-up observations of *HETE* GRB 011130.

1.1 Prompt emission

The prompt gamma-ray emission of GRBs shows great variability among the thousands of bursts that have been detected. The νF_ν spectrum typically peaks in the range of a few hundred keV. GRBs are as long as hundreds of seconds in duration, as short as 10 ms, and show variability on time-scales as short as 1 ms. Their lightcurves can be exceedingly complex, but often (about 25% of bursts) exhibit a

"fast-rise-exponential-decay" (FRED) behavior (Fishman & Meegan, 1995). A few representative examples are shown in Figure 1-1.

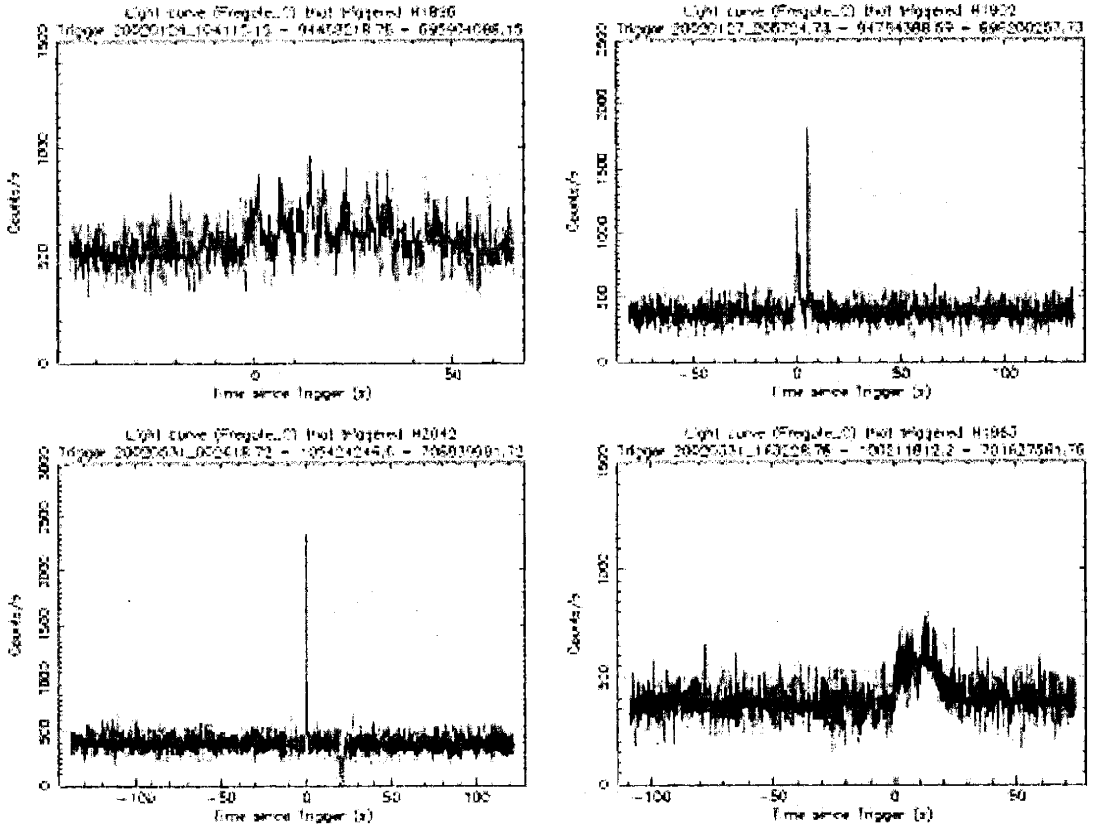

Figure 1-1: FREGATE GRB lightcurve examples. *Clockwise from top left:* GRB 020124 (H1896) shows multiple peaks over a $\sim 60s$ period. GRB 020127 (H1902) shows two sharp peaks. GRB 020531 (H2042) shows a single $\sim 200msec$ peak. GRB 020331 (H1963) shows a broad $\sim 25s$ peak.

The largest collection of GRB detections comes from the Burst and Transient Source Experiment (BATSE) instrument on the Compton Gamma-Ray Observatory (CGRO), which observed a large fraction of the sky continuously in the $25keV-2MeV$ band (Meegan et al., 1996). BATSE searches for count rate excesses, or "triggers", in the 50-300 keV count rate on 64, 256, are 1024 ms time-scales. BATSE detected about one GRB per day down to a limiting count rate of $0.5ph/$ cm ^{2}/s which corresponds to a sensitivity of about 10^{-7} erg/cm^2/s (Paciesas et al., 1999). Over its nine year mission, BATSE detected 2704 on-board triggered bursts. This large dataset provides

a detailed understanding of the characteristics of GRB prompt gamma-ray emission, which is described below.

1.1.1 Spectral characteristics

GRBs typically have a hard spectrum with a νF_ν peak between 50 and 300 keV (Preece et al., 2000). Empirically the data are well described by a so-called "Band spectrum" (Band et al., 1993), with a low-energy power-law index α, smoothly connected at a break energy to a high-energy power-law index β. Typical values are $\alpha \simeq -1$ and $\beta \simeq -2\ to\ -3$. The typical peak energy E_{peak} occurs near $\sim$ 200 keV, but this is close to the peak response energy of the instrument, drawing suspicion that it is an instrumental effect. Preece et al. (2000) make statistical arguments that the clustering is intrinsic, but Lloyd & Petrosian (1999) correct for instrumental effects and find the that true distribution of E_{peak} is flat from 100 keV to 1 MeV.

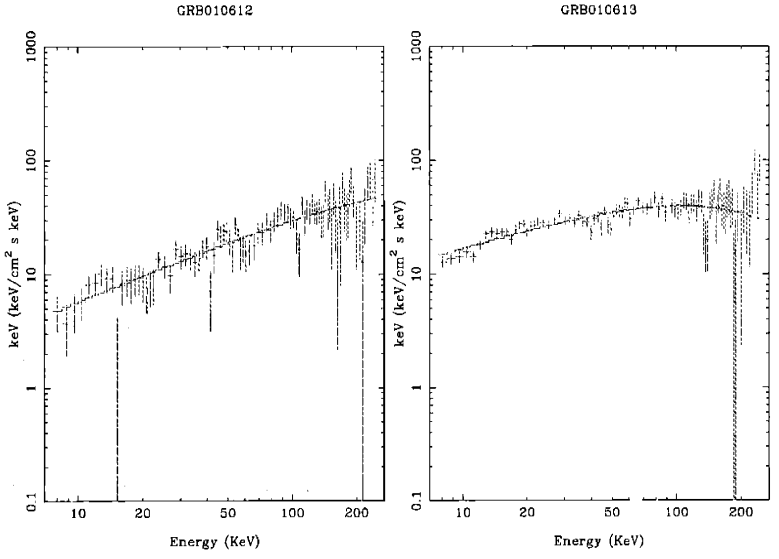

Figure 1-2: Examples of FREGATE GRB spectra with fits to a cutoff power-law model. GRB 010612 shows a cutoff at 600 keV while GRB 010613 shows a cutoff at 176 keV. From Barraud et al. (2002).

A number of instruments have examined the prompt emission of GRBs at X-ray energies (below BATSE's 25 keV low energy limit) and found significant X-ray emis-

sion (Section 1.5.1). This is of great importance because unlike gamma ray detectors which can at best only provide crude localization on a prompt basis[2] (~5°accuracy for BATSE), X-ray instruments, starting with *BeppoSAX*, have been able to localize GRBs to $\lesssim 10'$ accuracy through their prompt X-ray emission, leading to extensive afterglow studies (Section 1.2).

1.1.2 Timescales

The duration of GRBs are typically measured in terms of T_{90}, the time interval over which 90% of the burst counts are measured (T_{50} is also often used). T_{90} shows a clear bimodal distribution with about 2/3 of bursts with $T_{90} > 2s$ categorized as long-duration and about 1/3 of bursts with $T_{90} < 2s$ categorized as short-duration (Kouveliotou et al., 1993). Interestingly, all of the GRBs that have detected afterglow counterparts have been long duration. Thus, much of what we know about GRBs from afterglow and host galaxy studies actually only applies to long-duration GRBs; short duration GRBs remain poorly studied. Figure 1-3 shows a scatter plot of E_{peak} versus Duration (T_{50}) for BATSE events with 10 additional events that were observed in common with the *BeppoSAX* WFC.

1.1.3 Variability

The intrinsic millisecond variability of GRBs suggests that the source regions are small, comparable to stellar dimensions. This small size, combined with the high observed gamma-ray flux of up to 10^{-4}erg/cm^{-2} implies a very high photon density at the source. For a nonrelativistic source, photon-photon scattering would produce an extremely high optical depth for MeV photons; few would escape the burst and the observed flux would only be possible if the bursts were at galactic scales (Cavallo & Rees, 1978). However, for a relativistic source expanding with a high bulk Lorentz factor Γ, the photons have much lower energy in the rest frame of the expansion, so

[2]In a few cases, the IPN has provided ~ few arc-minute sized error boxes that have been released promptly (< 1 day).

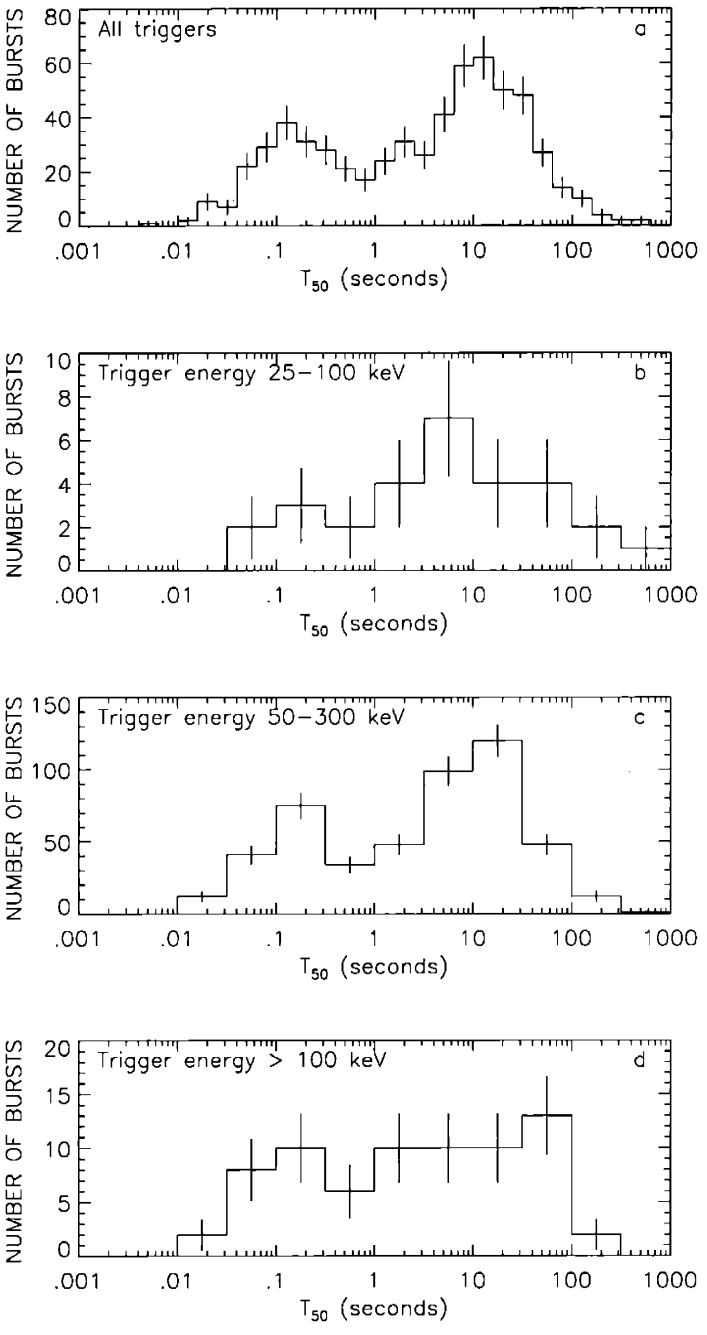

Figure 1-3: Duration distribution (T_{50}) for the BATSE 4B revised catalog. From Paciesas et al. (1999).

the photon-photon interaction cross-section is lower. The photons escape the burst and appear as gamma-rays to us due to a large Lorentz boost of $\Gamma \gtrsim 300$.

1.1.4 Isotropy and the $logN(> P)$ distribution

The large number of GRBs localized by BATSE with ~few degree error boxes convincingly demonstrates the isotropic nature of the GRB sky distribution (Briggs et al., 1996). This places a clear restriction on the GRB source population, ruling out galactic plane sources or other populations that would not be isotropically distributed in the sky.

The cumulative distribution $N(> P)$ of all GRBs greater than a given peak flux P is commonly used to characterize the range of the GRB peak fluxes. Any source that is uniformly distributed in a Euclidean universe will have a $-3/2$ slope in a plot of $logN(> P) vs. LogP$. For bright GRBs, above about 5 ph/cm^{-2}/s, a slope roughly consistent with $-3/2$ is observed. However, at lower flux there is a paucity of bursts, and the $logN(> P)$ distribution flattens (Paciesas et al., 1999). Kommers et al. (2000) performed an archival search of BATSE data to find GRBs that were too faint for the on-board trigger, extending the 50-300 keV threshold peak fluence down by a factor of ~ 2 to about 0.2 ph/cm^{-2}/s, showing that the $logN(> P)$ distribution continues to flatten.

A cosmological population would satisfy the observed isotropy, and the flattening of $logN(> P)$ is expected for a population of sources at cosmological redshifts. More local populations were also considered. In the mid-1990s, before the detection of GRB redshifts could corroborate the cosmological picture, a population of compact objects in a large galactic corona with the diameter of several 100 kpc was proposed (Brainerd, 1992; Bulik et al., 1998; Lamb, 1995; Podsiadlowski et al., 1995; Shklovskii & Mitrofanov, 1985).

1.2 Afterglows, counterparts, and host galaxies

In the mid-1990s, when the GRB distance scale was still unknown, many believed that the issue would only be settled if counterparts were discovered at other wavelengths (Fishman & Meegan, 1995). IPN error boxes were followed up in optical, X-ray, and radio. Though these error boxes were in some cases small ($\sim$ few arcminutes) a convincing counterpart was never discovered, probably because the searches occurred long (weeks or months) after the bursts (Schaefer, 1992; Band et al., 1999; Boer et al., 1993). Others used wide-field cameras to search for optical flashes from GRB optical counterparts (Krimm et al., 1996; Hudec et al., 1999), but these searches did not yield any detections, probably because of lack of sensitivity.

It was recognized Rees & Meszaros (1992) that the compact size implied by variability (Section 1.1.3), combined with very high radiation density, would cause the source to expand rapidly in a relativistic outflow. Based on this, Paczynski & Rhoads (1993) and Katz (1994) theorized that GRBs would be followed by fading emission at other energies, called *afterglow.*

An afterglow from a GRB was first detected in 1997 from GRB 970228 by the Italian – Dutch *BeppoSAX* satellite. The prompt X-ray emission from the GRB allowed the Wide Field Camera (WFC) to localize the event with $3'$ radius precision in the 2–30 keV band (Costa et al., 1997c). After a delay of eight hours, the satellite was reoriented to study the GRB with the Narrow Field Imager (NFI) which detected fading X-ray emission and provided a more accurate ($50''$ radius) localization (Costa et al., 1997b). Subsequently, the GRB was extensively studied in X-ray, radio, and optical wavelengths (Costa et al., 1997a; Galama et al., 1997; van Paradijs et al., 1997). Subsequent optical observations detected a host galaxy of GRB 970228 at $z = 0.695$ (Djorgovski et al., 1999).

The first GRB redshift was determined from *BeppoSAX* GRB 970508 with a spectrum which showed absorption lines consistent with z = 0.835 (Metzger et al., 1997). Subsequent HST observations (Sahu et al., 1997) demonstrated that the optical transient was at the center of a underlying host galaxy, providing the first direct

evidence of the cosmological distance scale for GRBs. Frail et al. (1997) detected the first radio afterglow from GRB 970508. Early radio observations showed strong variability, likely due to Galactic interstellar scintillation, but after a month the variability died away suggesting that the source had increased in size. With the known GRB distance and an understanding of the scintillation properties of the ISM in the direction of the GRB, the size at the time the variability stopped was estimated to be less than $R \simeq 10^{17}$ cm, which also implied relativistic expansion of the fireball.

The redshift of GRB 970508, combined with the measured flux, allowed the determination of the isotropic equivalent luminosity as $L_\gamma = 5 \times 10^{51}$erg/s, assuming that the flux is emitted equally in all directions. This is considerably greater than the flux emitted by a supernova, and comparable to a solar rest mass. However, later observations are consistent with a jet model (Section 1.2.6) where burst explosion is collimated into an angle of $\sim$30 °, giving a burst energy of 5×10^{50}erg/s (Frail et al., 2000).

1.2.1 Redshifts and host galaxies

To date (May 2002) redshifts have been determined for 31 GRBs [3]. In most cases, the redshift was determined for the associated host galaxy, because spectroscopic observations are generally performed too late to detect significant light from the optical transient itself (though some observations have detected absorption-line systems in the optical transients, arising from the ISM of the host galaxy). In some cases, when no optical transient was detected, the host galaxy was found from the position of X-ray and radio counterparts (see Section 1.2.2).

A typical GRB redshift is $z \simeq 1$, with a range of 0.36 (GRB 011121, Infante et al. (2001)) to 4.50 (GRB 000131, Andersen et al. (2000)), though GRB 980425 (Galama et al., 1998a) has a controversial association with a SN and galaxy at $z = 0.0085$ (Section 1.3). GRB host galaxies show great variety, but are typically faint (R $\sim$25). In almost every case where a transient is found, a host galaxy is found at a

[3] Jochen Greiner maintains a database of GRB localizations and redshifts at his web site: http://www.aip.de/People/JGreiner/grbgen.html

corresponding location. HST observations are commonly used to resolve the position of the GRB within the host galaxy (Figure 1-4). In studies of the more than 20 host galaxies observed with HST, the offset of the GRB from the host is found to follow the light distribution (Bloom et al., 2001b; Bloom & Kulkarni, 2001), which is consistent with an association with star-forming regions, and inconsistent with a population of coalescing binaries that would exist in a galactic halo population. GRBs statistically tend to coincide with galaxy light which is reasonable if they have stellar progenitors. A discussion of currently favored progenitor models can be found in Section 1.4.

1.2.2 Association with star formation

Mounting evidence links GRBs to active star formation. Host galaxies are found to be similar to active star-forming galaxies at comparable redshifts (Kulkarni et al., 1998a; Hogg & Fruchter, 1999), but show evidence for an elevated star-formation rate (SFR) (Fruchter et al., 1999b), though the statistical sample remains small. Some GRBs, such as GRB 990123, are clearly seen to come from active star forming regions (Fruchter et al., 1999a). Spectroscopic evidence of massive star formation, such as [O II] and [Ne III] lines, are commonly detected in GRB host galaxies (Djorgovski et al., 2001).

Though there were deep, early optical searches, GRB 970828 had no detectable optical transient (Groot et al., 1998). Detection of a radio flare revealed the position of the host galaxy (Djorgovski et al., 2001); the optical afterglow was likely obscured by dust, which is consistent with star forming regions. Additionally, the increasing evidence linking GRBs to supernova explosions (see Section 1.3) fits well with the idea of GRBs coming from regions of active star formation.

1.2.3 The fireball model

One of the great successes of GRB theory was the prediction by Rees & Meszaros (1992) and Paczynski & Rhoads (1993) that GRBs would be followed by broadband, fading, power-law afterglow emission (Section 1.2.5). In the fireball model, the central

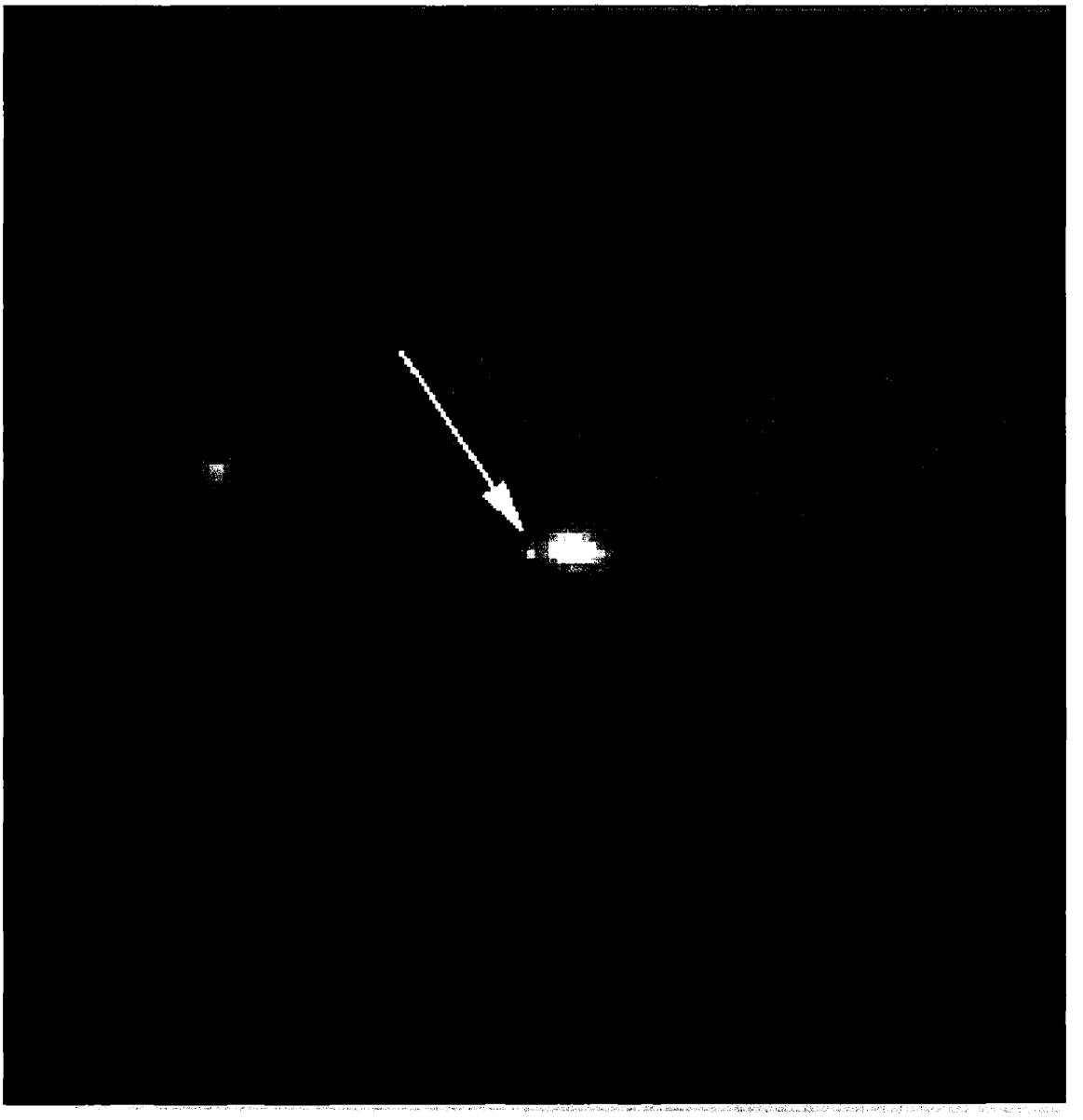

Figure 1-4: HST WFPC2 false-color composite image of an 11″ box around the GRB 010921 host galaxy taken 35 days after the burst. The OT can be seen offset 0.41″ East of the galaxy centroid. Image Credit: Joshua Bloom (Caltech), the Caltech-NRAO-GRB Collaboration, and NASA/Space Telescope Science Institute.

engine (Section 1.4) deposits of order 10^{52} erg in a compact (~stellar-sized) region, surrounded by a uniform density medium (variants of the model consider a nonuniform surrounding medium, see below). The tremendous thermal energy and pressure of the resulting compact fireball causes it to rapidly expand. As the fireball expands, the randomly-directed particle trajectories soon become a uniform outward flowing shell as they reach sufficiently large radii. This transformation of thermal kinetic energy into kinetic energy of an expanding shell is referred to as "strong adiabatic cooling" (Meszaros et al., 1993). Radiation pressure couples the initial energy of the explosion to the initial baryonic mass, M_b, which carries away the kinetic energy in the shell with energy $E_0 = \Gamma_0 M_b c^2$ where Γ_0 is the bulk Lorentz factor. If M_b is small, $< 10^{-5}\mathrm{M}_\odot$, then for $E_0 \simeq 10^{52}$ erg, we expect $\Gamma_0 \simeq 300$, which is the typically observed value.

1.2.4 Internal and external shocks

The next step is to convert the kinetic energy of the expanding fireball into the radiation that we see both as prompt and afterglow emission. The two accepted models for this are internal shocks (Narayan et al., 1992; Rees & Meszaros, 1994) and external shocks (Meszaros & Rees, 1993). Internal shocks involve a central engine that emits multiple shells of ejecta with slightly different Γ_0. As these shells overtake each other, they collide and radiate. This model is favored to explain the prompt emission because the variability in ejected shells can explain the observed variability of prompt X-ray and gamma ray emission.

In the external shock model, the shell collides with the surrounding medium, and expands as a shockwave. Electrons accelerated by the shock emit synchrotron radiation. It is difficult to explain prompt emission with external shocks, as it would require a complicated surrounding medium to explain observed variability. Beyond this, the exact physics of prompt emission is not well understood (see Lloyd-Ronning & Petrosian (2002) and Lloyd & Petrosian (2000) for current theories). However, subsequent to the prompt emission, any shells emitted by the central engine will eventually merge to form a single shell that will expand into the surrounding medium,

radiate primarily by synchrotron, and decelerate.

1.2.5 Fireball afterglow emission

Sari et al. (1998) describe the fireball emission from a population of electrons accelerated by a relativistic shock wave to a power-law distribution, which emit synchrotron radiation. This model, which I will describe below, does a very good job of explaining and in fact predicting the afterglow of GRBs (Katz, 1994; Meszaros & Rees, 1997; Vietri, 1997). I will also discuss several situations where the simplifications of this model break down, and other physical mechanisms must be considered to model the observed afterglow.

A shell of ejecta (blast-wave) with bulk Lorentz factor Γ propagating through a cold medium of uniform density n will create a shocked fluid. Behind the shock, in the ultrarelativistic limit, the particle density is $4\Gamma n$ and the energy density is $4\Gamma^2 n m_p c^2$ (Blandford & McKee, 1976). The electrons are accelerated by the shock to a power-law distribution $N(\gamma_e) \sim \gamma_e^{-p}$ with a cutoff below some γ_m. Assuming a fixed fraction ϵ_e of the shock energy goes into electrons, γ_m is set to give the correct energy density, and $p > 2$ is required to keep the number of electrons bounded. The standard value chosen is $p = 2.5$ (Sari et al., 1996). A significant fraction of the shock energy is also assumed to go into magnetic field density, ϵ_B. The interaction of accelerated electrons with the magnetic field will generate synchrotron radiation.

In the calculations below, which are in the observer frame, to transform from the frame of the ejecta, power is increased by Γ^2 and frequency by Γ. The electrons will radiate power $P(\gamma_e) \sim \Gamma^2 \gamma_e^2 B^2$ at a characteristic frequency $\nu(\gamma_e) \sim \Gamma \gamma_e^2 B$ (Rybicki & Lightman, 1979). Because of the γ_e^2 dependence of $P(\gamma_e)$, the most energetic electrons will quickly cool, moving themselves to lower energies in the $N(\gamma_e)$ distribution. At any given time t since the burst, this effect is important only for electrons that have had enough time to radiate away most of their energy. The relation $\Gamma \gamma_c m_e c^2 \simeq P(\gamma_c) t$, which relates electron energy to emitted energy in time t, gives the critical energy γ_c of an electron that has had time to cool. So, the electron distribution is cut off above γ_c, as well as below γ_m. In general, the $N(\gamma_e) \sim \gamma_e^{-p}$ electron power-law

distribution will result in a synchrotron spectrum of the form $F_\nu \propto \nu^{-(p-1)/2}$ (Rybicki & Lightman, 1979). The synchrotron spectrum will have "break frequencies" ν_m and ν_c, corresponding to the limits of the electron distribution, γ_m and γ_c. There is an additional break frequency ν_a, corresponding to the synchrotron self-absorption cut-off. The resulting spectrum is shown in Figure 1-5.

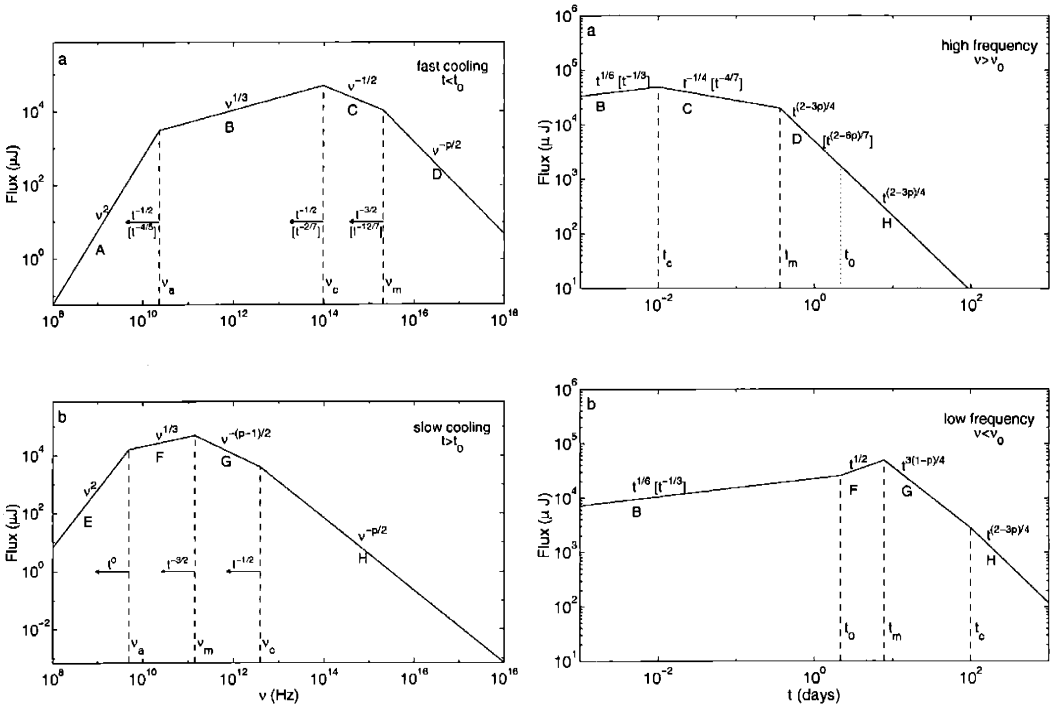

Figure 1-5: Predicted spectrum *left* and lightcurve *right* from fireball model of GRB afterglow emission. The shape of the spectrum is derived as synchrotron emission from a power-law distribution of electrons with a low energy cutoff. The lightcurve comes from the hydrodynamical evolution of the expanding fireball. In the *fast cooling* regime, all electrons have had time to cool significantly; in the *slow cooling* regime, only a fraction of the electrons have had time to cool significantly. From Sari et al. (1998)

The hydrodynamics of the ejecta determine the time evolution of Γ, which in turn is used to calculate the light curve and the time dependence of the spectrum. The ejecta will sweep up mass $\sim \rho R^3$. For an adiabatic shock with a constant energy E_0, expanding into a constant density medium, $E_0 \simeq \Gamma^2 R^3 n m_p c^2$, so $\Gamma \sim R^{-3/2}$.

Using the relation $t \simeq R/4\Gamma^2 c$ to relate the observer time to Γ (details depend on the hydrodynamics; see Sari (1997); Waxman (1997); Panaitescu et al. (1997)), we get $\Gamma \sim t^{-3/8}$. $\Gamma(t)$ specifies the time evolution of the break frequencies and thus the afterglow lightcurve. The result is a model of the flux in the form

$$F_\nu \propto \nu^{-\alpha} t^{-\beta}$$

with a number of break freak frequencies where α makes a step change, and a number of break times where β makes a step change as shown in Figure 1-5.

Though the simple fireball model fits certain data sets well, there is currently much interest in understanding exceptions to its assumptions. The massive star progenitors in some models are expected to have mass loss in a wind, leading to a $\rho \sim R^{-2}$ density profile, rather than uniform density. This will change the hydrodynamic evolution of the ejecta to $\Gamma \sim t^{-1/4}$. The effect would be discernible in the afterglow, but in practice, very few GRBs have had afterglow observations that were broad enough temporally and spectrally to detect it (Harrison et al., 2001). So far there is no clear evidence for a wind density profile (Kulkarni et al., 2000).

1.2.6 Energetics and Jets

For GRBs with known redshift, the total gamma-ray energy assuming isotropic emission is $E_{iso,\gamma} = 4\pi F_\gamma d_L^2 (1+z)^{-1}$, called the equivalent isotropic gamma-ray energy, where F_γ is the gamma-ray fluence of the burst, and d_L is the luminosity distance. Bloom et al. (2001a) calculated $E_{iso,\gamma}$ for 17 GRBs and found a mean of 2.2×10^{53} erg with a range from 5×10^{51} erg to 1.4×10^{54} erg . These tremendous energies challenged the limits of theoretical models, but also raised suspicion that the emission might be collimated into a conical jet rather than isotropic (Waxman et al., 1998; Fruchter et al., 1999a).

More fundamental than $E_{iso,\gamma}$ is E_0, the total GRB energy, yet this is difficult to measure, because relativistic beaming restricts us from observing more than a fractional solid angle $\sim \Gamma^2$ of the ejecta. Frail et al. (2000) were able to circumvent

this issue by observing the radio afterglow of GRB 970508 hundreds of days after the burst when it had slowed to subrelativistic expansion, and they derived a total energy $E_0 \sim 5 \times 10^{50}$ erg , which is considerably lower than the $\sim 5 \times 10^{51}$ erg inferred from the early afterglow, suggesting that the initial explosion had a jet opening angle of ~ 30 deg.

In general, when the beaming angle Γ^{-1} is much less than the jet opening angle θ_j, then the jet afterglow is indistinguishable from a spherical ejecta. However, as Γ decreases, two effects can cause the afterglow to decay more quickly, thus showing evidence for a jet. As the fireball loses energy and Γ^{-1} increases, more and more of the jet is seen by the observer, until $\Gamma^{-1} > \theta_j$ is satisfied at which point the entire jet is seen. Since the amount of the jet that is seen is no longer increasing with time, the afterglow will decay more rapidly, causing a temporal "jet-break" at all energies. Second, the jet will eventually begin to expand laterally, which will slow the expansion as more material is swept up.

At early times when $\Gamma^{-1} < \theta_j$, the hydrodynamical evolution of an expanding relativistic jet is the same as the spherical case, because the matter does not have enough time to expand sideways (Piran, 1994). However, when $\Gamma^{-1} \simeq \theta_j$, sideways spreading becomes important. Sari et al. (1999) use an analytical model that the spreading is comparable to the Lorentz factor, with the jet angle increasing from its initial value $\theta_{j,0}$ like $\theta_j \sim \theta_{j,0} + \Gamma^{-1}$. This model predicts a steep time decay index $\beta = p \simeq 2.4$ after the jet break.

The signature of a jet has been detected in a number of GRBs, either through a broadband break in the lightcurve (Stanek et al., 1999; Harrison et al., 1999), or through detection of polarization that implies a non-spherical geometry (Covino et al., 1999; Wijers et al., 1999). Frail et al. (2001) searched for jet-breaks in 17 GRBs with known redshifts, though in some cases the determination was based on a single band. In other cases, only an upper or lower limit on the time of the jet-break is found. The jet-break time is used to derive the conical opening angle, which is used to correct $E_{iso,\gamma}$ to give the true gamma-ray energy, E_γ. They find (see Figure 1-6) that E_γ is clustered around 5×10^{50} erg , which is comparable to the kinetic energy release of an

ordinary supernovae. This narrow clustering implies that the broad range of observed $E_{iso,\gamma}$ is actually due to a broad range of opening angles, and further, because of these jet opening angles, only a small fraction, one in about 500, of GRBs are visible to us.

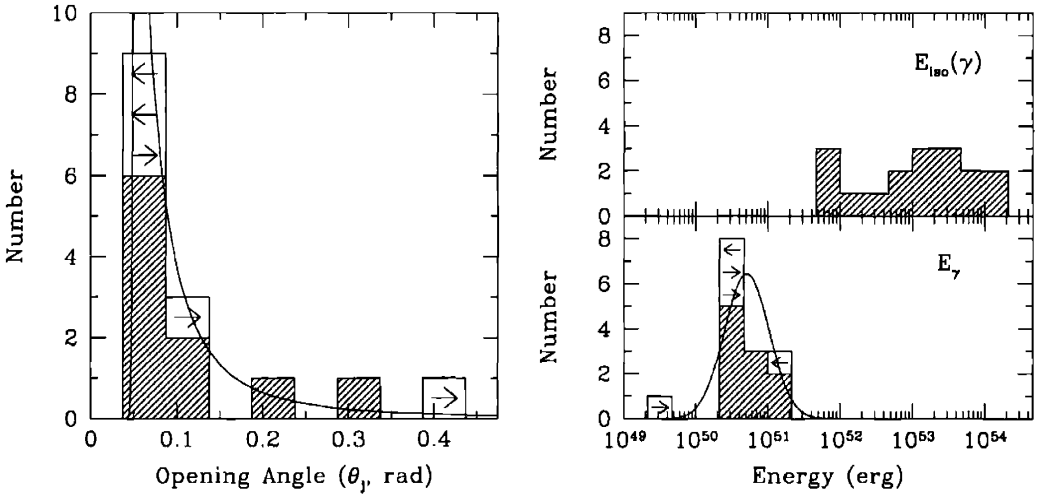

Figure 1-6: *Left:* Distribution of jet opening angles, derived from observed jet break times. *Top right:* Distribution of isotropic equivalent GRB gamma-ray energy. *Bottom right:* Distribution of geometry-corrected GRB gamma-ray energy, with arrows for five GRBs that have an upper or lower limit on the corrected energy. From Frail et al. (2001)

The observed rate of GRBs, $R_{obs}(z=0) = 0.5 Gpc^{-3}\mathrm{yr}^{-1}$ (Schmidt, 2001), is then corrected to the true rate $R_t(z=0) = 25 Gpc^{-3}\mathrm{yr}^{-1}$ (Frail et al., 2001). This rate is marginally (within errors) consistent with the rate of neutron star coalescence (Phinney, 1991) and is well below the rate of Type Ibc supernova, $R_{Ibc} \sim 6 \times 10^4 Gpc^{-3}\mathrm{yr}^{-1}$.

1.3 X-ray line emission and the connection to supernova

With several GRB progenitor models involving a supernova, and the observed association of GRBs with massive star formation, there is much interest in observing an association of GRBs with supernovae. The *BeppoSAX* error box of GRB 980425 was

found to contain a supernova, SN 1998bw (Galama et al., 1998a). The association of these two objects is controversial (Pian et al., 2000), but interestingly SN 1998bw is one of the most energetic supernovae ever discovered, with an ejecta kinetic energy of 5×10^{49} erg and $\Gamma > 2$ (Kulkarni et al., 1998b).

Further evidence for an association with supernovae came when GRB 980326 showed a late-time brightening and reddening (Bloom et al., 1999) that is interpreted as matching a supernova lightcurve at $z = 1$. Similar features were seen in GRB 970228 (Reichart, 1999; Galama et al., 2000), though many other bursts do not show any evidence for a supernova. An alternative explanation to this behavior is "dust echos" due to the blast wave running into high density environments (Esin & Blandford, 2000; Reichart, 2001).

X-ray observations of GRB afterglows can probe the composition of the medium surrounding GRBs by potentially detecting emission lines from elements ejected by a supernova or some other GRB precursor. X-ray line features are detected in six afterglows: GRB 970508 (Piro et al., 1999), GRB 970828 (Yoshida et al., 1999), GRB 990705 (?), GRB 991216 (Piro et al., 2000), GRB 000214 (Antonelli et al., 2000), and GRB 011211 (Reeves et al., 2002). The lines are typically associated with iron, and in cases where the redshift is known (GRB 970508, GRB 980828, GRB 990705, and GRB 000214), the line energy is consistent with redshifted iron. *Chandra* observations of GRB 991216 show an emission line at energy 3.49 keV that Piro et al. (2000) identify as iron K_α at $z = 1.00$ (the redshift is not determined in optical observations). They hypothesize that a large quantity of iron ($\sim 0.1 M_\odot$) surrounds the burst and was earlier ejected by a supernova.

GRB 011211 was observed by *XMM-NEWTON* for 27 ks beginning 11 hours after the burst. (Reeves et al., 2002) detect (at the 3σ level) emission lines from magnesium, silicon, sulphur, argon, calcium, and possibly nickel (Figure 1-7). The lines are *blueshifted* (relative to the Hubble flow) implying that the emission region has an outflow velocity of 0.1c. The features favor progenitor models where a supernova explosion precedes the GRB. The outflow velocity, and an estimated radius of $R \sim 10^{15}$cm for the line emission, imply that the supernova occurred about 4 days (and

at least 10 hours) before the GRB. On such a short time-scale, little iron can be synthesized, which explains the lack of iron lines. (Note: Borozdin & Trudolyubov (2002) have questioned the significance of the lines reported by Reeves et al. (2002). Thus, it is likely that a confirmation of this picture will require a second GRB to be promptly observed by *Chandra* or *XMM-NEWTON*.)

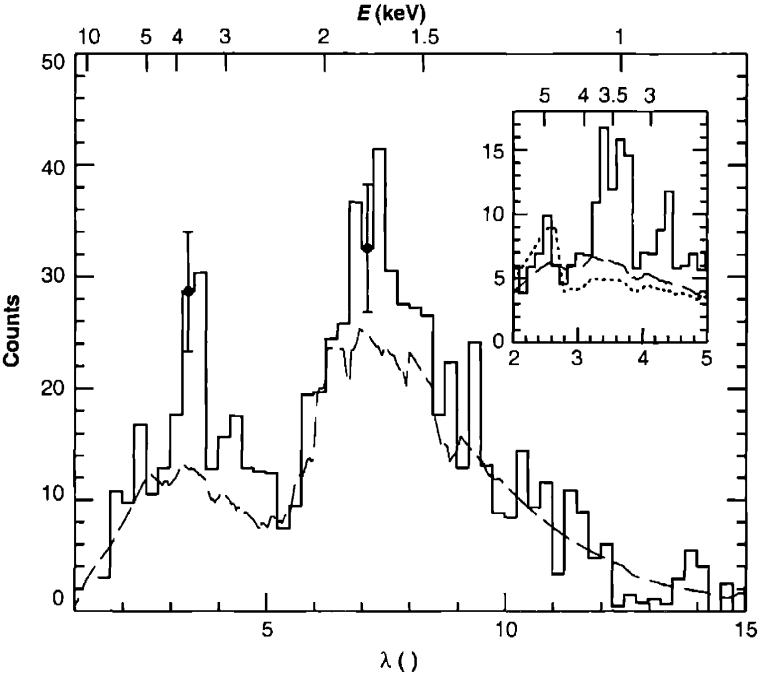

Figure 1-7: A 9700s *Chandra* HETG spectrum of GRB 991216, shows a 4.7σ line feature at $3.5\mathring{A}$ ($E = 3.49 \pm 0.06$ keV), which is identified with Ly_α emission from hydrogenic iron whose rest frame energy of 6.97 keV implies a redshift of $z = 1.00 \pm 0.02$. From Piro et al. (2000).

1.4 Progenitors

The primary constraints on models of GRB progenitors is their huge, rapid energy release of $\sim 10^{51}$ erg in gamma-rays in a few seconds. In general, models describe a "central engine" that quickly deposits the requisite energy in a small region, limited in size to a $few \times 10^7$cm by variability constraints. The baryon mass in the fireball

is limited to about $10^{-5}M_{\odot}$ to allow the observed bulk Lorentz factors of $\Gamma \sim 300$.

Other constraints come from afterglow observations, so they only apply to long-duration GRBs. The afterglow counterparts of short-duration GRBs have not yet been observed (Section 1.1.2). There is substantial evidence connecting GRBs to star-forming regions and massive stars (Section 1.2.2). This includes observations of GRBs in rapidly star forming galaxies, evidence for extinction of optical afterglow by dust, evidence of supernovea associated with GRBs, and observations of line emission in the X-ray afterglow of several GRBs that is sugestive of a supernova precursor (Section 1.3).

The currently favored models fall into two classes: the explosion of a massive star (collapsar, hypernova, and supranova models) and the merger of two compact objects (NS-NS or NS-BH). For long-duration GRBs, the massive star explosion models are favored, while binary coalasence is still considered a possibility for short-duration GRBs. An important similarity among most models is that the final product is a ~stellar mass black hole surrounded by a rapidly rotating torus of material whose energy powers the GRB.

The original "collapsar" model (Woosley, 1993), and the similar "hypernova" model (Paczynski, 1998) describe the core collapse of a massive star directly into a black hole. A torus of material, supported by large angular momentum, rapidly forms around the black hole, and loses its gravitational potential energy through accretion on timescales of seconds, similar to the observed prompt GRB emission. The rotational axis of the system provides a natural avenue for jetted emission. To satisfy small baryon contamination constraints, the star should have lost most of its hydrogen envelope. Wolf-Rayet stars are considered likely candidates in this model, which also provides a link to type Ib/Ic supernovae (MacFadyen & Woosley, 1999).

The supranova model of Vietri & Stella (1998) describes a two-step collapse to a black hole. First, a "supramassive" neutron star (with mass above the Chandrasekar limit but stabilized by angular momentum) forms in a supernova explosion. Loss of angular momentum through magnetic dipole radiation will eventually cause collapse to a black hole and a GRB. Because the supernova explosion sweeps away the

surrounding area, this model provides the required small baryon contamination.

The coalescence of the compact binaries forms another class of GRB progenitors (Paczynski, 1986). These include a variety of binaries, including NS-NS, NS-BH, BH-WD, and BH-HE. These models are generally inconsistent with the association of long-duration GRBs with massive star formation and supernovae, but they still could explain the short-duration burst population. Similar to the collapsar model, the coalescence will result in a black hole our neutron star surrounded by an accretion disk whose energy powers the GRB central engine.

1.5 Additional questions and future research

1.5.1 Prompt X-ray emission and X-Ray Rich GRBs

The ratio of 2 – 10 keV X-ray flux to 50 – 300 keV gamma-ray flux L_x/L_γ provides the usual measure of prompt X-ray emission in GRBs. GRBs with $L_x/L_\gamma > 0.3$ are called "X-ray rich GRBs" (Heise et al., 2001). Ginga detected a significant number of X-ray rich GRBs (Strohmayer et al., 1998). $30 - 50\%$ of GRBs detected by *BeppoSAX* are X-ray rich, and a small fraction of those that have no detectable gamma-ray flux above 40 keV are termed "X-ray Flashes" (XRF, Heise et al. (2001); also called Fast X-ray Transients). Similar numbers of X-ray rich GRBs have been seen by *HETE* (Figure 1-8 and Section 1.5.1).

Because radio or optical afterglow from X-ray rich GRBs has not yet been detected, their properties are not well understood. They may be simply an extension of the long-duration GRB class, they might come from exceptionally high redshifts, or they might represent a new class of GRBs. *HETE* is particularly sensitive to these bursts and thus provides an opportunity to extensively explore their properties.

1.5.2 Optically dark GRBs

Though all prompt and small GRB error boxes since the first discovered in 1997 (GRB 970228) have been searched optically, only about half have yielded an optical

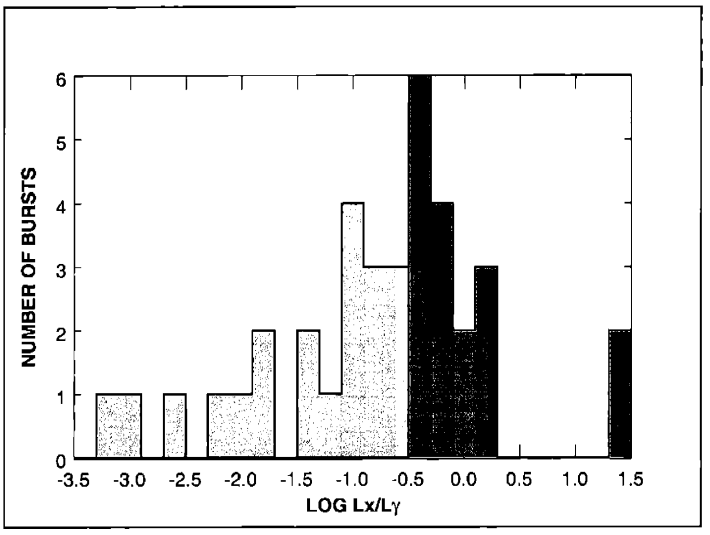

Figure 1-8: The X-ray (2-10 keV) to gamma-ray (30-400 keV) fluence ratios of HETE bursts. X-ray rich bursts are shown in red. Some outliers have been omitted for clarity.

counterpart. The other half is referred to as "optically dark". Studies have shown (Reichart & Yost, 2002) that the lack of an optical counterpart is not caused by the error boxes being too large, or being reported too late, nor is it because the observations in the optically dark cases had systematically different limiting magnitude. Instead, it appears that optically dark GRBs are intrinsically dark. This could be because they come from star forming regions whose dust extinguishes the optical afterglow (Reichart & Price, 2002), or because they are at very high redshifts ($z > 5$) and their optical afterglow is absorbed by the Ly_α forest (Lamb & Reichart, 2000).

1.5.3 Very high redshift GRBs

The set of 31 currently known GRB redshifts extends from $z = 0.36$ to $z = 4.50$ (Section 1.2.1. An interesting question is what maximum redshift might we detect with *HETE*? This requires knowing the intrinsic range of redshifts where GRBs occur, and which of these could be detected by *HETE*. To address this, Lamb & Reichart

(2000) take a set of GRBs with known redshift and determine the maximum redshift where they could be detected by *HETE*. They find that *HETE* could detect GRBs out to $z \simeq 20$ (Figure 1-9). Simulations predict significant star formation out to this redshift (Gnedin & Ostriker, 1997) which might produce associated GRBs. Detecting such bursts would provide a unique way to study star formation at these extreme redshifts.

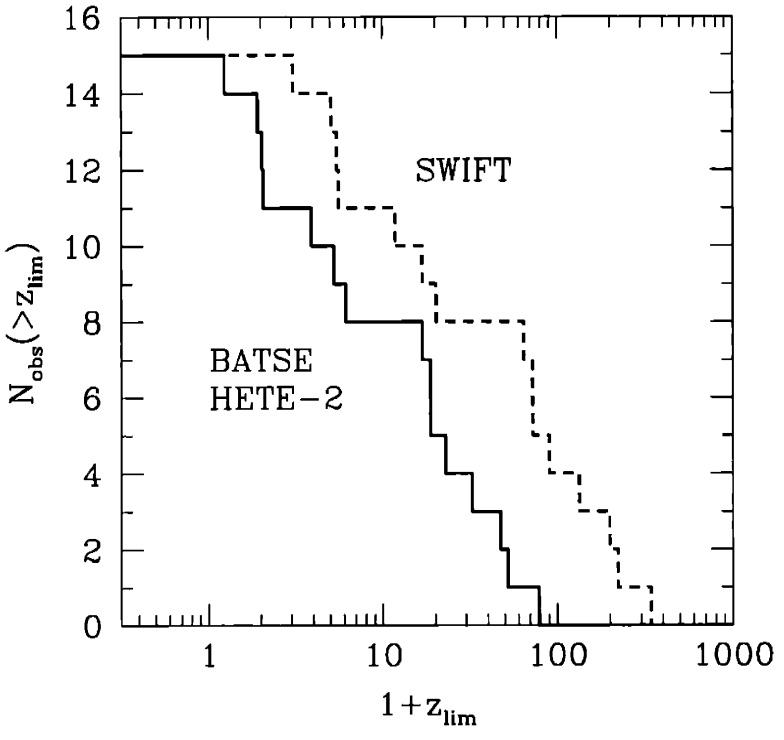

Figure 1-9: Cumulative distributions of the limiting redshifts at which fifteen GRBs with well-determined redshifts and published peak photon number fluxes would be detectable by BATSE and *HETE*, and by *Swift*. From Lamb & Reichart (2000).

1.6 Thesis overview and my role in the *HETE* mission

The *HETE* mission is an international collaboration, primarily centered at MIT (Section 2.1). As a member of the *HETE* team, my participation in the mission has been broad, so accordingly I present a broad overview of the *HETE* mission in Chapter 2, with descriptions of science instruments, the spacecraft, mission operations, primary ground stations, burst alerts, and a review of *HETE* science results thus far. As a duty scientist at the *HETE* Mission Operations Center at MIT, I was required to understand at an operator level all science instruments (Section 2.2), the spacecraft (Section 2.3), the primary ground stations (Section 2.3.2), and the burst alert network (Section 2.4). I built, tested, and helped to deploy a number of the burst alert stations, and I served as the network system administrator for the entire burst alert network. I also helped maintain the burst alert network, including a repair mission to the Galapagos burst alert station. I participated in spacecraft environmental testing at MIT Lincoln Laboratory, spacecraft and lauch vehicle integration at Vandenburg Airforce Base in Lompoc, California, and launch operations at Kennedy Space Center in Cape Canaveral, Florida.

My primary focus has been the SXC, where I had a major role in the fabrication, testing, integration, and in-flight operation of the instrument. This work, which was done in collaboration with several other SXC team members, is presented in Chapter 3. I also worked extensively on SXC data analysis, which is presented in Chapter 4. I wrote a suite of IDL SXC analysis software tools that process raw SXC data with considerable flexibility. The software uses a cross-correlation technique to generate an image of the X-ray sky from raw CCD data. My software uses spacecraft aspect data and WXM science results to maximize the sensitivity of the SXC to GRBs. Further, when a candidate X-ray transient is detected by the WXM, my analysis tools can perform a completely automated analysis of the SXC data to determine if the source is detected in the SXC.

A major effort of the *HETE* science team is responding to GRBs and other

X-ray transients detected by *HETE* and rapidly disseminating our results to the international observer community. As part of this effort, I have been a co-author on more than 44 *GCN Circulars*. I have also led follow-up observation campaigns of several *HETE*-localized GRBs. Chapter 5 describes optical observations of GRB 011212 and GRB 020331 with the Magellan consortium's 6.5m Baade telescope, which resulted in the detection of the host galaxy of GRB 020331. Chapter 6 describes our follow-up observations of GRB 011130 with the Chandra X-Ray Observatory and with ground-based optical telescopes.

Chapter 2

The High Energy Transient Explorer

2.1 Overview

[1] The High Energy Transient Explorer (*HETE*) mission is devoted to the study of gamma-ray bursts (GRBs) using soft X-ray, medium X-ray, and gamma-ray instruments mounted on a compact spacecraft. A powerful feature of *HETE* is its potential for localizing GRBs within seconds of the trigger with good precision ($\sim 10'$) using medium energy X-rays and improving the localization to $\sim 20''$ accuracy using low energy X-rays. Real-time GRB localizations are transmitted to ground observers within seconds via a dedicated network of 14 automated "Burst Alert Stations" (BAS) and the GRB Coordinates Distribution Network (GCN), thereby allowing prompt optical, IR, and radio follow-up, leading to the identification of host galaxies and the measurement of redshifts for a large fraction of *HETE* GRBs.

HETE is currently the only satellite that can provide near-real time localizations of GRBs, and that can localize GRBs that do not have X-ray, optical, and radio afterglows. These capabilities are key to allowing us to probe further the unique physics that produces the brightest photon sources in the universe.

[1] Parts of this chapter come from the *HETE* Science Team's unpublished proposal to the NASA 2002 Senior Review of Space Science Mission Operations & Data Analysis Programs

A Science Team from France, Japan, Brazil, India, Italy, and the US is responsible for the *HETE* mission. MIT is the PI (principal investigator) institution. The *HETE* mission is unique in that it is entirely "self-contained," insofar as it has relied upon dedicated tracking, data acquisition, mission operations, and data analysis facilities run by members of the international Science Team since the launch in October 2000.

HETE is detecting GRBs at a rate of $\sim$90 yr^{-1}, and is now localizing GRBs at a rate of $\sim$15-20 yr^{-1} with sufficient accuracy to allow optical, radio, and X-ray followup observations. In addition, it has detected $\sim$25 bursts from soft gamma repeaters (SGRs), and >200 X-ray bursts (XRBs). As of May 2002, in the most recent 7 months, *HETE* has localized 10 GRBs; four of these have led to the detection of an optical afterglow and another has led to the identification of probable radio and X-ray afterglows.

The *HETE* mission should continue addressing basic questions about GRBs over the next 3 years: "Why are there optical afterglows for only $\sim$1/2 of all GRBs?"; "What are the 'X-ray Rich' GRBs?"; "Are there other, rarer types of GRBs?"; "What are the short GRBs?"; "Are there GRBs at z>10?".

2.2 Instruments

HETE's science instrument suite consists of the French Gamma Telescope (FREGATE), the Wide-Field X-Ray Monitor (WXM), and the Soft X-ray Camera (SXC). These three instruments have co-aligned fields of view. FREGATE is a non-imaging gamma-ray (6 keV to > 400 keV) detector that acts as a sensitive GRB trigger and provides accurate GRB timing and broadband spectroscopy. The WXM is a coded aperture X-ray imager with the primary purpose of localizing GRBs with 5-10 $'$ radius error circles. SXC is a coded aperture soft X-ray imager that can provide $\sim$ 1 $'$ GRB localizations for a subset of WXM-localized bursts.

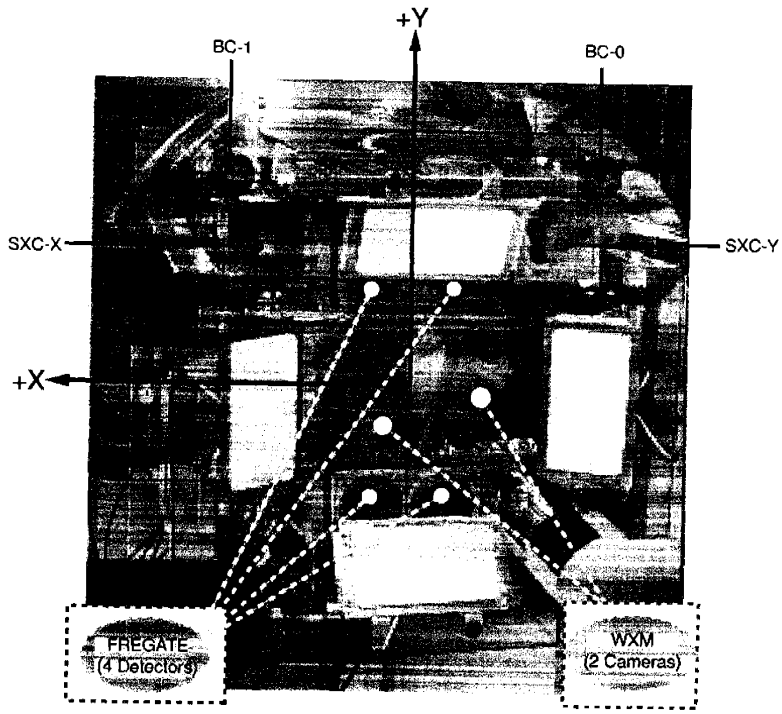

Figure 2-1: Instrument face of the *HETE* satellite. In this view, the two pairs of circular detectors comprising FREGATE are labeled "FREGATE (4 Detectors);" the two 1-D masks and detectors comprising the WXM are located in the center of the picture and are labeled "WXM (2 cameras);" and the two square units comprising the SXC are located at the upper left and upper right corners of the picture and are labeled "SXC-X" and "SXC-Y."

2.2.1 Gamma-Ray Detectors

The prime objectives of the French Gamma Telescope (FREGATE) are the detection and spectroscopy of GRBs, SGR bursts, and XRBs, and monitoring of other variable sources. Table 1 lists its properties. FREGATE has functioned flawlessly since launch (Atteia et al., 2002); its sensitivity is more than a factor of two better than was expected prior to launch. Its GRB detection rate is ≈44 confirmed bursts per year, plus over 50 unconfirmed bursts per year. Of the ≈44 confirmed bursts per year, about 11 originate from outside the passively collimated field of view of the detector. (The passive collimator reduces the low energy background by excluding the diffuse cosmic component and the contributions from soft sources in the Galactic center

Table 2.1: FREGATE omnidirectional γ-ray Spectrometer

Built by	CESR (France)
Instrument type	Cleaved NaI(Tℓ)
Energy Range	6 keV to > 400 keV
Timing Resolution	10 μs
Spectral Resolution	~13% @ 81 keV, ~10% @ 356 keV
Effective Area	160 cm^2
Background count rate 25-100 keV	100 c/s/detector
Sensitivity, 6 σ, 50 - 300 keV	$\sim 1 \times 10^{-7}$ erg/cm^2/s
Passively collimated field of view	~4 steradians

region, but is semi-transparent to GRBs).

The FREGATE spectral response was extensively calibrated prior to launch, and the calibrations have been confirmed in flight using observations of the pulsed spectrum of the Crab Pulsar. The in-flight energy resolution is excellent and the lower energy threshold is 6 keV, due to the use of cleaved crystals. For each burst whose arrival direction is known, a response matrix is constructed and models of the incident photon spectrum are fit to the data using XSPEC. The combination of broad energy range and good energy resolution is a powerful one for the discovery and study of spectral features.

2.2.2 WXM

The primary objectives of the Wide-Field X-Ray Monitor (WXM) are the detection, localization, and spectra of GRBs, SGR bursts, and XRBs. Table 2 lists its properties. The WXM has performed well since launch. The sensitivity of the WXM is equal to that expected prior to launch.

The localization accuracy of the WXM is better than expected prior to launch (systematic error <2.7′ rather than >5′), as calibrated using observations of the Crab, Sco X-1, SGRs 1806-20 and 1900+14, and numerous known X-ray burst sources (see Figure 2-2; Graziani & The HETE Science Team (2002), Shirasaki et al. (2002)). The WXM has successfully localized nearly all of the GRBs that it has detected. The flight software has correctly localized 6 GRBs in near-real time, but these locations

Table 2.2: Wide Field X-ray monitor

Built by	RIKEN (Japan) and LANL
Instrument type	Coded Mask with PSPC
Energy Range	2 to 25 keV
Timing Resolution	1 ms
Spectral Resolution	$\sim$ 25% @ 20 keV
Detector QE	90% @5 keV
Effective Area	$\sim$175 cm^2 (each of two units)
Sensitivity (10 σ)	$\sim 8 \times 10^{-9}$ erg/cm^2/s (2-10 keV)
Field of View	1.6 steradians (FWZM)
Localization resolution	$19'$(5σ burst) $2.7'$(22σ burst)

were not sent out to the astronomical community due to technical issues. One SGR burst and two X-ray bursts that the WXM flight software correctly localized in near-real time were sent out to the astronomical community. An additional 6 SGR bursts and 25 X-ray bursts that the WXM flight software correctly localized in near-real time were not sent out to the astronomical community, in order not to overwhelm the community with non-GRB burst alerts, or because real-time spacecraft aspect was not available.

The WXM spectral response was extensively calibrated prior to launch, and the calibrations have been confirmed and refined in flight using observations of the Crab nebula. The in-flight spectral resolution is equal to that expected. For each burst that is detected, a response matrix is being constructed and models of the incident photon spectrum are fit to the data.

Like the other *HETE* instruments, then WXM benefits from an exceptionally low and stable background throughout *HETE*'s equatorial orbit. The background rate does exhibit strong temporal variations during the months that the Galactic bulge region is in the WXM FOV.

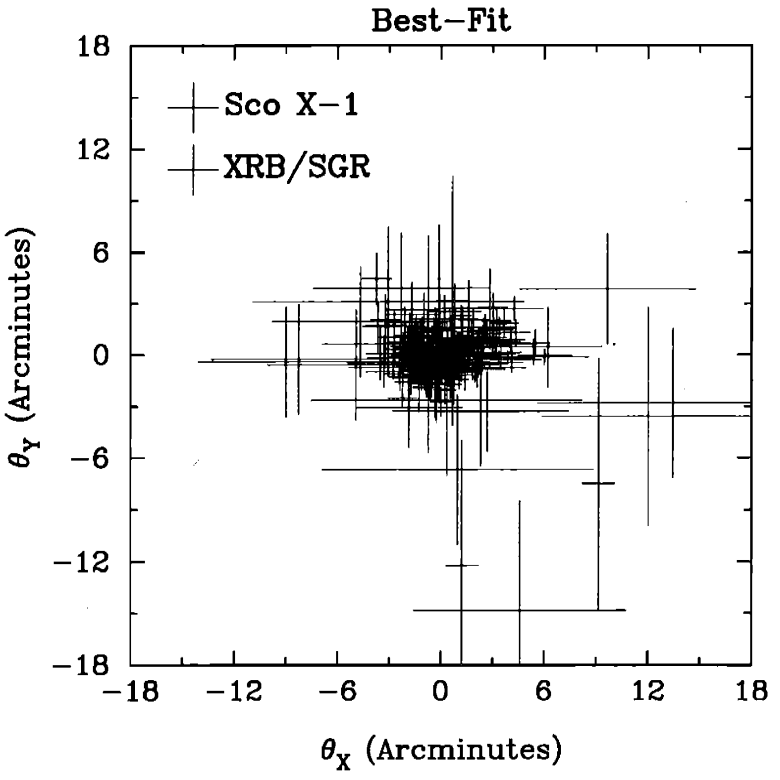

Figure 2-2: WXM systematic error in location. The figure shows the deviations of Sco X-1 (purple crosses) and various SGR and XRB sources (red crosses) from their true locations after applying the best-fit astrometric correction to the Sco X-1 data. The error bars are the statistical errors in location. (Graziani & The HETE Science Team, 2002)

2.2.3 SXC

The *HETE* soft X-ray cameras (SXC; Ricker et al. (2002g), Villasenor et al. (2002), Monnelly et al. (2002)) were designed to provide fine ($<1'$) localization of bursts, based on their 1-10 keV emission. The SXC consists of two orthogonally-oriented, one-dimensional coded aperture units, each comprised of a fine ($\sim$45 μm) featured slit mask, separated by 10 cm from an X-ray CCD detector plane, with 15 μm pixels. The pre-launch and current properties of the SXC are given in Table 2.2.3. This section provides an overview of the SXC; see Chapter 3 for discussion of SXC design and performance and see Chapter 4 for a discussion of SXC imaging and sensitivity.

To prevent contamination of the CCD detectors by non X-ray photons, the SXC

Table 2.3: Soft X-ray Camera

	At launch (both OBFs intact)	At present (Inner OBF only)
Built by	MIT CSR	
Instrument type	4 CCID-20	2 CCID-20
Camera dimensions	10cm × 10cm × 17.5cm	
Energy Range	500 eV to 14 keV	1.3 to 14 keV
Timing Resolution	1.2s	
Spectral Resolution	46 eV @ 525 eV 129 eV @ 5.9 keV	~300 eV @ all energies
Detector QE Detector QE > 20%	93% @ 5 keV, 0.5–14 keV	93% @ 5 keV, 1.3–14 keV
Effective Area	74.4 cm^2	37.2 cm^2
Source Sens (Crab)	2.3 $t^{-1/2}$ (5.5σ)	1.9 $t^{-1/2}$ (3.5σ)
Burst Sens ($cts/cm^2/s$)	1.0 (5.5σ)	0.8 (3.5σ)
FOV (FWZM)	1.88 sr	1.29 sr*
Focal Plane scale	33″ per CCD pixel	
Localization	20″(systematics limit)	

*There is an additional 0.54 sr FOV for one-sided localizations.

was provided with two redundant optical blocking filter (OBF) systems: 1) very thin (0.5 μm) aluminized plastic films, covering the entire aperture, and 2) Be foil (25 μm) filters, covering 1/2 of the detector area. The thin film OBF system operated for 3 months (Y-camera) and 5 months (X-camera), respectively. After those times, the films were apparently lost due to erosion by atomic oxygen. [2]

The foil OBFs have remained intact throughout the mission. However, the foil OBFs protect only 1/2 of the detectors, and are subject to edge leakage during bright moon conditions. As a result, the SXC sensitive area is now 1/2 the value at launch, and the SXC can only be used during the "lunar dark" of the month (*i.e.*, 20 days, or ~70% of each lunar month).

After the loss of the outer OBFs, an extensive re-write of the SXC flight software was required to correct for residual light leakage. The revised flight software was uploaded and tested in July 2001, which successfully revived the SXC. Prior to launch,

[2]Atomic oxygen densities at 600km apparently increase by 10^3-10^5 times during intense solar flares (Dooling & Finckenor, 1999). *HETE* experienced a series of such flares in late 2000 – early 2001, shortly before the loss of the SXC outer OBFs. The existence of this strong dependence of atomic oxygen on solar activity at the *HETE* orbital altitude was not known at the time the SXC underwent its design reviews in 1998.

we had estimated that the SXC would localize about 1/3 as many GRBs as would the WXM (albeit with 100× smaller error circles), based on a solid angle-area-time product comparison. In fact, with the SXC acting as a "vernier" for the WXM, the usable SNR for SXC localizations was improved by $\sim 1.5\times$ over pre-launch estimates (see Table 3). With the reduction in sensitive area because of the Outer OBF loss, and accounting for the reduced operating time per month, we estimate that the SXC will localize 1/6 as many GRBs as will the WXM. For a WXM localization rate of 17 events yr^{-1}, we now expect an SXC localization rate of ~2–3 events yr^{-1}.

During July-August 2001, the SXC localized 9 galactic transients, produced by 4 XRBs and 1 SGR (Monnelly et al., 2002), to an accuracy of $< 1'$. (NB: During the 9 months in which the SXC has been restored to operation, all 10 of the WXM-localized GRBs (Table 2.4) have occurred either at times of bright moon, were measured to be faint in the WXM, or were outside the useful FOV of the SXC. Thus, no GRB localizations by the SXC have yet occurred.)

2.3 Spacecraft and mission operations

HETE was launched into an equatorial low Earth orbit by a Pegasus rocket from Kwajalein Atoll in the Republic of the Marshall Islands in October of 2000. *HETE* orbits the Earth every 96 minutes at an altitude of 600 kilometers. During normal operations, *HETE*'s solar panels are continually oriented towards the sun. The suite of science instruments face opposite the solar panels (figure) and thus always face the anti-sun direction. The instruments are co-aligned and cover about a two steradian field of view (the individual instruments have different fields of view). The fields of view follow the ecliptic plane throughout the year, always 180° from the sun. This ensures that any GRBs detected will be at least 120° from the sun which is optimal for optical follow-up observations.

The science instruments are operated during the 35 minute night of each orbit. They are turned off during orbit day because the sun-illuminated earth is in their fields of view. During orbit day, the sun allows the solar panels to charge the batteries

which then power the spacecraft during orbit night. To maximize instrument on-time, FREGATE and WXM operations are typically extended a few minutes on either side of night into twilight increasing "live time" from 35 to 40 minutes. The SXC and optical cameras cannot be operated in twilight because scattered light saturates the CCD detectors.

2.3.1 Attitude control system

HETE's attitude control system (ACS) is primarily designed to maintain anti-sun pointing during orbit day and night. The attitude control system displayed its authority when *HETE* attained its on-station orientation, in its nominal anti-solar orientation, within three hours of launch. Since then, it has performed well, both in normal operations and after rare spacecraft anomalies. A magnetic torque coil system and a single momentum wheel control spacecraft orientation. During the day, aspect is determined by sun sensors and magnetometers, which together provide $\sim 1^\circ$ accuracy of pitch, yaw, and roll. During night, the suite of four optical CCD cameras determine aspect relative to stars to a much higher precision (we have recently improved orbit night stability to $<2'$ RMS.). Two of these are called "ACS cameras". These are tilted at 45 degrees with respect to the science instruments, which improves determination of spacecraft roll. The two others are called "boresight cameras", as they are co-mounted and co-aligned with the SXC. The proximity of the boresight cameras to the SXC provides additional stability against thermal fluctuation, which provides more accurate aspect determination, needed for the SXC's high angular resolution.

2.3.2 Primary ground stations

A network of three primary ground stations (PGSs) provide uplink and downlink via a high speed S-band radio link to *HETE*. The PGSs have an internet link to the MIT mission operations center where uplinked commands originate, and downlinked data is processed, analyzed, and archived. The *HETE* primary ground stations (PGS) are

located at the National University of Singapore, the Kwajalein Atoll in the Republic of the Marshall Islands, and at Cayenne, French Guinea. All three stations are currently operating at full capacity, downlinking up to 9 Mbytes of spacecraft data per contact for up to 15 contacts per day. Additional downlink, in the form of real-time messages, are provided by the Burst Alert Stations (Section 2.4).

2.4 Burst Alerts

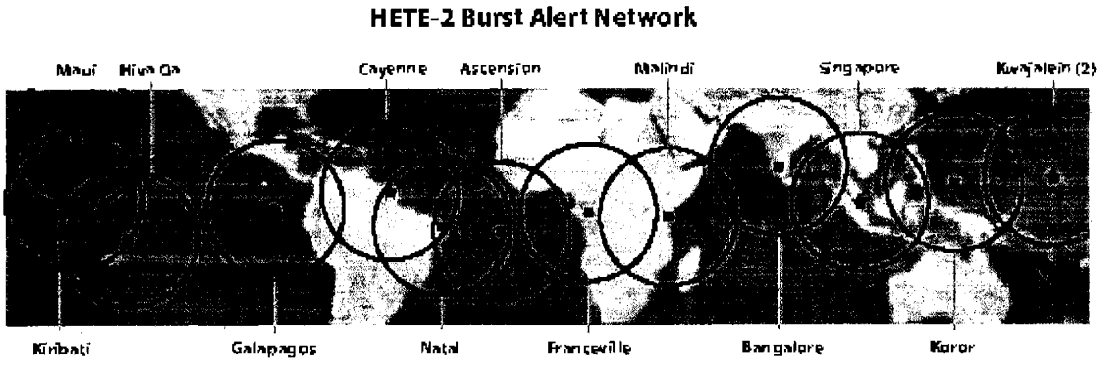

Figure 2-3: The 14 *HETE* Burst Alert Stations (BAS) are distributed in longitude near the equator in a manner that *HETE* is within range of a BAS over 99% of its orbit.

2.4.1 Burst Alert Network

The transient nature of GRB afterglows (Section 1.2) makes it valuable to disseminate localizations as soon as possible to allow rapid follow-up observations. *HETE* is capable of autonomously determining GRB positions on board in real-time. Burst positions are transmitted to the ground over a 300 bps VHF signal to Burst Alert Stations (BAS). Each BAS consists of an omnidirectional antenna, a VHF receiver, a PC (running software to extract the messages from the audio signal from the receiver), and an internet connection for transmitting data to the MIT Control Center.

The *HETE* Burst Alert Network (BAN) currently consists of fourteen BASs sited at locations along the equator (see Figure 2-3). All stations in the BAN, with the

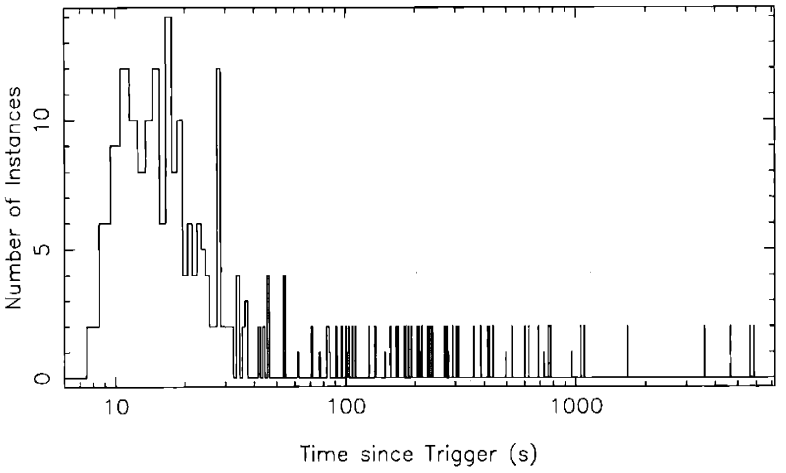

Figure 2-4: Histogram of the time delay between trigger detection on board *HETE* and the transmission of the first GCN Notice from the GCN Center at GSFC. For the majority of burst alerts, the notification is sent out <20s after the burst trigger; the long tail of the distribution is created by bursts that occurred over gaps in the Burst Alert Network.

exception of Kiribati, are now operating routinely, except for instances of power or Internet interruptions. The average real-time coverage of *HETE*'s orbit has improved from ~40% at the beginning of 2001 to the current value of ~85%.

Notification of *HETE* bursts proceeds in two steps: first, the results of the on-board analysis of burst data are distributed via the Burst Alert Network in near real time; then, once the full burst data set is available on the ground, the results of ground analyses may be distributed.

2.4.2 Real-Time Alerts

Information about GRBs detected by *HETE* is transmitted to the BAN in real time, immediately relayed to the *HETE* Mission Control Center at MIT, and then promptly reformatted and sent to the GRB Coordinates Distribution Network (GCN); the GCN then distributes the information in the form of email, pager and/or Internet socket messages to observers around the world. The first message received by observers includes the time, energy range, duration, and significance of the detected burst; sub-

sequent messages can include burst localizations as calculated by the flight software, if the burst was in the WXM field-of-view.

The response time of the *HETE*-to-GCN system depends strongly on the presence of a functioning BAS with Internet access within receiving range of *HETE* at the time of message transmission. When this is the case, the time between burst detection and receipt by the observer is typically under 20s; in other cases, the delay can be as long as 15 minutes. The distribution of delays is shown in Figure 2-4.

2.4.3 Results of Ground Analyses

Once the detailed burst data are collected by a PGS, typically 20–60 minutes after the burst, more detailed analyses of the burst data can be performed. In typical cases, a more precise burst localization with a smaller error radius than any calculated on board is available within 10 minutes of receipt of data. Such positions are distributed as a GCN Notice as soon as the entire burst analysis team agrees on the results of the analyses. Bursts H1896, H1902, H1959, and H1963 are examples of this process (refer to Table 2.4).

In some cases, the ground burst analysis is more complex: the spacecraft aspect is difficult to calculate due to contamination by moonlight, the burst shows strong spectral evolution, or the results of independent analyses of the same data show large discrepancies. In these situations, the refined burst localization is delayed by several hours, while the science team performs further analyses. Bursts H1761, H1770, and H1864 are examples of these cases.

Finally, routine inspections of survey data have revealed several untriggered bursts. These analyses are typically only completed several hours after the burst occurred, so significant delays are incurred in the analyses of the data. Bursts GRB011019 and GRB011212 are examples of this type of burst.

Table 2.4: Eighteen GRBs localized by the *HETE* Spacecraft to date. SNR: signal-to-noise ratio. Alert Delay: delay for initial FREGARE or WXM trigger, not necessarily including a WXM localization. Loc. Delay: delay for WXM localization.

GRB	*HETE* ID	GCN Circular	FREGATE SNR[1]	WXM SNR[2]	Error Radius	Alert Delay	Loc. Delay	Comments
010110	untrig	-	-	23.3	[$\sim$10′]	N/A	N/A	Fregate was off
010213	untrig	934	9.8	69.4	3.5′	36h	36h	X-ray rich
010225	H1491	-	15.9	19.8	[$\sim$10′]	N/A	N/A	X-ray rich; no aspect
010326B	H1496	1018	19.7	11.2	18′	4.75h	4.75h	Soft spectrum
010612	H1546	1065	23.2	9.1	36′	15s	69h	*HETE* +IPN
010613	H1547	1067	70.2	12.1	36′	102s	57h	Double-peaked
010629B	H1573	1075	62.3	21.8	15′	78s	6.5h	Double-peaked
010921	**H1761**	**1096**	**83.3**	**7.3**	**10′**	**17s**	**5.2h**	**Optical ID**
010928	H1770	1103	48.9	6.3	6′	203s	6.2h	1-sided error box
011019	untrig	1109	10.1	14.1	35′	12.1h	12.1h	X-ray rich
011130	H1864	1165	4.1	9.7	7.6′	4.4h	4.4h	X-ray rich (Chandra TOO)
011212	untrig	1194	7.4	8.9	11′	6.3h	6.3h	X-ray rich
020124	**H1896**	**1220**	**41.1**	**11.4**	**12′**	**11s**	**1.4h**	**Optical ID; Long**
020127	**H1902**	**1229**	**37.9**	**17.1**	**8′**	**96s**	**1.8h**	**Radio ID (Chandra TOO)**
020305	**H1939**	**1262**	**7.2**	**3**	**25′**	**42s**	**10h**	**Optical ID; double-peaked**
020317	H1959	1280	11.8	8.8	18′	34s	0.9h	X-ray rich
020331	**H1963**	**1315**	**27.2**	**9.7**	**8′**	**55s**	**0.7h**	**Optical ID; Long**
020531	H2042	1399	22.38	7	25′	1.47h	1.47h	Short/hard; X-ray/Optical ID?

[1] 8-85 keV; [2] 2-25 keV

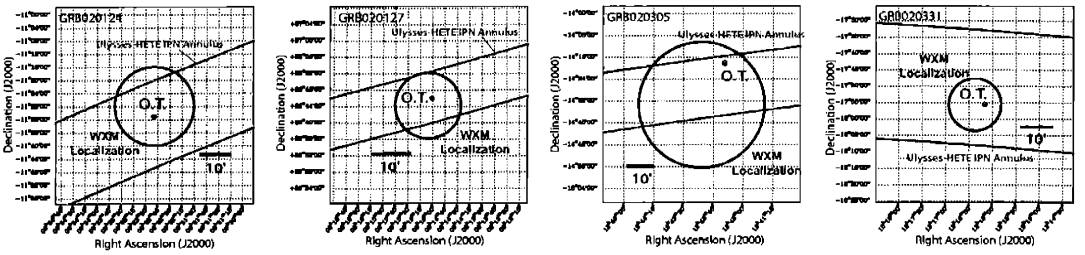

Figure 2-5: *HETE* error circles, IPN annuli, and locations of optical afterglows for four GRBs.

2.5 HETE Scientific Results

2.5.1 Gamma-Ray Bursts

FREGATE is detecting GRBs at a rate of $\approx$ 44 confirmed GRBs yr^{-1} and over 50 unconfirmed GRBs yr^{-1}. About 75% of the confirmed GRBs originate within the FOV of the FREGATE collimators. WXM has localized 18 GRBs since January 2001, with accuracies of 6 - 20 arcminutes. Table 2.4 lists the properties of these 18 events.

2.5.2 GRB Afterglows and Redshifts

In the 7 months prior to May 2002, the *HETE* mission has produced 10 localizations, corresponding to a rate of ≈ 17 yr^{-1}. Four of these 10 localizations have yielded optical afterglows (with 2 redshifts measured so far); one more has yielded probable X-ray and radio afterglows. Figure 2-5 shows the HETE WXM error circle, IPN annulus, and location of the optical transient for the 4 bursts with optical afterglows. Figure 2-7 shows the lightcurves in 6 X-ray and γ-ray energy bands, and the fading optical afterglow, of GRB010921, the first HETE burst for which an optical afterglow was detected. This burst was relatively bright and has a redshift $z = 0.450$, making it a favorable candidate for detecting a SN component in the lightcurve and spectrum of the optical afterglow. However, no such component was detected.

Figure 2-8 compares the brightnesses of the optical afterglows of HETE GRBs and

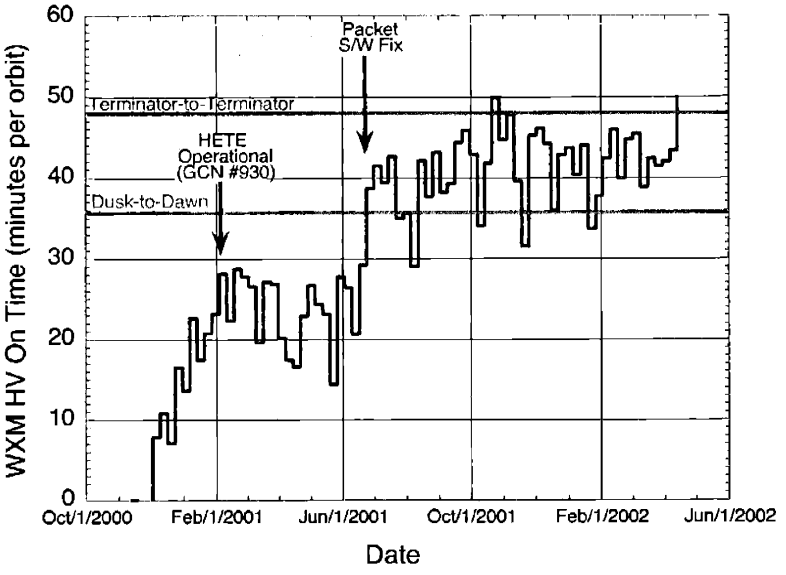

Figure 2-6: The mean WXM HV on time as a function of time through the *HETE* mission, which is a good indicator of the overall operational efficiency of *HETE* during its mission. Indicated are the time at which *HETE* was declared capable of detecting and localizing GRBs and the date on which spacecraft communications became more robust (Section 2.3). The mean operation efficiency of *HETE* effectively doubled after July 1, 2001, when compared with the months immediately after declaration of operations.

those of previously known optical afterglows. The dissemination of a number of HETE GRB localizations within 0.7-2 hours of the burst (see Table 2.4) has allowed optical follow-up observations to probe the brightness distribution of optical afterglows at early times. In addition, there is every reason to believe that the HETE mission will produce real-time localizations. Figure 2-9 shows that, if some GRB optical afterglows are very bright, these near-real-time localizations will allow robotic telescopes to probe the transition from the burst itself to the afterglow (robotic telescopes are able to respond to GCN Alerts by automatically slewing to observe the position, with typical delays of minutes).

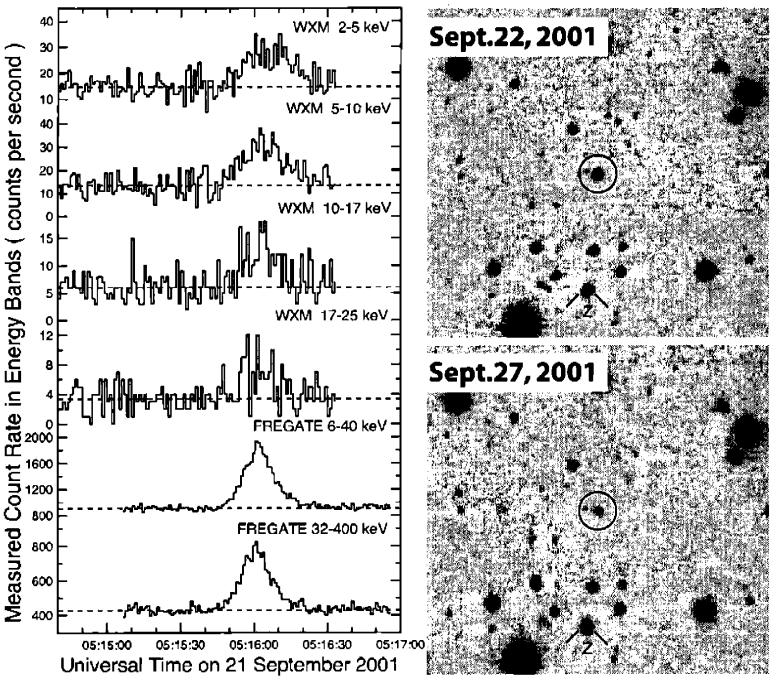

Figure 2-7: At left, the light curve of GRB010921 as seen by FREGATE and the WXM. At right, images of the fading optical counterpart of GRB010921 (Price et al., 2002a)

2.5.3 X-Ray Rich GRBs

FREGATE has detected 18 "X-ray rich" GRBs (Section 1.5.1; i.e., bursts for which $L_x/L_\gamma \equiv F_{2-10\mathrm{keV}}/F_{50-300\mathrm{keV}}$ is > 0.3) (see Figure 2-10); six of these occurred within the WXM FOV and were localized by the WXM (see Table 2.4). Thus, $\approx 40\%$ of the GRBs detected by the HETE mission are "X-ray rich" bursts. This is similar to the recent report that 30-50% of the GRBs seen by the WFC's on BeppoSAX are "X-ray rich" (Heise, 2002).

Are X-ray rich GRBs nearby or exceptionally far away? Are any associated with supernovae? The HETE mission has disseminated the localizations of three X-ray rich GRBs within 0.9-6.3 hours of the burst (see Table 2.4). Yet no radio or optical afterglow has been detected from these or any other X-ray rich GRBs, raising the question of whether such bursts have unusually faint or no optical and radio afterglows. Finding the counterpart of an X-ray rich GRB would therefore be a breakthrough. During

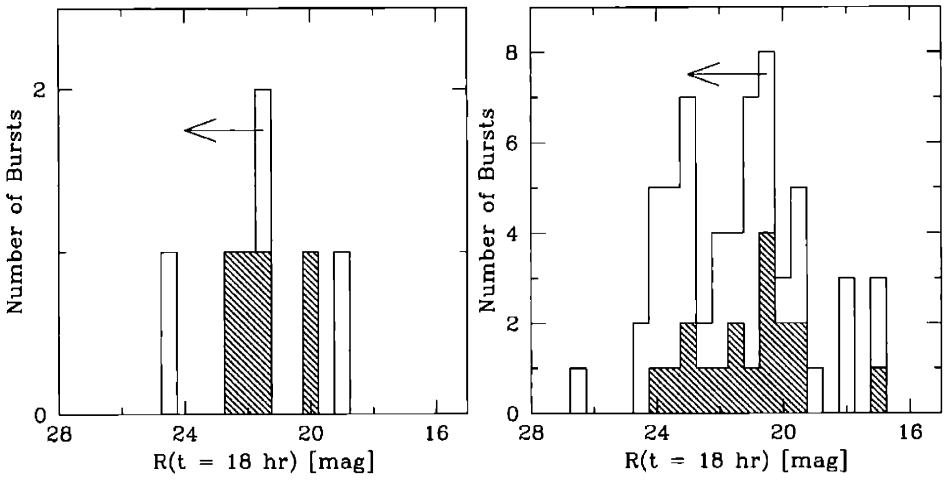

Figure 2-8: Brightnesses of the optical afterglows of *HETE* GRBs (left panel) and those of previously known optical afterglows (right panel), scaled in both cases to their R-band magnitude 18 hours after the GRB (?). The shaded boxes are detections; the open ones are upper limits (i.e., so-called "optical dark" GRBs).

the HETE extended mission, the WXM can be expected to localize an additional 12 or so "X-ray rich" GRBs, which will provide opportunities for follow-up observations to detect or set severe upper limits on optical or radio afterglows from these bursts.

2.5.4 Short GRBs

Short GRBs (Section 1.1.2; duration < 2s, Kouveliotou et al. (1993)) remain an enigma. FREGATE has detected $\approx$10 such bursts (corresponding to $\approx$ 20% of the GRBs that it has detected). Figure 2-11 shows the time history of GRB010628, one of the short burst detected by FREGATE.

To our knowledge, no previous detector has observed a short burst with an X-ray instrument having the combined energy range of FREGATE and WXM. FREGATE will detect $\sim$ 20 short bursts during the two-year HETE extended mission, bringing to $\sim$ 30 the total number of short bursts detected by HETE during its full 4-year mission. With the sensitivity and the combined energy range of FREGATE and WXM, the HETE extended mission will either localize a short burst or provide evidence that

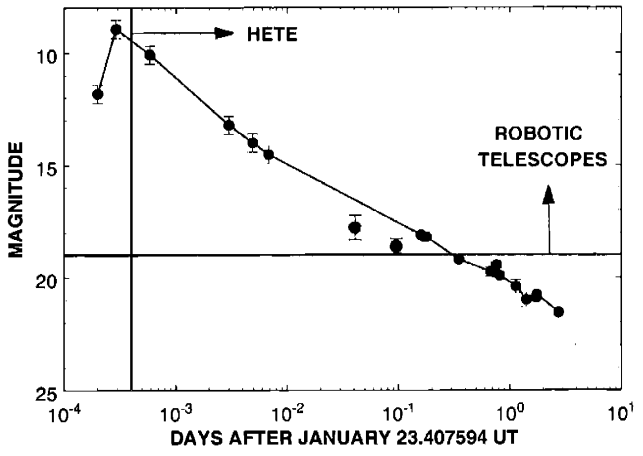

Figure 2-9: The magnitude of the optical emission associated with GRB990123 as a function of time (Galama et al., 1999). The two points slightly below the GRB990123 decay line are measurements for two recent *HETE* bursts (green: GRB020331 Kato et al. (2002); red: GRB020124 Torii et al. (2002)). The vertical line at 35s indicates a expected delay to issue the first real-time *HETE* localization notice. The horizontal line shows the sensitivities of currently operating robotic telescopes such as Super-LOTIS, ROTSE III, and TAROT-2.

spectra of short bursts are harder – and therefore more X-ray deficient – than has been thought.

On May 31, 2002 at 00:26:18 GMT, FREGATE detected, and WXM localized GRB020531, a short ($\sim$ 200 msec), hard GRB (Ricker et al., 2002f). A 43 arcminute by 67 arcminute 90% confidence rectangle was released 88 minutes after the burst, providing a unique opportunity to study a short burst at early times. 18 hours after the burst, the error box was refined by the IPN to a 46 square arcminute (3 sigma) error box (Hurley et al., 2002). This error box was observed by the VLA, *Chandra*, *Hubble*, and several ground-based optical telescopes. A possible transient source has been detected (?), with analysis ongoing at the time of this writing.

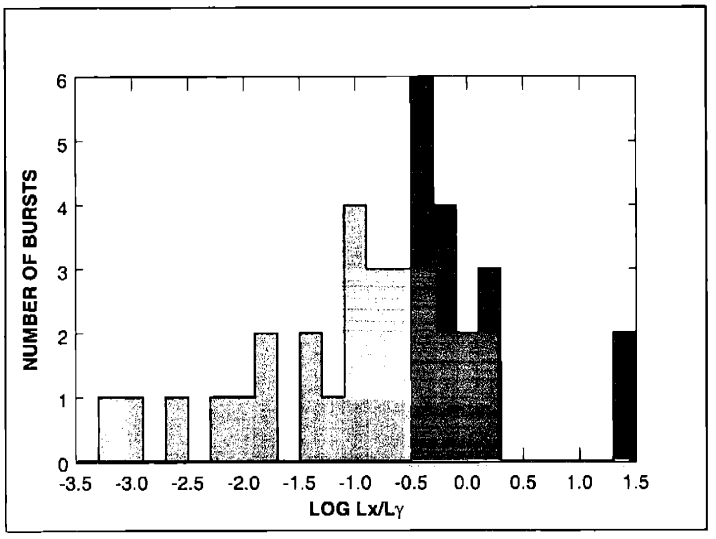

Figure 2-10: The X-ray (2-10 keV) to gamma-ray (30-400 keV) fluence ratios of HETE bursts. X-ray rich bursts are shown in red. Some outliers have been omitted for clarity. Note the tail of low L_x/L_γ bursts.

2.5.5 Emission Lines in GRB X-Ray Afterglows

The recent exciting discovery (Reeves et al., 2002) of hydrogen-like emission lines from a series of low-Z elements (Mg XII, Si XIV, S XVI, Ar XVIII, and Ca XX, and possibly Ni XXVIII) in the X-ray afterglow of GRB O11211 demonstrates that X-ray observations of such emission lines can strengthen the association between GRBs and the deaths of massive stars, provide unique information about the nucleosynthetic yield of Type Ib/Ic supernovae, and reveal the dynamics of the GRB explosion (Piro et al., 2000; Reeves et al., 2002; Lazzati et al., 2002) (Section 1.3).

GRB011211 lies at a redshift $z = 2.14$, so 4 of the 5 emission lines lie below the SXC window cutoff (at 1.3 keV), and thus would not be detectable by the SXC. However, for GRBs with $z < 0.8$ (median value for the 31 GRBs with known redshift), the five lines would be accessible to SXC observations. To evaluate the possibility that the SXC might be able to detect such emission lines, we have modeled the prompt emission from a plasma with the properties reported for GRB011211 by Reeves et al,

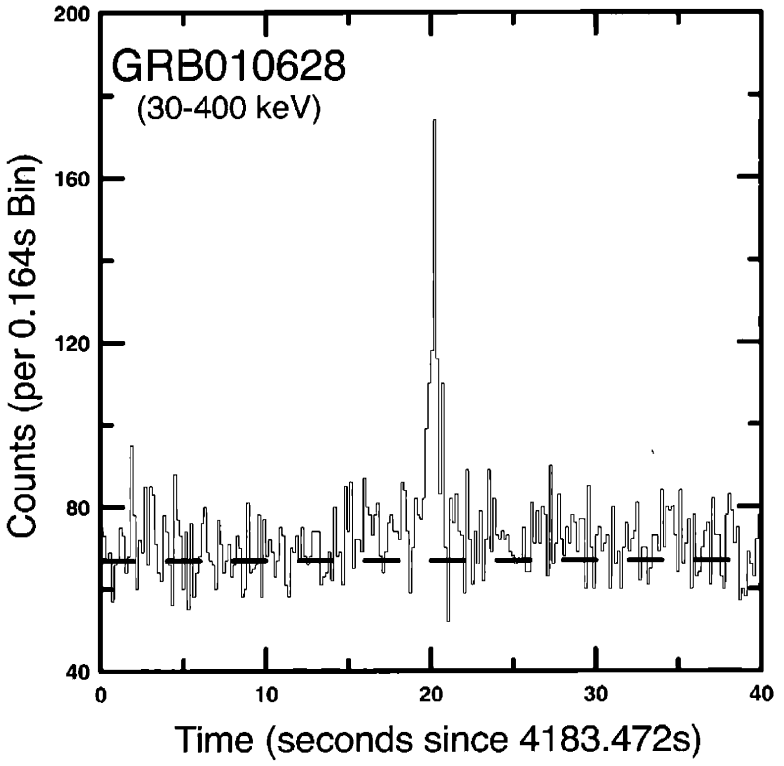

Figure 2-11: A short GRB detected by FREGATE: for this burst, T_{50}=0.5s, T_{90}=1.0.

but at a redshift of $z = 0.8$. In Figure 2-12, we show the spectrum that we would expect to measure. Our simulation assumes that the burst has a flux $\sim 5\times$ Crab and a duration of 50s. A burst with this brightness could be expected to fall within the FOV of the SXC 1-2 times per year, at favorable periods in the lunar month. As can be seen in Figure 2-12, the emission line structure is quite evident in the simulation. Thus there is a possibility that during the two-year HETE extended mission the SXC will be able to detect X-ray emission lines in the spectra of a few very bright GRBs.

2.5.6 Unsolved GRB Questions

Much progress has been made in the GRB field in the past six years. However, it would be premature to pronounce the GRB mystery solved. There is no consensus even on the nature of the central engine powering the subclass of long bursts. Is it a newly formed black hole undergoing accretion or the collapse of a rapidly spinning magnetar?

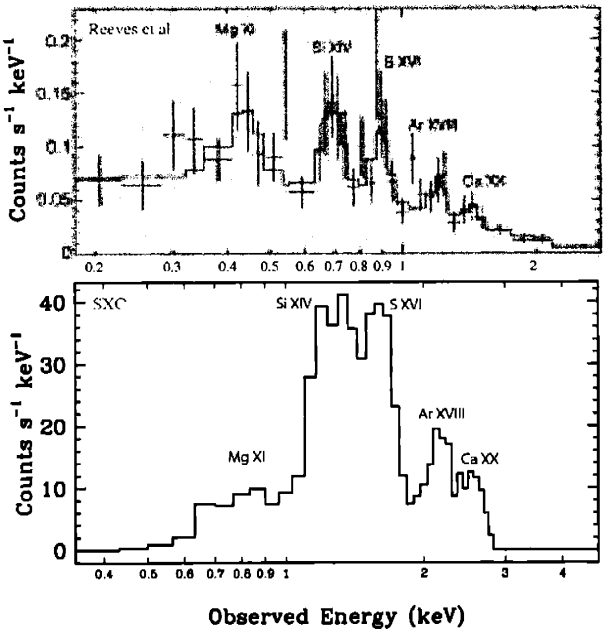

Figure 2-12: In the upper panel, the XMM spectrum of GRB011211 (Reeves et al., 2002); in the lower panel, the simulated spectrum of a bright (250 Crab-s) GRB as seen in the SXC.

If accretion, is the jet energized by black hole rotation, MHD processes in the disk, or neutrinos? Do the GRB and the supernova it produces happen simultaneously, or are they separated by days or even years (Vietri & Stella, 1999)?

Diversity of GRBs. There is also growing evidence that what we call GRBs may be a catch-all term for a diverse family of high-energy transients. Short bursts (duration < 2s; Kouveliotou et al. (1993)) remain as mysterious as ever. To these we must now add "X-ray rich GRBs" (Heise et al., 2001) and "X-ray flashes" (Heise, 2002). Is each of these a different kind of event, or is there some underlying unified model capable of producing all of them (*e.g.*, depending on the observer's viewing angle)?

Theory also predicts other classes of GRBs having longer durations than ordinary GRBs. Some may come from a first generation of stars which produced an abundance of black holes with 100 - 200 $M_{\odot}$ (Abel et al., 2002; Fryer et al., 2001), others from variations on the black hole theme (black holes made by fall back in supernovae, black

hole helium core mergers, etc). It would be surprising if nature has found only one way of making brilliant flashes of X rays and gamma rays, even at cosmic distances.

GRB–SN Connection. One possible breakthrough would be proof that long GRBs are accompanied by Type Ib/Ic supernovae (Section 1.3). An optical spectrum taken at the right epoch can confirm that the excess emission in the afterglow is supernova and not a light echo or some other modulation of the afterglow emission itself. Properties of the supernova will be constraining on the progenitor of the GRB, the total energy of the GRB, and the explosion mechanism.

GRBs as a Probe of Cosmology. *HETE* can detect GRBs out to $z \sim 20$ (see Section 1.5.3 and Figure 1-9), and may therefore provide the first identification of a very high ($z > 5$) redshift GRB. In addition, the dissemination by *HETE* of GRB localizations in near-real time should make it possible to bring to bear the Chandra and XMM-Newton X-ray observatories, as well as large-aperture ground-based optical telescopes (*e.g.*, Keck, Magellan, and the VLT) soon after the GRB. This is necessary in order to achieve high signal-to-noise, high resolution spectra of GRB X-ray and optical afterglows – a requirement for achieving the promise of GRBs for cosmology.

2.5.7 The future of *HETE*

With operations expected to last until 2004, the full HETE mission can be expected to produce totals of $\sim$ 60 localizations, $\sim$ 25 optical afterglows, and $\gtrsim$ 25 redshifts. The actual numbers are likely to be larger, as solar activity declines and the "live time" of the FREGATE and WXM instruments can be safely increased from 40 to as much as 55 minutes per orbit. There is also every reason to believe that the HETE mission will soon produce its first near real-time localization. With the mysteries that still surround GRBs and the (currently) unique capabilities of the *HETE* FREGATE, WXM and SXC instruments, the scientific promise of the extended *HETE* mission is great.

Chapter 3

Soft X-Ray Camera Design and Performance

3.1 History and conception

The *HETE-1* satellite (Figure 3-2), which was lost in November of 1996 due to failure of the Pegasus rocket, was not equipped with a Soft X-ray Camera (SXC; Section 2.2.3). Instead it had four UV CCD cameras, mounted at the four corners of the instrument side of the spacecraft, each tilted 19° from vertical, as shown in Figure 3-2. The UV cameras were chosen to increase broadband sensitivity, because at the time, it was not known at which wavelengths GRB counterparts would be detectable.

In 1997, when the rebuild of *HETE-2* (in this thesis, *HETE-2* is referred to as *HETE*) was beginning, *BeppoSAX* detected an X-ray afterglow from GRB970228 (Chapter 1; Costa et al. (1997b)), demonstrating the effectiveness of detecting GRB counterparts in X-rays. The constraints of the *HETE* rebuild meant that significant modifications of the spacecraft would not be possible, but it was recognized that the CCD readout electronics associated with the UV cameras could be used with both optical CCDs and X-ray CCDs. A total of 8 CCDs could be accommodated; one in each of four optical cameras used for aspect determination, and two in each of two Soft X-ray Cameras as shown in Figure 3-1. An optical camera is co-mounted and boresighted with each SXC module. The two optical cameras thus mounted are called

boresight cameras. The other two optical cameras are mounted on the two spacecraft corners that do not have SXC modules; these two optical cameras are designated *aspect cameras.*

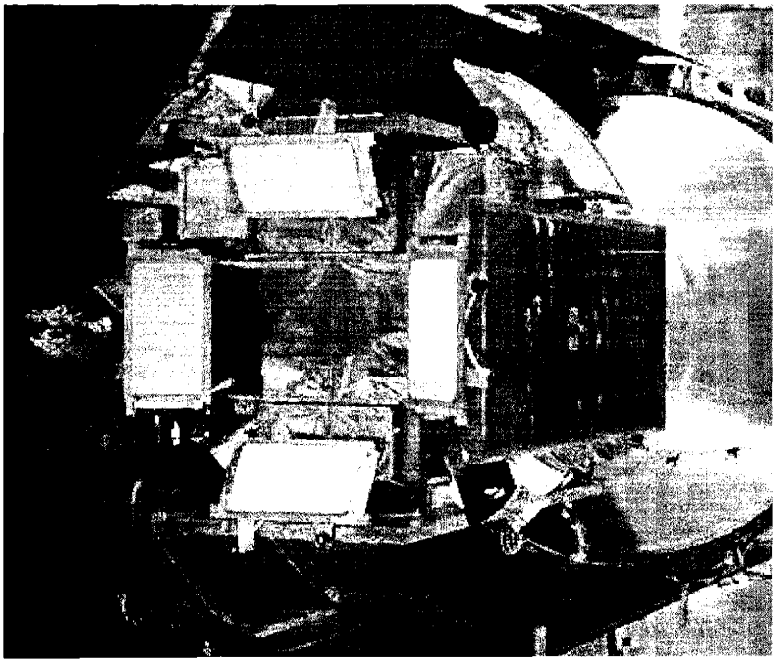

Figure 3-1: *HETE* mounted to the Pegasus rocket with solar panels stowed. The top two corners each have an SXC module and a co-mounted boresight camera. The bottom two corners each have an aspect camera, tilted at 45° .

Silicon CCDs are capable of detecting X-rays with very high spatial resolution (typically the electron charge cloud from an X-ray is localized within one or sometimes two 15μm pixels) and moderate spectral resolution with response below 1 keV. Thus, a CCD focal plane combined with a 1D coded aperture mask with comparably small features yields a 1D coded aperture camera with sub-arcminute angular resolution and a wide field of view.

The SXC (Vanderspek et al., 1999; Villasenor et al., 2002; Monnelly et al., 2002) consists of two one-dimensional coded aperture cameras with orthogonal orientation (referred to as SXC-X and SXC-Y). The imaging properties of the SXC are described in Chapter 4. A side view of an SXC module is shown in Figure 3-3. Each has a

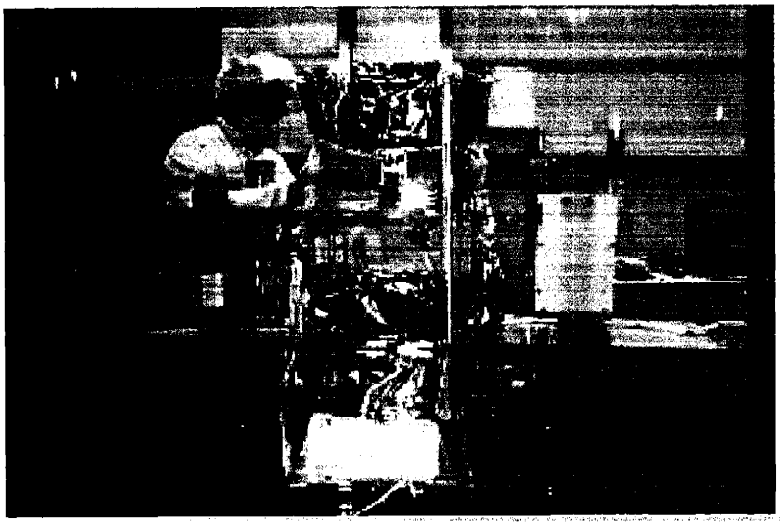

Figure 3-2: *HETE-1* was launched in 1996, but was lost due to a failure of the launch vehicle.

coded aperture mask that is 10 centimeters square with a random pattern of slits having a 45 micron feature size. Each camera has two large format X-ray CCDs with 15 micron square pixels.

The SXC was designed, built, and tested in a short time-frame and under the constraints of pre-existing spacecraft resources from the original *HETE-1* design. Development began in early 1997 at the MIT CCD Laboratory where environmental tests and CCD calibration was also performed. The SXC was delivered and integrated in mid-1999.

3.2 Requirements, Design, and Testing

3.2.1 CCD detectors

The SXC uses MIT Lincoln Laboratory CCID-20 X-ray CCDs, which are 2048×4096 arrays of 15μm square pixels. The detector size is 3.1×6.1 cm. Unlike many CCD applications where half of the array is used as a frame store to facilitate readout, the entire arrays are used for X-ray detection. Because the SXC uses a 1D coded mask,

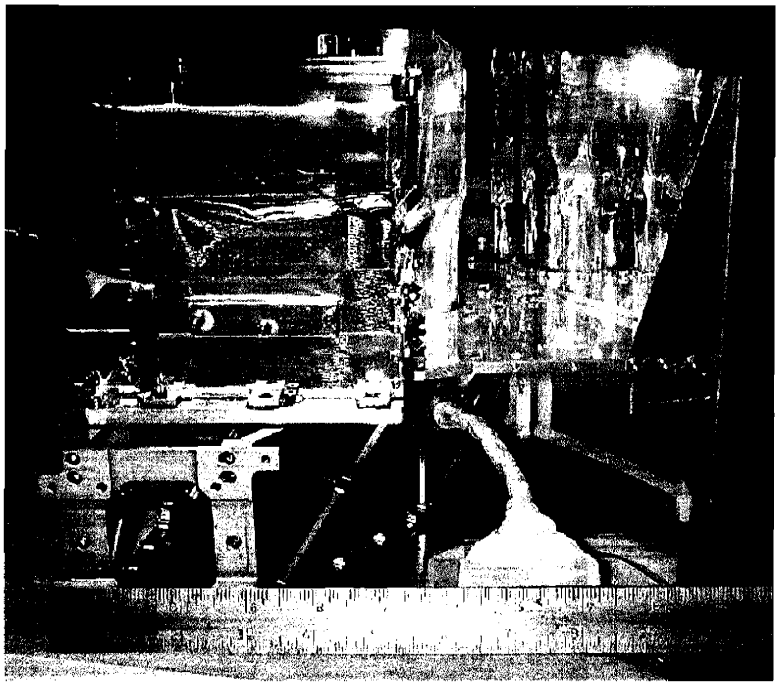

Figure 3-3: Side view of a SXC module. The cooling radiator is the curved attachment to the right, with the baseplate acting as a heat pipe. The sides of the boresight camera lens is also covered with thermal tape to allow heat dissipation.

it is only necessary to use one dimension of the CCD's two dimensional imaging capability. X-ray events are read out in a way that only captures their position along the short (2048 pixel) direction on the chip, ignoring their location on the long (4096 pixel) direction. This choice results in a considerable, and much needed, savings in limited on-board processing resources. The CCDs are read-out continuously with a 1.3 s period, which sets the limiting time resolution of the instrument.

Each SXC module focal plane (Figure 3-4) utilizes a pair of CCDs mounted on a single aluminum nitride baseplate, with a 1 mm separation along their longer side. The CCDs were aligned by GL Scientific in Honolulu to within 5 μm over their 6.1 cm length.

The CCDs are passively cooled with a radiator plate that is attached to the rear of the SXC module. The radiator is designed to maintain the CCD temperature at -50°C, which reduces dark current to a tolerable level.

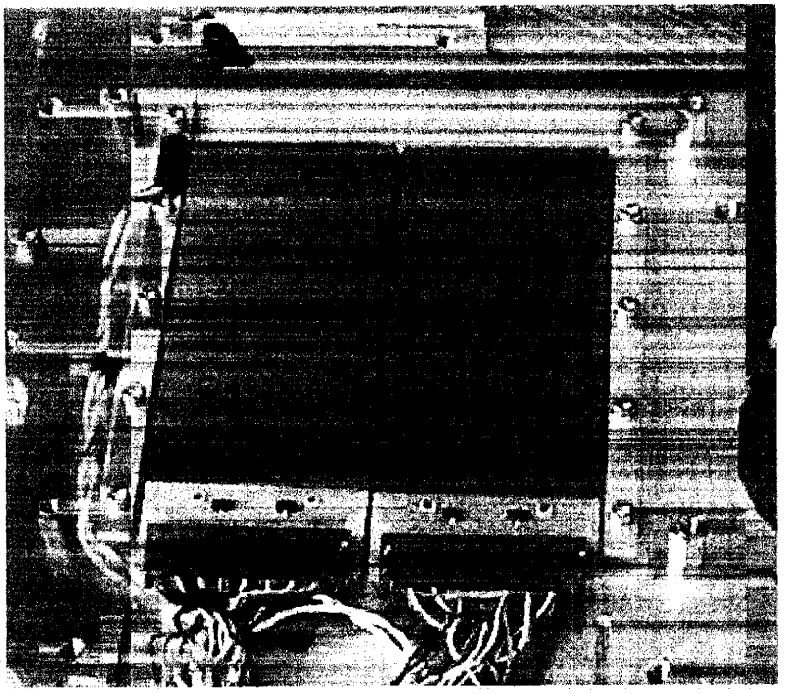

Figure 3-4: SXC focal plane showing the two CCID-20's mounted side by side on a common AlN baseplate.

3.2.2 Coded mask

The coded mask is a 10×10 cm, 25 μm thick electroformed gold sheet, fabricated by Dynamics Research Corporation in Wilmington, MA (Figure 3-6). The mask consists of a random series of open slits with a 45 μm feature size. To meet the system imaging performance goals, there are several tolerance requirements on the mask. The mask slits must remain straight and parallel with a deviation of less than 5 μm. The stainless steel mask frame must support the mask without deforming it, and the mask must not distort in the thermal stresses of the space environment.

The steel mask frame has a lower coefficient of thermal expansion than does the gold mask; thus, at lower temperatures, steel will contract more than gold. During environmental tests, it was noticed that at low temperatures, the contraction of the steel frame was permitting the mask to sag. This problem was solved by placing the mask under uniform tension, keeping the mask free from thermal distortion. Once

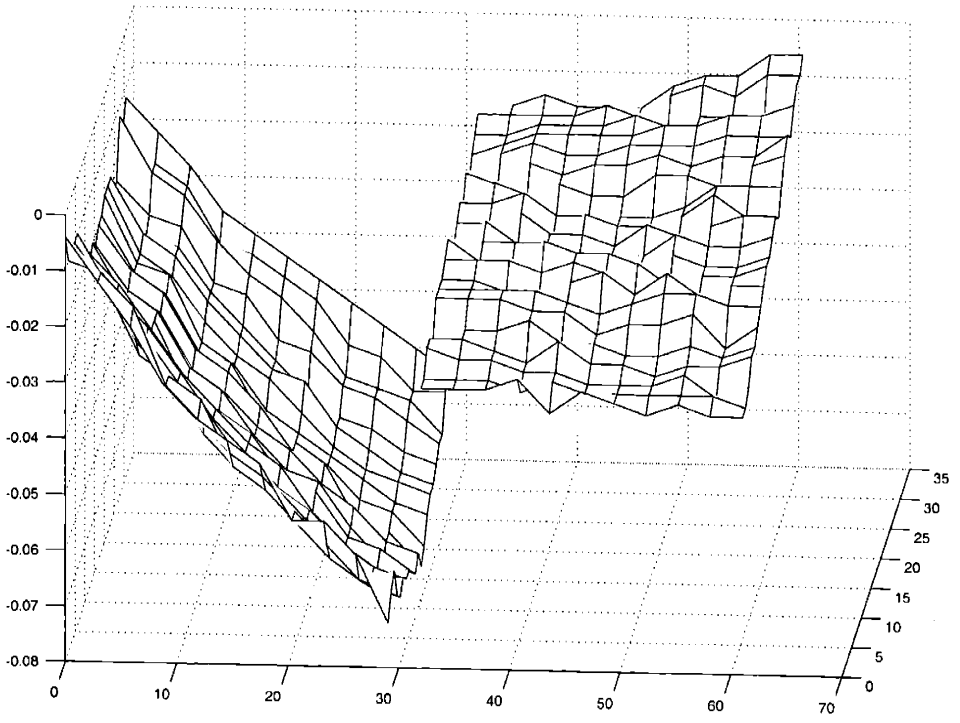

Figure 3-5: Measured surface map of the CCD on one of the focal planes showing the relative orientation. All axes are in mm. The effect of the "roll" of one CCD with respect to another can be negated through in-flight calibration.

mounted in the frame, microscopic examination of the mask showed no significant distortion. Individual slits were examined along their length under a microscope's cross-hair as the mask was moved along by a precision translation stage.

The mask pattern was generated as a series of 45 μm spaced closed or open elements. The closed-to-open ratio is 4:1, or an open fraction of 0.2. This open fraction was selected based on a signal-to-noise optimization similar to Doty (1988). The pattern is generated randomly with the constraint of the open fraction and that any closed element has at least one other closed element adjacent to it. This constraint is imposed because a lone closed element would have an increased chance of breakage. Hundreds of candidate patterns were generated and the pattern noise properties were examined. Patterns were ranked by tabulating their worst pattern noise fluctuations.

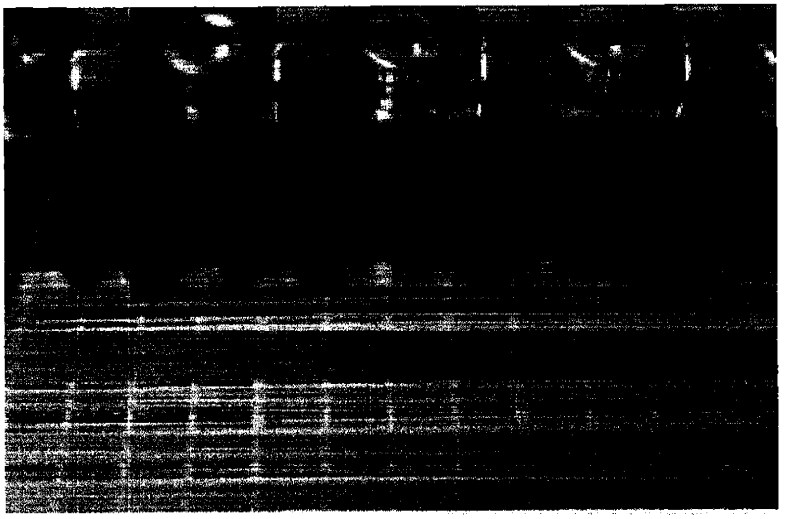

Figure 3-6: Close-up image of the edge coded mask. The smallest slits in the image are 45 μm wide.

3.2.3 Assembly and alignment tolerance

The CCDs are constructed to very precise and accurate dimensions. The mask is fabricated and mounted in its frame to similar tolerances. However, to achieve the full imaging potential of the SXC, it is also necessary that the mask and CCD be aligned to the same tolerances. This requirement derives from the fact that the CCDs are read out in a manner that captures only one dimension of information. Any rotation of the mask relative to the plane of the CCD would blur the CCD's detection of the x-rays coming through each mask slit.

An additional concern is a potential tilt of the mask with respect to the common plane of the two CCDs. A small tilt of the mask would not blur the CCD's ability to image x-rays coming through the mask. However, it would cause the pitch of the mask, as projected onto the CCD, to change slightly as a function of off-axis angle. This effect can be partially corrected with calibration, but it would be difficult to correct fully.

The effects of alignment and distortion of the mask or CCDs on the imaging properties of the SXC are summarized as followed:

Distortions and defects in the mask or CCD Limits imaging accuracy, but not significant if localized to a small area.

Rotation of mask with respect to CCD in their common plane Blurs image of mask over entire CCD, limiting imaging accuracy.

Tilt of mask with respect to CCD out of their common plane Limits imaging accuracy; if small, it can be partially corrected by calibration.

The correct relative positions of the mask and CCD are maintained by the SXC walls. To ensure proper alignment, the baseplate, walls, and mask frame were lapped flat to within a few μm. The rotational alignment of the mask with respect to the CCDs was measured with a microscope in a manner similar to the procedure for the examination of the slits (Section 3.2.2).

3.2.4 Optical blocking filter and beryllium shield

In addition to being sensitive to x-rays, the CCDs used in the SXC are also sensitive to optical light. An optical blocking filter (OBF), with a neutral density of 8, needed to block moonlight, was used to mitigate this problem. The outer OBF is a $10 \times 10cm$ square of 5000 Å polyimide and 1500 Å aluminum. This is the same design as was used on the *Chandra* HRC filters, which have an equivalent surface area. The OBF (or outer OBF) is mounted in front of the mask, so it also can protect the mask from thermal fluctuations due to heating from optical light.

There was an early concern that micrometeorites might strike and severely damage the CCDs. The OBF and mask provide some protection against this: a micrometeorite would fragment of impact with the OBF or mask so a shower of smaller, and hopefully less damaging, particles would strike the CCD. However, because the effect of micrometeorites and other space debris on CCDs was not known, we weren't able to establish with certainty that this type of shielding would provide an acceptable level of safety.

To provide additional safety against micrometeorites, and to provide backup optical light blockage, a 25 μm beryllium shield was placed in front of one of two CCDs on

each SXC module. This thickness of beryllium provides thorough protection against micrometeorites, but also reduces low energy CCD response, moving the cutoff energy from 0.5 to 1.5 keV. The beryllium shield also also blocks light from the CCDs, except for light leaking in through the edge, so it acts as an inner OBF, providing a backup for the outer OBF. The other CCD in each SXC module has no beryllium shield, and maintains its low-energy response down to 0.5 keV. Because each SXC module could still image with one CCD, the loss of the outer OBF would reduce the sensitivity of an SXC, but would not result in its failure.

3.3 In-flight performance

When the SXC was first activated a few weeks after launch, data from the cameras indicated that both were functioning nominally. However, within the first few months, problems were noticed with the instrument that have since been associated with the loss of the outer OBF (Section 3.3.1). The lack of an outer OBF makes light contamination a considerable problem for the SXC, but with the inner OBF (beryllium shield) intact and through modifications in operations and flight software, the problem is mitigated in more than 70% of *HETE*'s orbits.

For periods in the month more than 4 days from the full moon, the inner OBF (beryllium shield) on two of the four CCDs does a sufficient job of blocking out light, yielding high quality data (Figure 3-7). The two non-beryllium covered CCDs (one in each SXC module) are currently inoperable, and will not be discussed in the following pages; it is not expected that they can been made operable. Within 3–4 days of the full moon, all SXC CCDs are inoperable due to light contamination (Figure 3-8) from moonlight entering through the edges of the CCDs under the inner OBF. Thus, SXC operations can occur for approximately 20 days of each lunar cycle. Operations are also sometimes limited by scattered light from the Earth's atmosphere at dawn and dusk. Diagnosing and quantitatively evaluaing this problem, and extensive re-writing of the SXC flight software to compensate for its effects, delayed commissioning of the SXC until June of 2001. Further improvements in SXC flight software in April 2002

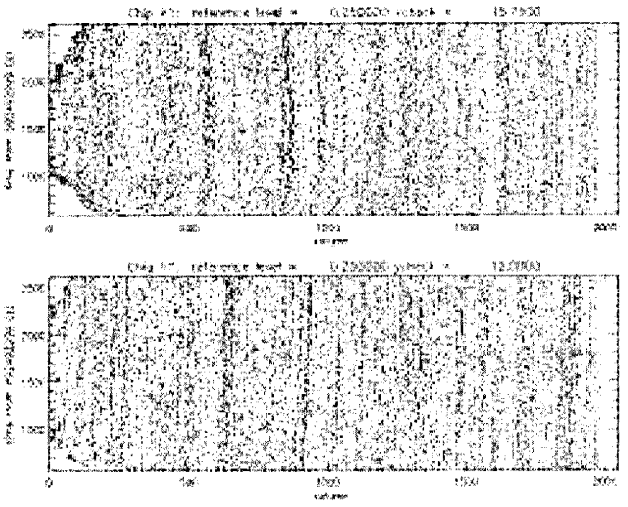

Figure 3-7: SXC CCD data with the Crab in the field of view. The CCD is read out in a one dimensional mode; in this plot, the x-axis represents the position on the CCD, while the y-axis is time, which shows where and when each x-ray strikes the CCD over the course of an orbit. Because the crab is a bright point source, it is possible to see the mask pattern, which is appears as vertical streaks. The mask pattern streaks are slightly wavy because of small drifts in spacecraft pointing over the orbit.

increased the SXC X-ray detection rate by 50%. This efficiency increase, which is largely energy independent, was achieved by improving the discrimination between real X-ray events and cosmic-ray events that are detected in multiple CCD pixels.

3.3.1 OBF damage

The outer optical blocking filters (OBF; Section 3.2.4), which are designed to protect the light-sensitive CCDs from saturation so that X-rays may be detected, were lost in the first few months of the mission. We have since concluded that their loss was due to etching of the OBF's outer polyimide layer by atomic oxygen, which was present at unexpectedly high concentrations. Atomic oxygen is quite corrosive, and at high concentrations will attack carbon based films, including polyimide. During solar maximum, levels of atomic oxygen in the atmosphere at *HETE*'s 600 km altitude can increase by two to three orders of magnitude over solar minimum levels. Atomic

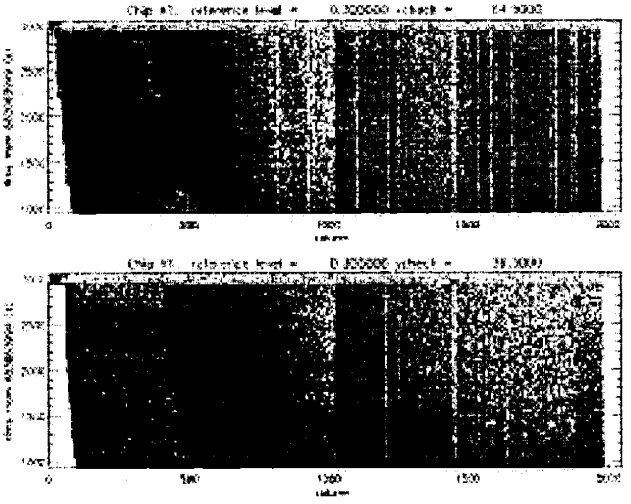

Figure 3-8: SXC CCD data with the Moon in the field of view. The axes are the same as in Figure 3-7, but the bright Moon has saturated the CCD making it impossible to detect x-rays. The SXC is normally turned off during full Moon.

oxygen does not effect the beryllium inner OBFs.

3.3.2 Iron-55 calibration source

Both SXC modules have a radioactive iron-55 (Fe^{55}) calibration source with an emission line at 5.9 keV [1]. The source is used to calibrate the CCD gain and energy resolution. Figure 3-9 shows a typical SXC CCD pulse-height spectrum with the iron line visible. Except for the strong Fe^{55} peak visible in each plot in the figure, the counts are due to the diffuse x-ray background (DXRB). The low-energy cutoff on each plot is due mainly to the beryllium filter but also to the lower CCD quantum efficiency below 1 keV due to absorption in polysilicon gates.

Before flight, gain variations were a concern because the CCDs were fabricated withour a phosphosilicate glass (PSG) coating, which is used to prevent Na contamination that could cause gain variations. As a routine and automated processing step

[1]The 5.9 keV emission line from Fe^{55} is produced by an electron capture process. An inner shell electron is captured by the iron nucleus, resulting in a Mn atom with one less proton and one more neutron then Fe^{55}. The Mn atom is initially in an excited state, and emits principally a MnK_α line upon entering the ground state

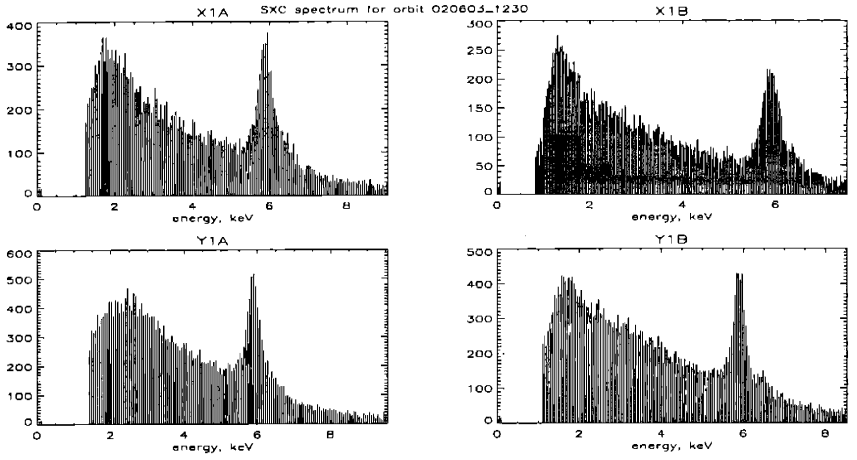

Figure 3-9: Energy spectra from each of the four CCD sectors (two on each chip), taken June 13, 2002. The strong peak on the right side of each plot is the 5.9 keV Fe^{55} peak due to the iron calibration source.

done for each orbit, the Fe^{55} peak is examined to determine its position and width, which provide continuous monitoring of gain and noise, respectively.

The Fe^{55} source is mounted just outside the mask, fully illuminating the CCDs. Figure 3-10 shows a scatter plot of pulse height and CCD column, allowing for comparison of the spectral response of each individual CCD column. The Fe^{55} counts make a dark horizontal band, demonstrating that the gain is constant among all CCD columns in the sector (there are two sectors per CCD). This is expected because all the CCD columns in a sector are read out through a common electronics chain. Note that the horizontal band shows a periodic modulation that is due to the radioactive source being above and therefore modulated by the mask. Also note the extra counts in the lower left corners of sectors X1A and Y1A, likely due to light leakage at the beginning of the orbit. The data set is integrated over an entire orbit.

3.3.3 Data cleaning

The Fe^{55} events and light contamination events add to the background in images, so to optimize the imaging performance of the SXC it is necessary to remove these events before the imaging analysis is performed. We have developed an automated cleaning

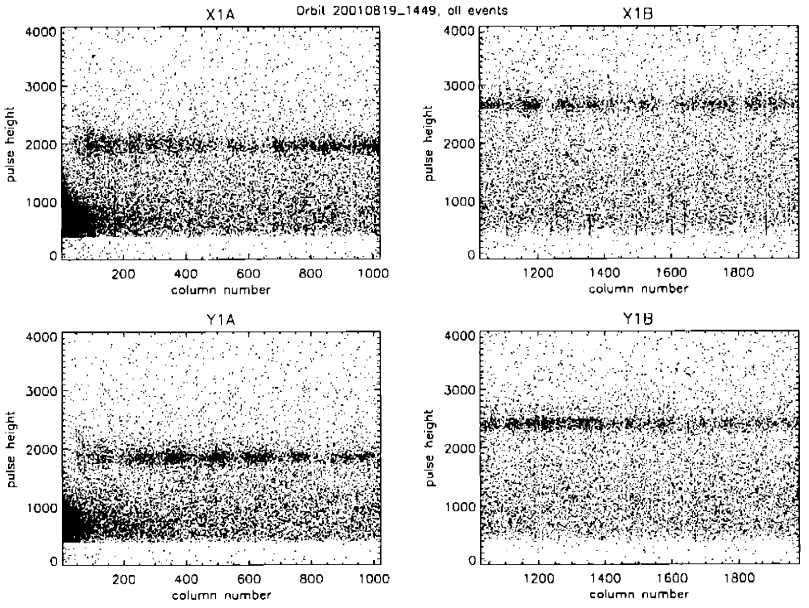

Figure 3-10: Scatter plot of pulse height and CCD column. The Fe^{55} counts make a dark horizontal band, demonstrating that the gain is constant among all CCD columns in each sector.

procedure that processes the data from each orbit before the data is analyzed. First the centroid and width of the Fe^{55} source is determined for each CCD sector (Figure 3-9). All events within 1.5 sigma of the peak are removed. Next any regions with many excess light contamination counts are removed. These cleaning steps will also remove real source counts from astrophysical objects, but this loss is outweighed by the benefit of greatly reducing the image noise.

Chapter 4

Soft X-Ray Camera Imaging and Sensitivity

4.1 Geometrical properties

The characteristic angular resolution of each SXC is 96″, set by the mask element size (45 microns) and the mask to detector distance (96 mm). The mask pattern is over-sampled three times by the 15 micron CCD pixels. Each camera has a 1.6 steradian field of view (full width, zero response) that is slightly rectangular: 65° in the resolution direction, 79° in the non-resolution direction. The fields of view of SXC-X and SXC-Y have a 1.3 steradian area of overlap, shown in Figure 4-1.

The SXCs are designed to provide accurate localizations ($\lesssim 1'$) over a wide field of view. To achieve this, the CCDs and mask must maintain precise alignment throughout each orbit. This alignment can be tested by observing the pattern of illumination on the CCDs from a bright x-ray source such as Sco X-1. Any misalignment between the mask and CCD would result in blurring of the illumination pattern (Section 3.2.3). Data collected in orbit verify that alignment has been maintained within an acceptable tolerance.

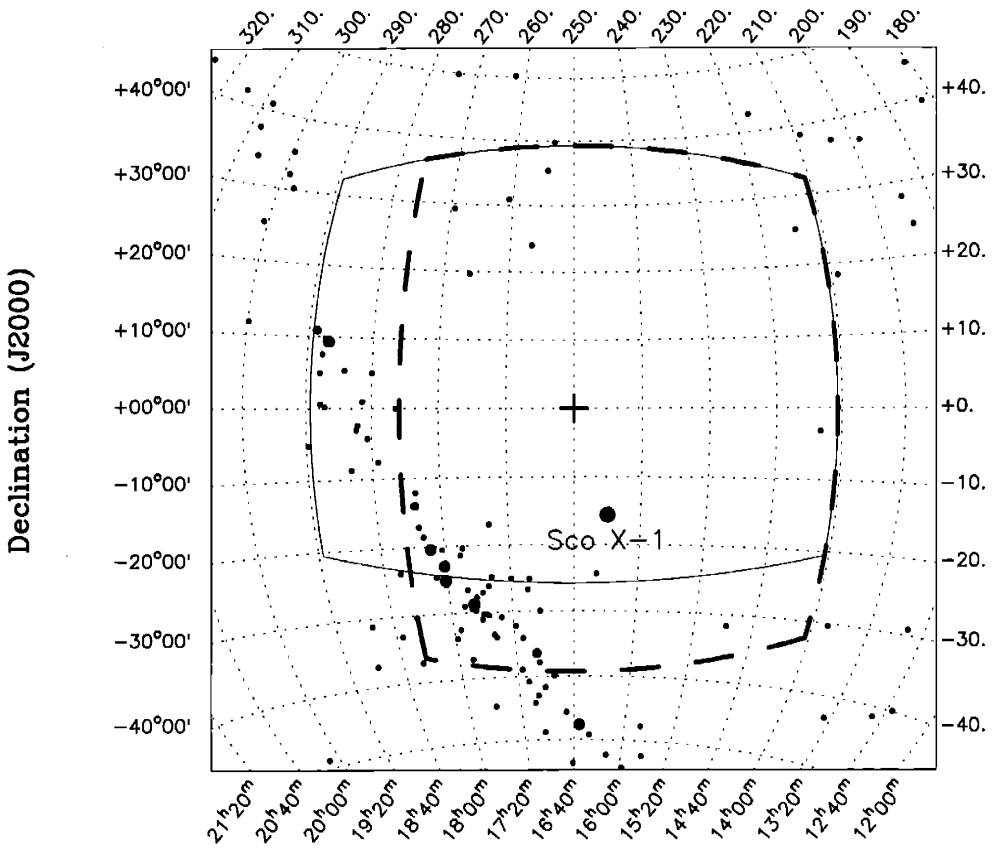

Figure 4-1: SXC fields of view: SXC-X *thick dashed*, SXC-Y *thin solid*. This view is pointing near Sco X-1, with the Galactic Center to the lower left and known X-ray sources shown as dots. Each SXC has position resolution in only one direction; here SXC-X provides right ascension, and SXC-Y provides declination.

4.2 Imaging

Imaging is performed with a one dimensional cross-correlation process where the CCD data are correlated against all possible angles in the sky. There are 2782 resolution elements, each 96″, across the 65° field of view. A celestial X-ray source will appear as a peak in the cross-correlation map, demonstrated in Figure 4-2. A detection in a single camera yields a long thin rectangle that is less than 1′ wide, and 79° long (the width of the field of view in the non-resolution direction); a detection in both SXC-X and SXC-Y can be combined to yield a celestial position with sub-arc minute

precision. Further details of the SXC localization accuracy will be discussed below.

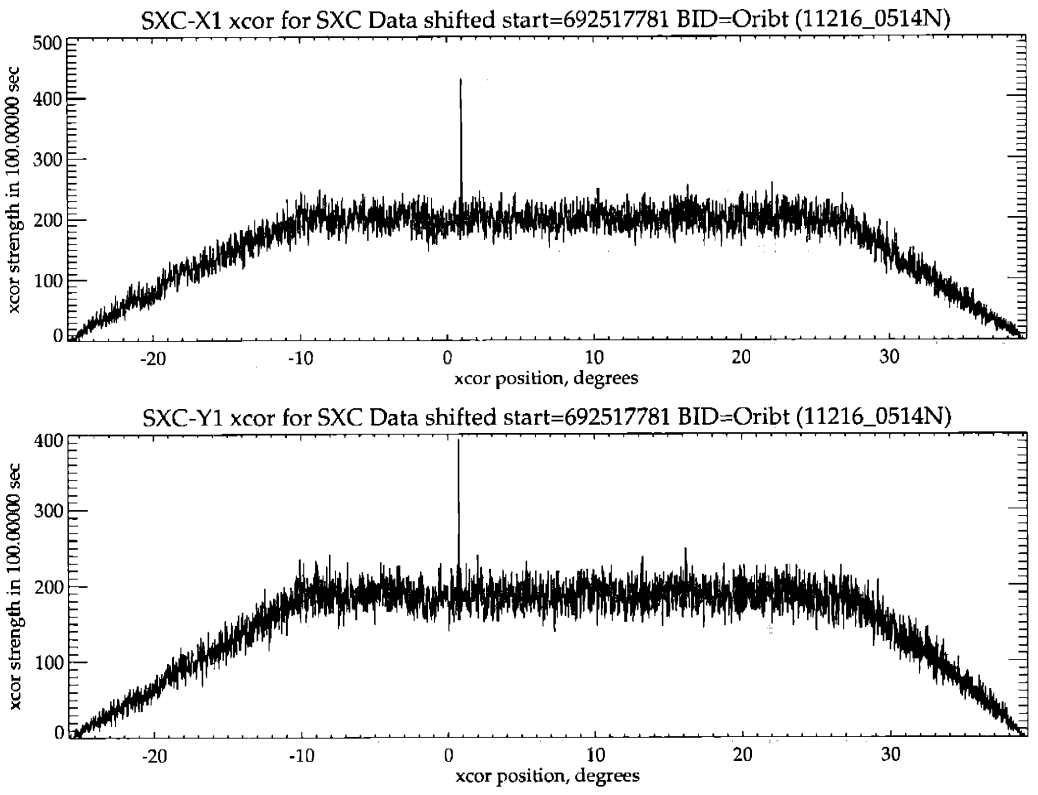

Figure 4-2: SXC one-dimensional image showing a localization peak corresponding to the Crab in both the X and Y cameras for a 100 second observation. The two one-dimensional positions can be combined to yield a celestial coordinate pair. The plateau on which the Crab sits is due to the diffuse X-ray background and X-ray sources, principally the Crab. The noise plateau slants downward near the edges as it extends to the outer limits of the field of view that are shadowed by the SXC walls, and thus are partially coded.

The pointing stability of HETE typically drifts at the arc minute level on about 10 second time scales. The drift is sufficiently small that it does not effect the WXM, but is an issue for the SXC because the cross-correlation image feature size of 96″ is finer than the aspect drift. This causes the peak from a point source, such as the Crab, to move through the cross-correlation image, as shown Figure 4-3. Without further processing, the drift timescale sets a limit on how long SXC data can be integrated to detect sources at long time scales. However, because the spacecraft aspect is tracked by the optical star cameras, we can correct the SXC data for the

aspect drift by shifting the cross-correlation image to compensate for the drift. The resulting data, as shown in Figure 4-4, have a coherent position across time, and are thus more suitable to be integrated to detect signals on longer time scales.

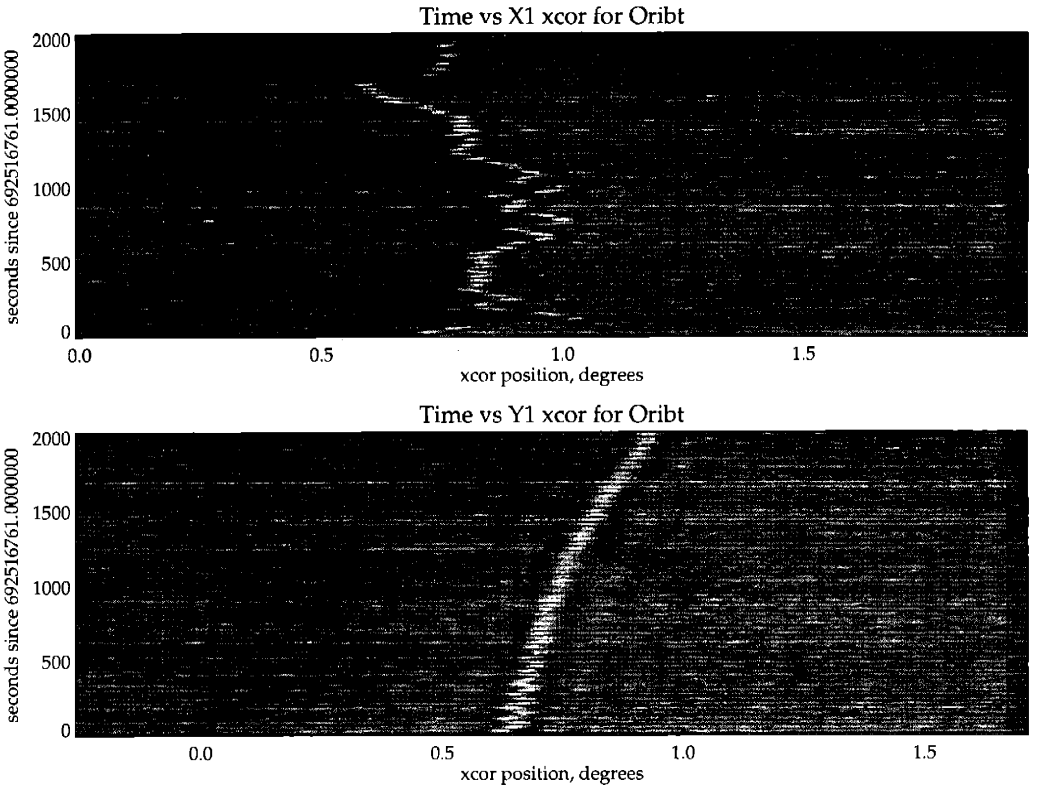

Figure 4-3: SXC image showing a localization peak corresponding to the Crab. In these plots, the y-axis spans 2000 seconds of data in 2 second steps, the x-axis labels the cross-correlation position in a restricted 2 °portion of the field of view, and the intensity of the image represents the strength of the cross-correlation at each angle and time. Because of instabilities in spacecraft aspect, the position of the Crab is seen to drift by a degree throughout the orbit.

4.3 Calibration

To optimize the accuracy of SXC localizations, and to understand their uncertainties, we have performed a series of calibration observations on known X-ray sources. Calibration observations began with observations of the Crab in December 2000 – January 2001. The calibration dataset was expanded with observations of Sco X-1 in

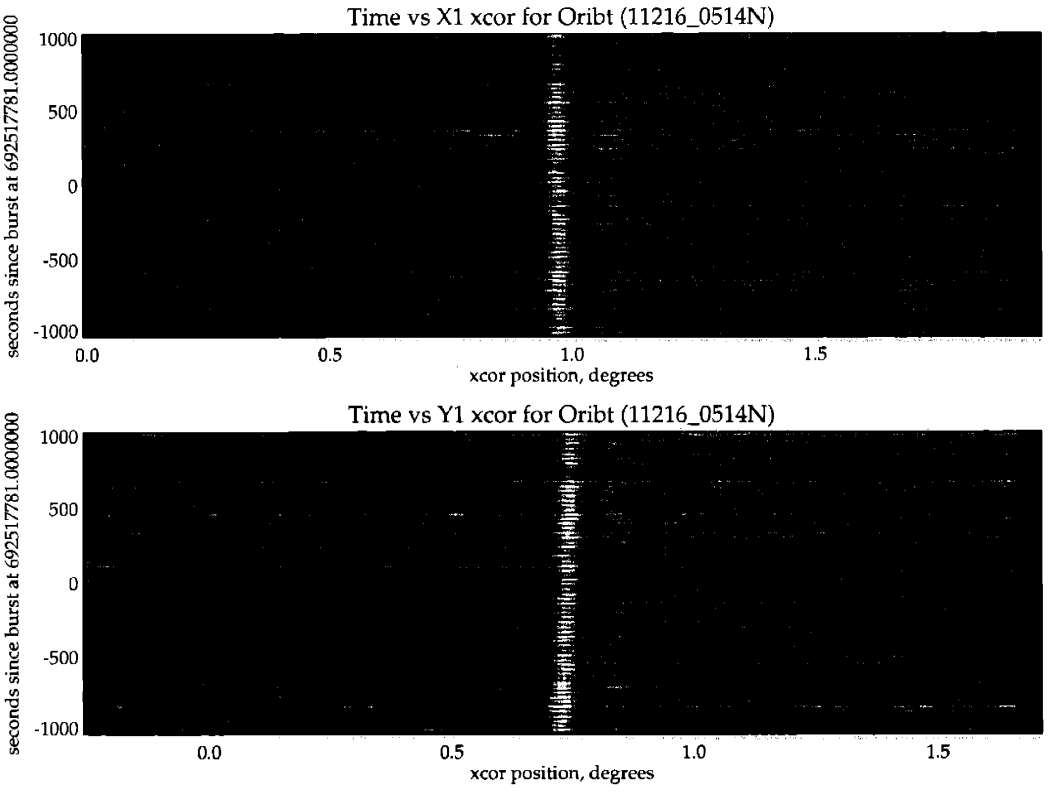

Figure 4-4: SXC image showing a localization peak corresponding to the Crab. These plots are the same as Figure 4-3, except at each time, optical aspect data have been used to shift the cross-correlation to correct for spacecraft aspect drift.

May – July 2001, and the Crab again in December 2001 – January 2002. During calibration observations, the spacecraft roll was adjusted so that the calibration source covered all areas of the SXC field of view, as shown in Figure 4-5.

Calibration data are used to determine the parameters in a simplified geometrical model of the SXC which relates positions in the crosscorrelation map to positions in celestial coordinates. The model parameters are determined with a joint fit of all calibration data with fit parameters representing the relative position of the CCD and mask, and the relative rotation between the SXC and spacecraft. The solution is combined with spacecraft aspect information, obtained from optical star cameras, to calculate positions in celestial coordinates.

Empirical measurements show a 20″ RMS localization accuracy in the X and Y directions. This corresponds to a 90% confidence error circle of 43″. Figure 4-6

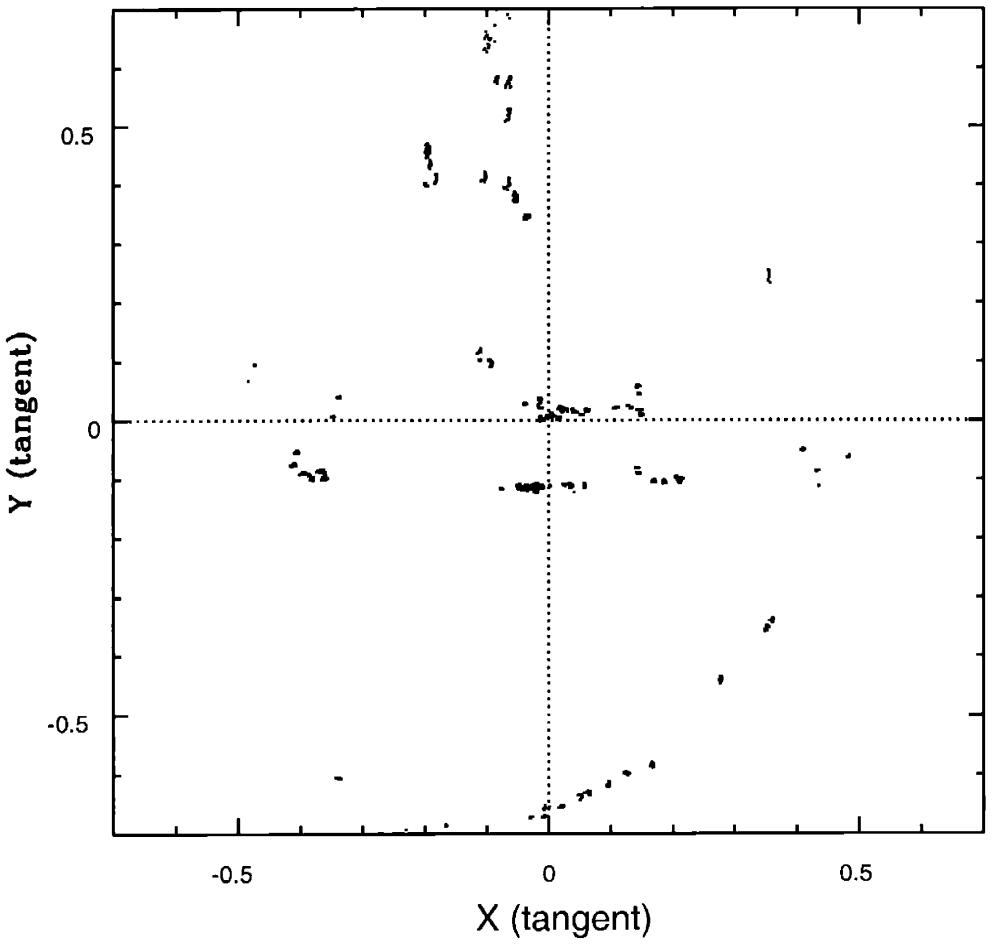

Figure 4-5: Coverage of the SXC field of view by calibration observations of the Crab and Sco X-1. The plot shows a tangent plane projection of the SXC field of view, covering an angular range of $\pm 30°$.

shows localization accuracy from multiple independent observations of Sco X-1. The largest contributor to this error is likely mechanical distortions due to periodic thermal fluctuations during each 90 minute orbit. With additional modelling, we should be able to further reduce this systematic thermal effect.

4.4 SXC as a *vernier* for the WXM

Because the SXC has a wide field of view with a fine angular resolution, resulting in a cross-correlation map with thousands of elements, only a very bright source is likely to produce a correlation peak that is brighter than all the background peaks.

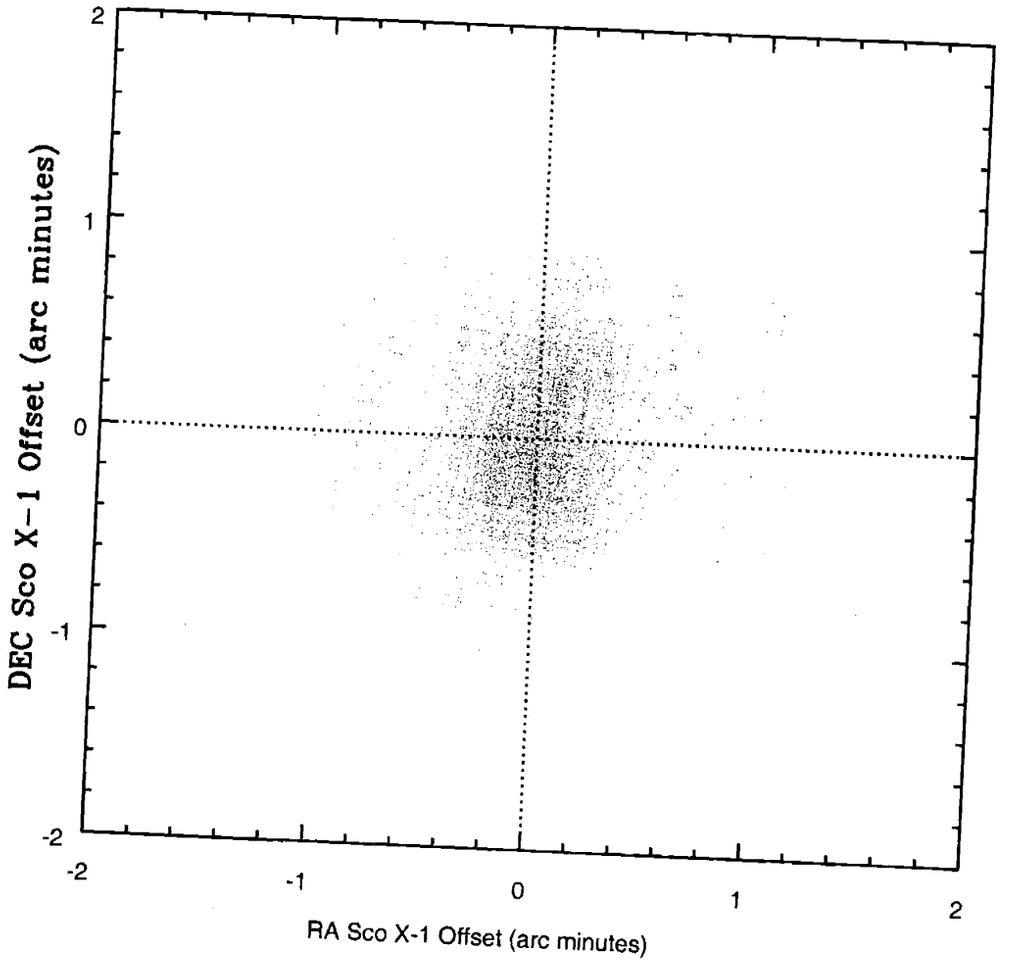

Figure 4-6: SXC astrometry: multiple independent localizations of Sco X-1 at different times and in different parts of the field of view showing 20″ RMS accuracy.

However, any source that the SXC could detect is very likely to be also detected and localized by the WXM. As a standard analysis procedure, we use the source position determined by the WXM to refine the region of the SXC cross-correlation map that is searched (Figures 4-7). Thus, the SXC serves as a *vernier* to refine the WXM localization. Typical WXM localizations are less than 15′ in radius, which is a tremendous reduction of the 65° SXC field of view (2782 resolution elements reduced to less than 20). This reduction greatly increases the chances that the true source has a higher cross-correlation strength than any background peak. However, when the search region is tightly restricted, it is difficult to tell *a priori* if the highest peak indeed corresponds to the source detected by the WXM and is not just a noise peak.

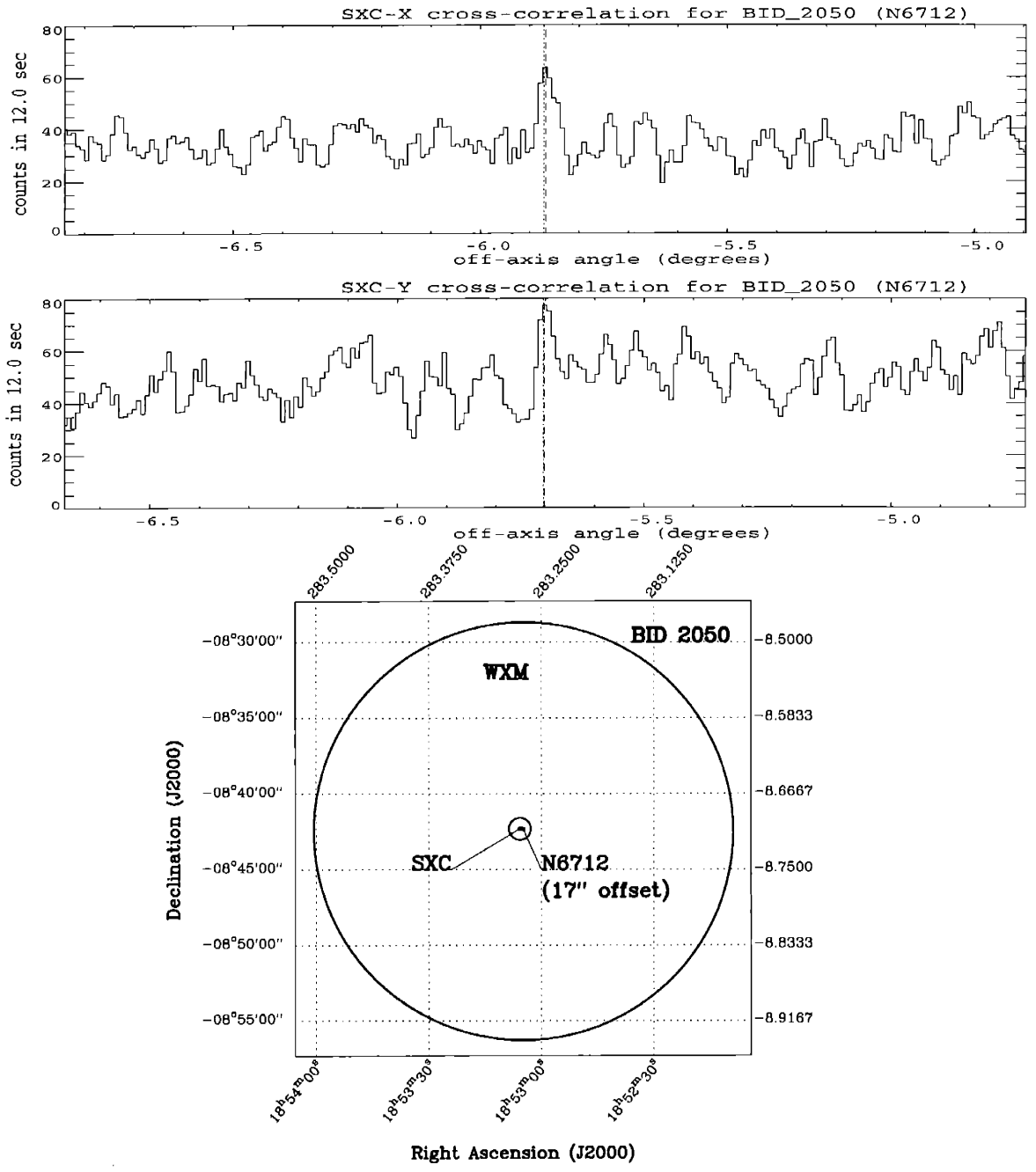

Figure 4-7: *Upper panels:* N6712 outburst on June 8, 2002, localized in SXC-X at a SNR of 3.9 and an offset of 16″ from the known source position and in SXC-Y at a SNR of 2.6 with an offset of 5.4″. The *short-dashed* line represents the known source position, while the *long-dashed* line represents the SXC localization. *Lower panel:* The SXC-X and SXC-Y positions are combined to give celestial coordinates. Note that the SXC error circle (red; 43″ radius) is considerably smaller than the WXM error circle (blue; 14′ radius).

We address the problem of possible false SXC detection in a restricted search area by increasing the search region to $\pm 1°$ centered on the WXM position. If the source is detected by the SXC then it will with very high probability fall within the WXM error region. However, if it isn't detected, then the SXC cross-correlation peak will fall at a random location in the $\pm$ 1° search region. For example, if the WXM error region is 1/10 of the SXC search region in one dimension, and the SXC peak falls within the WXM error region in for both the X and Y cameras, then there is only a 1% chance that it is a false detection.

At this time the SXC has not yet detected X-ray emission from a Gamma Ray Burst. Of all the GRBs detected by the WXM, none were detected by the SXC because of its smaller field of view (Figure 4-1), its reduced duty cycle (due to full moon constraints) or its lower sensitivity. However, a number of Galactic X-ray sources, both steady and transient, were detected while HETE was pointed at the Galactic Center during the summer of 2001 and 2002. In June of 2002 a series of tests were initiated where *HETE*'s on-board trigger system was configured to trigger on XRBs with *HETE* pointed at the Galactic Center (normally when the Galactic Center is in view, low energy trigger thresholds are set to not respond to the $\sim 5-10$ XRBs detected per day.) These tests were done to verify the WXM's ability to generate accurate flight localizations that are sent out to the GCN with less then one minute of delay, and to demonstrate the SXC's ability to provide refinements, based on ground analysis, of the WXM positions. During three days of testing, five XRBs were localized (Table 4.4). Four of these (BID 2050, BID 2052, BID 2057, and BID 2063) were two-axis detections, one (BID 2055) was a one axis detection. BID 2050, BID 2052, and BID 2063 were released as GCN Alerts with delays of 3-7 hours (BID 2050: Figure 4-7, BID 2052 and 2063: Figure 4-8). With increased automation, the typical delay will soon drop to less than two hours.

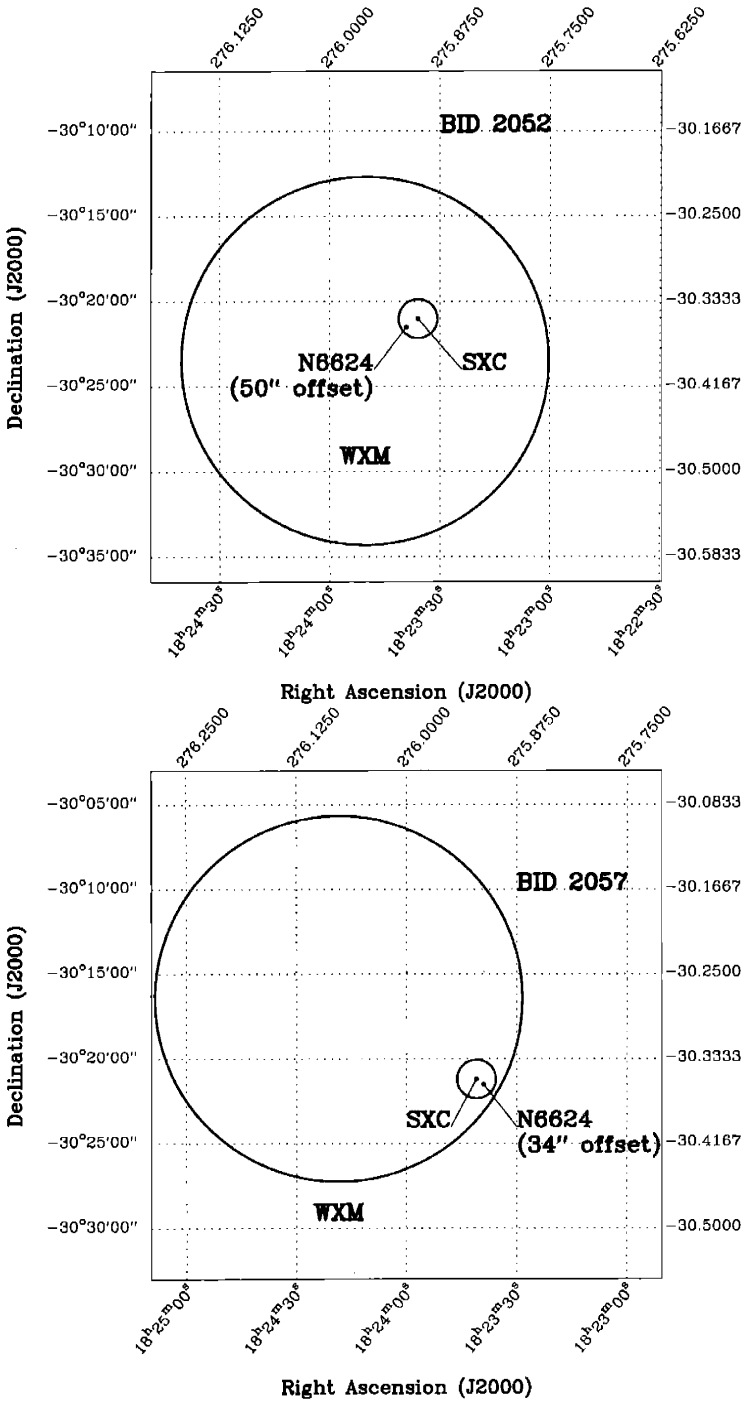

Figure 4-8: SXC and WXM error regions for two XRBs, as released in GCN Alerts.

Burst ID	Date (2002)	Time (UT)	Source	Axis	localization offset	SNR	Delay $(hrs)^1$	Remarks
2050	8 June	1059	N6712	x	16″	3.9	7.1	Good aspect;
				y	5.4″	2.6		Sent to GCN
2052	8 June	1602	N6624	x	27″	4.8	3.7	One aspect point;
				y	42″	4.1		Sent to GCN
2055	9 June	1304	N6624	x	–	–	1.6	Good aspect
				y	14″	2.9		
2057	9 June	2045	N6624	x	31″	2.9	3.8	Good aspect;
				y	14″	3.9		Sent to GCN
2063	10 June	1935	N6712	x	19″	8.1	0.75	High aspect drift;
				y	60″	7.2		Sent to GCN, but GCN was down

[1]With automated alerts turned on, these times will drop to less than 2 hours.

Table 4.1: Five XRBs localized by the SXC during three days of observations of the Galactic Center in June of 2002.

4.5 Sensitivity

Typically the SXC count rate is dominated by the diffuse X-ray background, which yields 15 cts/s in each of the two SXC cameras. During January and December, the Crab is in the SXC field of view giving a count rate of 4 cts/s per camera when it is on axis. With the increase of 50% in X-ray detection efficiency achieved in April 2002 (Section 3.3), the Crab count rate is projected to be 6 cts/s per camera.

An analysis of 2000 seconds (one orbit) of SXC data from December 12, 2001 when the Crab was 1.19° from the SXC boresight is used to characterize the sensitivity to a 1 Crab source. Using the technique described above of searching the SXC cross correlation map within ± 1° of the known Crab position, we check how consistently the Crab is detected. A detection is defined as the brightest cross correlation peak being within 2′ of the known Crab position. Integration times of 1, 2, 5, and 10 seconds are used to simulate a Crab-like transient with these durations (Table 4.5). Because the SXC has a very consistent background count rate, the sensitivity to constant sources for any integration time should be very similar to the sensitivity to transient sources, such as GRBs, with duration equal to that integration time.

Integration (sec)		% correct	
Before Apr 2002	Current	SXC-X	SXC-Y
1	0.67	71	74
2	1.33	82	82
5	3.33	91	93
10	6.67	97	99

Table 4.2: Consistency of detecting the Crab during 2000 seconds (one orbit) of data taken with the Crab on-axis. This number is representative of the SXC's ability to detect a 1 Crab GRB with a duration equal to the integration time. The integrations listed in the "current" column are adjusted to reflect flight-code improvements in April 2002 that yielded a 50% increase in event detection rate. For example, with the current sensitivity, a 3.3 Crab-sec source will be detected with $> 90\%$ reliability in both axes.

The Crab data used in this estimate were taken before April 2002 when flight-code improvements yielded a 50% increase in event detection rate. Because the increase is approximately energy independent, the sensitivity can be re-calculated by simply noting that an integration of x seconds before April 2002 is equivalent to a $\frac{2}{3}x$ second integration after April 2002. The current sensitivity to a 1 Crab source, adjusted accordingly, is shown in Table 4.5.

The SXC sensitivity can also be characterized in terms of integration time and flux threshold for a given signal-to-noise ratio (SNR). We set the SNR threshold at 3.5σ, which by itself is a low significance, but there is additional information that makes this level reasonable, predicated on the fact the analysis of SXC data will based on a WXM detection. First, the time of the burst will be known from WXM and likely FREGATE as well. Second, the WXM-localization allows the SXC to act as a vernier; it is only necessary to search a small part, and not the entirety of the SXC field of view. Because we are using this additional information to restrict the SXC analysis, it is possible to set a low threshold of 3.5σ, which for a burst of duration t seconds gives a sensitivity (compared to the Crab flux) of $1.9t^{-1/2}$ Crab.

4.6 Summary, conclusions, and ongoing work

The SXC is currently performing consistently, localizing sources with a 20″ RMS accuracy, corresponding to a two dimensional 90 percent confidence error radius of 43″. Because of the loss of the optical blocking filter, the SXC has lost half of the CCD collecting area, and cannot operate within 4–5 days of the full moon. The SXC has not yet localized a GRB, but has demonstrated its ability to reliably detect and localize transient X-ray sources with detections of Galactic X-ray transients. With recent adjustments of CCD readout leading to a 50 % sensitivity increase, we expect to get at least a one sided localizations for the majority of WXM-localized GRBs, excluding burst that are out of the SXC FOV or times when the SXC is turned off due to full moon.

Chapter 5

Observations of GRB 011212 and GRB 020331

The greatest progress in the study of GRBs has come from prompt follow-up observations (within $\sim$ 1 day) of GRB positions with optical telescopes. Beginning with optical observations of the *BeppoSAX* error box of GRB 970228 (Section 1.2), optical observations have identified GRB redshifts and studied host galaxies (Section 1.2.1), and contributed to the broadband study of afterglows, GRB energetics and the GRB surrounding environment (Section 1.2.6).

We have a program in place to study *HETE*-localized GRBs with the Magellan consortium's 6.5m Baade telescope (hereafter *Magellan*) at Las Campanas Observatory in the Chilean Andes at an altitude of 8000 feet[1]. We use both the MagIC and LDSS-2 instruments. MagIC, the Magellan Instant Camera, is a 2048 $\times$ 2048 direct CCD camera with a 2.36′ square field and a 0.069″/pixel plate scale. LDSS-2, the Low Dispersion Survey Spectrograph, is a high efficiency, wide-field multi-slit spectrograph, which in imaging mode has a 6.4′ diameter field with a 0.38″/pixel plate scale.

The primary goal of our observation program is to identify an optical afterglow counterpart within *HETE* error circles. This is done by comparing a single epoch

[1]http://www.lco.cl/magellan_lco

observation to the Digitized Sky Survey (DSS), or by comparing two separate epoch observations and looking for a source that has faded. If the counterpart is identified by our or other observations, we monitor the source's lightcurve, and attempt to measure its spectrum, or perform multi-color photometry. Typical WXM GRB localizations are $\lesssim 10'$, so the wider field of view of LDSS-2 is preferable over MagIC; Figure 5-3 shows an example of how the error circle of GRB 020331 was covered with a mosaic of 7 pointings. If the counterpart is identified, then MagIC is the preferred instrument for photometric observations because it has greater sensitivity, and its finer pixel plate scale offers better sampling of the point spread function, which is helpful in searching for a host galaxy underlying the afterglow.

5.1 GRB 011212

The *HETE* FREGATE and WXM instruments detected and localized GRB 011212 on December 12 at 04:04:02 UT (December 12.169). The burst was not detected by in-flight analysis (it was an "untriggered event") but was later detected by ground analysis, and an error region centered at $\alpha^{2000} = 05^h00^m05^s$, $\delta^{2000} = +32°07'39''$ with a total error radius of $11'$ (90% confidence region) was reported as a GCN Circular (Ricker et al., 2001g) on December 12.597, 10.3 hours after the burst. The event is classified as an X-ray rich GRB, and has a duration of > 80 seconds.

In the FREGATE 8-85 keV band, a total of 3724 counts were detected during the burst interval, corresponding to a fluence of $\sim 6.7 \times 10^{-7} cm^{-2}$ and an SNR of 9.8. The peak flux was $\sim 1.8 \times 10^{-8}$ergs $cm^{-2}s^{-1}$ (i.e., $\sim 0.5\times$ Crab flux), assuming a Crab-like spectrum. In the WXM $2 - 25$ keV band, the burst had an SNR of 6.9.

Further analysis of WXM data gave a refined location for GRB 011212 of: $\alpha_{2000} = 05^h00^m16.3^s, \delta^{2000} = +32°08'35''$ with a total error radius of $9'$ (90% confidence region). The duration in the WXM 2-10 keV band was > 80 s. A total of ~ 3500 counts were detected during that interval.

5.1.1 RXTE/ASM localization

It was soon discovered that the All Sky Monitor (ASM) on the Rossi X-ray Timing Explorer (RXTE) had also detected GRB 011212. The combined *HETE* and ASM error regions, which overlapped significantly, was published as a GCN Notice on December 12.78, 14.7 hours after the burst. The combined overlap region (Figure 5-1) reduces the error region from 254 to 50 square arcminutes.

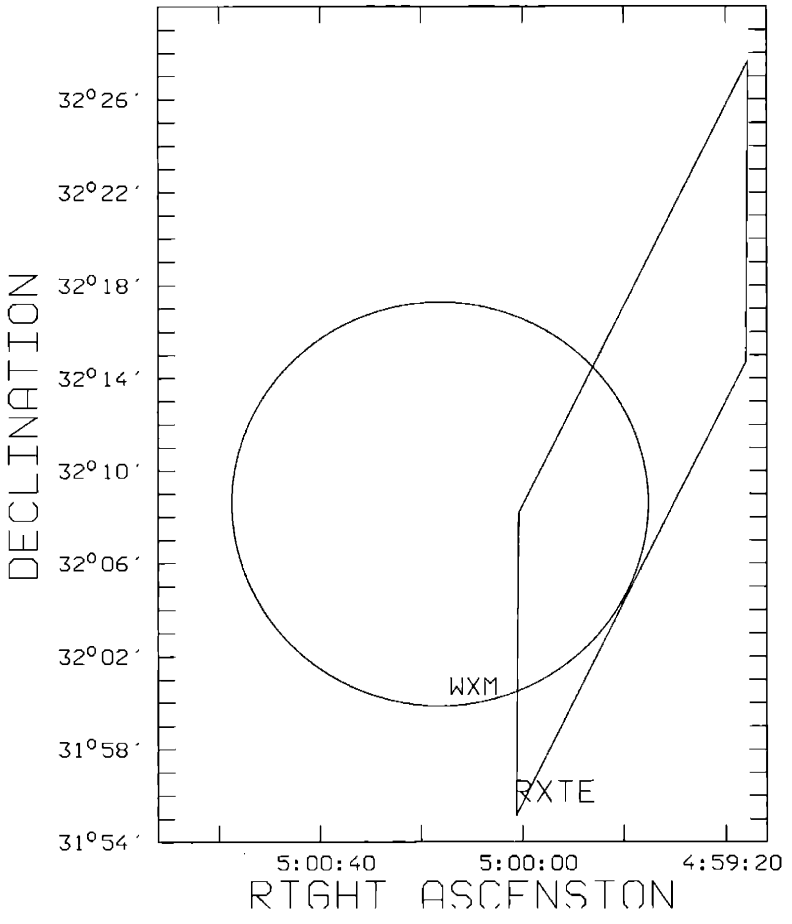

Figure 5-1: Localization region of GRB 011212, showing the *HETE* WXM refined localization and the RXTE ASM localization. The overlap region has an area of 50 square arcminutes.

5.1.2 Optical observations

A number of optical follow-up observations of the HETE/ASM error region were reported as GCN Circulars. These observations are summarized in Table 5.1.2. The earliest observation were 0.38 days (9.1 hours) after the burst by Kinugasa et al. (2001) with the Gunma Astronomical Observatory's 150-cm telescope, covering 90% of the region. In comparison with a second epoch of identical observations taken 1.38 days after the bursts, the authors detect no optical afterglow candidate brighter than $R = 20.5$.

Table 5.1: Optical observations of the *HETE*/ASM error box of GRB 011212 reported in *GCN Circulars*.

Mo/Day (2001)	Delay (days)	Observatory	GCN #	Coverage	Filter	limit	comment
12/12	0.38	Gunma 150-cm	1210	100%	R	20.5	
12/12	0.64	Oslo 0.25-m	1201	100%	R	18.5	
12/12	0.68	Terskol 2.0-m	1206	$\sim 85\%$	R	21.5	
12/13	0.98	Palomar 48-inch	1196	100%	R	21	
12/13	0.98	Mt. Ekar 1.8-m	1205	$\sim 80\%$	R	22.7	
12/13	-	USNOFS 1.0-m	1198	100%	BVRcIc	-	calibration
12/13	1.15	USNO 1.3-m	1216	100%	Ic	21.6	
12/13	1.38	Gunma 150-cm	1210	100%	R	20.5	
12/14	2.00	Magellan 6.5-m	1324	100%	R	24.5	Epoch 1
12/13	2.08	USNO 1.3-m	1216	100%	Ic	21.6	
12/14	3.00	Magellan 6.5-m	1324	100%	R	24.0	Epoch 2
02/16/02 02/17/02	67	U. Hawaii 2.2-m	1324	100%	VR	24.5	Epoch 3

The deepest exposure within one day of the burst was by Saracco et al. (2001) with the Mt. Ekar 1.8-m telescope, reaching a limiting magnitude of $R = 22.7$ at 0.98 days after the burst (Saracco et al., 2001). The deepest exposure within two days was our *Magellan* observation , reaching a limiting magnitude of $R = 24.5$ at 2.00 days after the burst (see below).

We observed the error box of GRB 011212 with the Baade 6.5m telescope at Magellan on 2001 December 14.17 UT (Epoch 1) and December 15.17 UT (Epoch 2) using the MagIC CCD detector. Twelve 360s R-band exposures were used to mosaic the entire HETE and RXTE/ASM joint error box on each night. Both night's

observations had seeing of 0.7″ and achieved a limiting magnitude of 24.5, except for the last half of the second night when the seeing decreased slowly to 1.3″ , with a limiting magnitude of 24.0 on the last frame. Third epoch observations were made with the University of Hawaii 2.2m telescope on Mauna Kea on 2002 February 16.33 and 17.38 UT. Three frames were used to mosaic the error box each with three 600s VR-band [2] exposures under conditions of 1.3″ seeing, giving a limiting magnitude of 24.5 after summing.

Aperture photometry was performed on all objects detected in the Epoch 1 images and then again at the same positions in the later epochs. The absolute magnitude of each source was calculated using a nearby USNO catalog star: for each source, the same calibration star was used in all epochs, and the quoted error in the magnitude does not include the uncertainty in the magnitude of the calibration star. Comparison with Epoch 3 is complicated by the fact that it is in VR-band, whereas Epochs 1 and 2 are in R-band. Four sources (Figure 5-2) were measured to have faded between both Epochs 1 and 2 and between Epochs 1 and 3. Their positions and magnitudes are listed in Table 5.1.2. Sources 2, 3, and 4 faded to near the detection limit in Epoch 2, and to below the detection limit in Epoch 3. The detection of fading behavior in these three sources is marginal with respect to the measurement error. The observed fading and upper limits are consistent with a temporal power law decay index between -1 and -2, except for source 1 in Epoch 3, but this flattening of the decay could be due to an underlying galaxy.

Table 5.2: Fading sources detected in optical observations of the *HETE*/ASM error box of GRB 011212.

Source	α_{2000}	δ_{2000}	Epoch 1 R-Band	Epoch 2 R-Band	Epoch 3 VR-Band
1	4:59:58.1	+32:02:57	23.14 ± 0.12	23.89 ± 0.22	24.08 ±0.24
2	4:59:59.4	+32:03:43	23.80 ± 0.18	24.65 ± 0.39	> 24.5
3	4:59:59.0	+32:09:04	23.75 ± 0.18	24.80 ± 0.48	> 24.5
4	4:59:39.5	+32:08:34	23.38 ± 0.12	24.41 ± 0.38	> 24.5

[2]VR is not a standard photometric band, see ?) for details

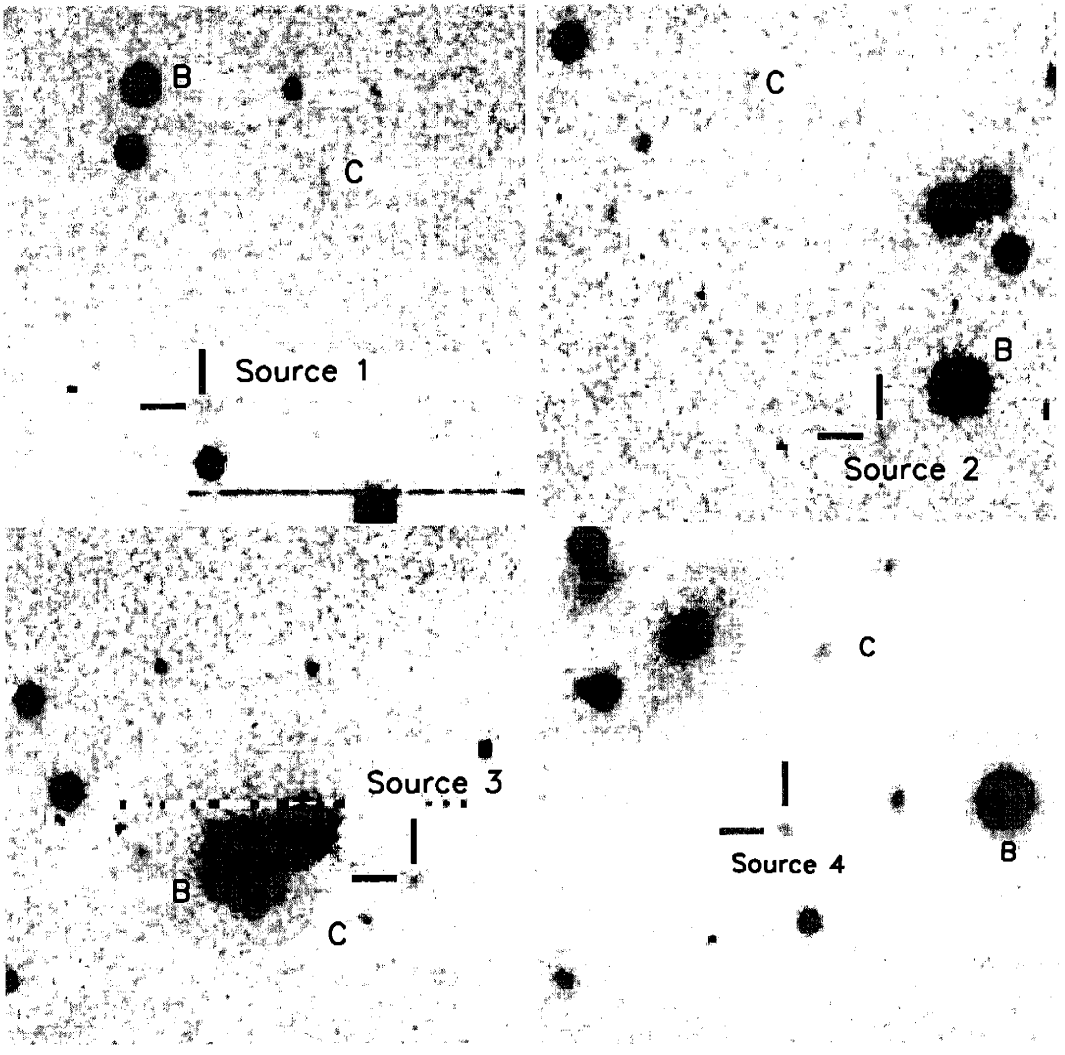

Figure 5-2: Finder chart of the four candidate sources from the Epoch 1 observations of GRB 011212 (see Tables 5.1.2 and 5.1.2). The charts contain the source, marked by cross-hairs, a bright star (B) from the USNO catalogue, and a constant star (C) of comparable magnitude to the source. The charts have a width and height of 33 arcseconds in RA and Dec. North is up and East is to the left.

Table 5.3: Finder chart stars for Figure 5-2: optical observations of the *HETE*/ASM error box of GRB 011212.

Source	$R(source)$	R(Star B)	R(Star C)
1	23.14 ± 0.12	18.8(USNO)	23.65 ± 0.15
2	23.80 ± 0.18	16.9(USNO)	23.59 ± 0.15
3	23.75 ± 0.18	14.4(USNO)	23.48 ± 0.14
4	23.38 ± 0.12	16.8(USNO)	23.11 ± 0.09

5.1.3 GRB 011212: Conclusions

Though the 10 hour delay in releasing the position is long compared to typical *HETE* performance, it was sufficiently rapid to permit several deep optical observations covering the error region, reaching a limiting magnitude of $R = 22.7$ one day after the burst and $R = 24.5$ two days after the burst. Our follow-up observations at later epochs detected several candidates, but none are convincing because they are all close to the limiting magnitude of the observation. With early, deep optical observations and no transient detected, GRB 011212 can be classified as an "optically dark" GRB (Section 1.5.2). Reichart & Yost (2002) show that most dark bursts are a result of extinction by a dense circumburst medium.

5.2 GRB 020331

At 16:32:28.76 UT on 31 March 2002, the *HETE* FREGATE and WXM instruments detected GRB 020331, a long (~50 sec) GRB. A GCN Alert Notice was issued at 16:39:31 UT. A preliminary localization was reported as a GCN Position Notice at 17:12:51 UT, ~40 min after the burst. Further ground data analysis produced a refined location of $\alpha_{2000} = 13^h16^m22.7^s, \delta^{2000} = -17°55'23''$, with a 90% confidence error circle radius of $8'$, released as a GCN Circular (Ricker et al., 2002e) at 21:05:38 UT.

In the FREGATE 8-40 keV band, GRB 020331 had a duration of ~ 20 ". A total of 2320 net counts were detected during that interval, corresponding to a fluence of $\sim 4 \times 10^{-7}$ ergs cm^{-2}. The peak flux averaged over 0.85 s was $\sim 1 \times 10^7$ ergs cm^{-2}s^{-1} (ie 4× Crab flux). In the WXM 2-25 keV band, the localization SNR was > 9.

5.2.1 Optical observations

The optical transient (OT) was detected by Fox et al. (2002) as a fading source in a difference image from Palomar Hale 200-inch telescope observations on 2002 Apr 1.40 and 2.38 UT. The OT faded from $R \sim 21$ to $R \sim 21.6$. Following this discovery, the source was detected in analysis of several earlier observations, including observations by Kato et al. (2002) with 25 cm and 30 cm telescopes located at Kyoto University taken 47 minutes after the burst. This is the earliest detection of a *HETE* OT. However, it should be noted that the detection had a SNR of only 2.0σ. Table 5.2.1 summarizes all optical observations of GRB 020331 that were published as GCN Circulars, excluding our *Magellan* observations, which are detailed in Table 5.2.1 and Figure 5-4.

Table 5.4: Optical observations of the *HETE* error box of GRB 020331 reported in *GCN Circulars*.

Mo/Day (2002)	Delay (days)	Observatory	GCN #	Coverage	Filter	*OT*	limit
03/31	0.033	Kyoto 25-cm, 30-cm	1363[1]	100%	$\sim Rc$	17.9	-
03/31	0.07	RIMOTS 30-cm	1344[2]	100%	R	-	14.9
03/31	0.10	SSO 40-inch	1316[3]	60%	R	19.5	19.3
03/31	0.10	AAT 3.9-m	1322[4]	50%	Ks	detected	-
04/01	0.34	Calar Alto 3.5-m	1317[5]	90%	K′	-	19
04/01	0.52	KPNO 0.9-m	1318[6]	100%	R,I	-	$R \sim 19$
04/01	0.60	KPNO 2.1-m	1320[7]	50%	J,H,K	-	-
04/01	0.71	Palomar 200-inch	1334[8]	100%	i′	~ 21	$R \sim 23$
04/02	1.69	Palomar 200-inch	1334	100%	i′	~ 21.6	$R \sim 23$
-	-	USNOFS 1.0-m	1319[9]	60%	BVRcIc	photometric cal	

[1] Kato et al. (2002), [2] Kawai et al. (2002), [3] Price & Begam (2002), [4] Price et al. (2002b). [5] Klose et al. (2002), [6] Hartmann (2002), [7] Ohta & Akiyama (2002), [8] Fox et al. (2002), [9] Henden (2002)

We first observed the *HETE* error circle of GRB 020331 with the Baade 6.5m telescope at Magellan on 2002 April 1.22 UT (12.7 hours after the burst) using LDSS-2 (Monnelly et al., 2002). Seven 90s R-band exposures were used to mosaic the entire *HETE* error circle (Figure 5-3). The limiting magnitude was R = 23.5, with $0.6''$ seeing. The OT was detected at $R = 21.05 \pm 0.11$, with magnitudes calibrated against star G020331 (R = 18.945) from the photometry of Henden (2002).

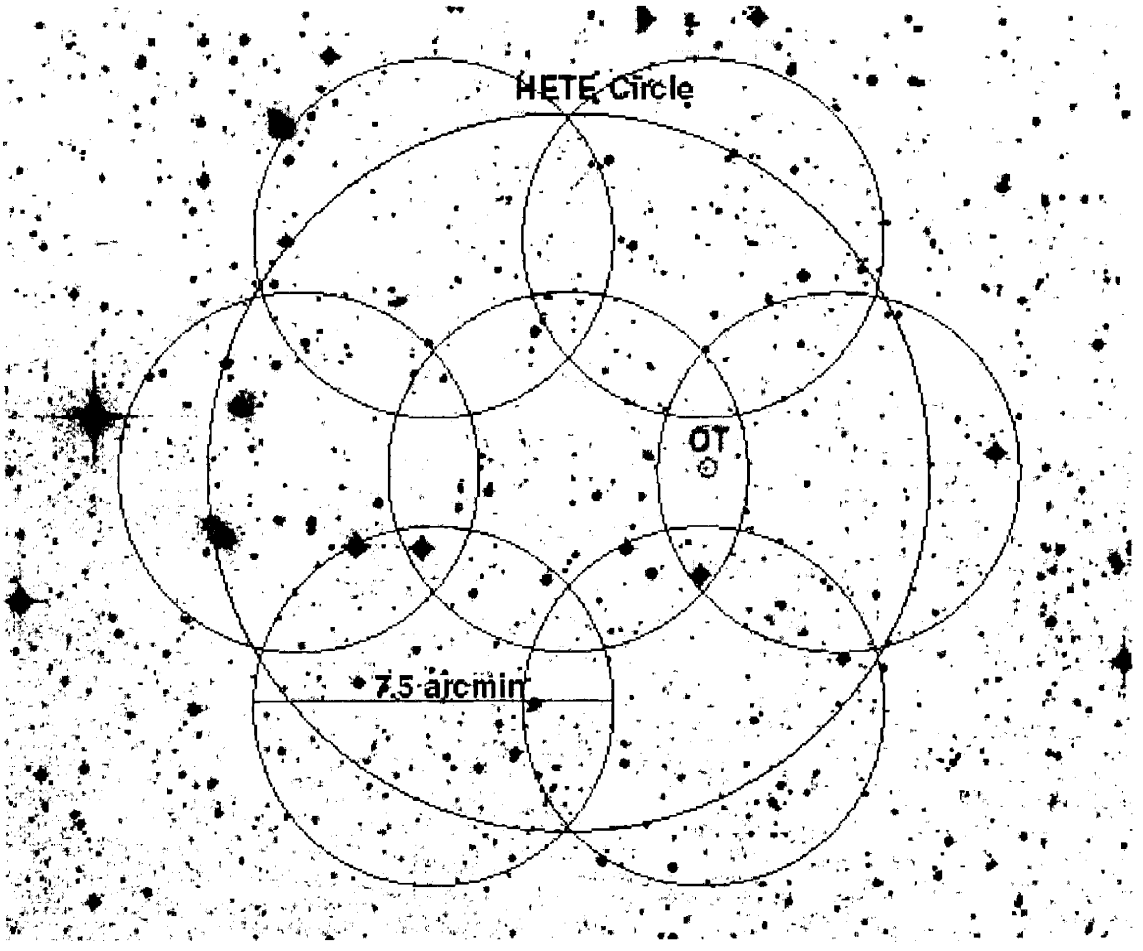

Figure 5-3: DSS image of GRB 020331 region showing location of optical transient (OT), *HETE* error circle (16′diameter, 90% confidence), and 7 LDSS-2 pointings (7.5′ diameter FOV).

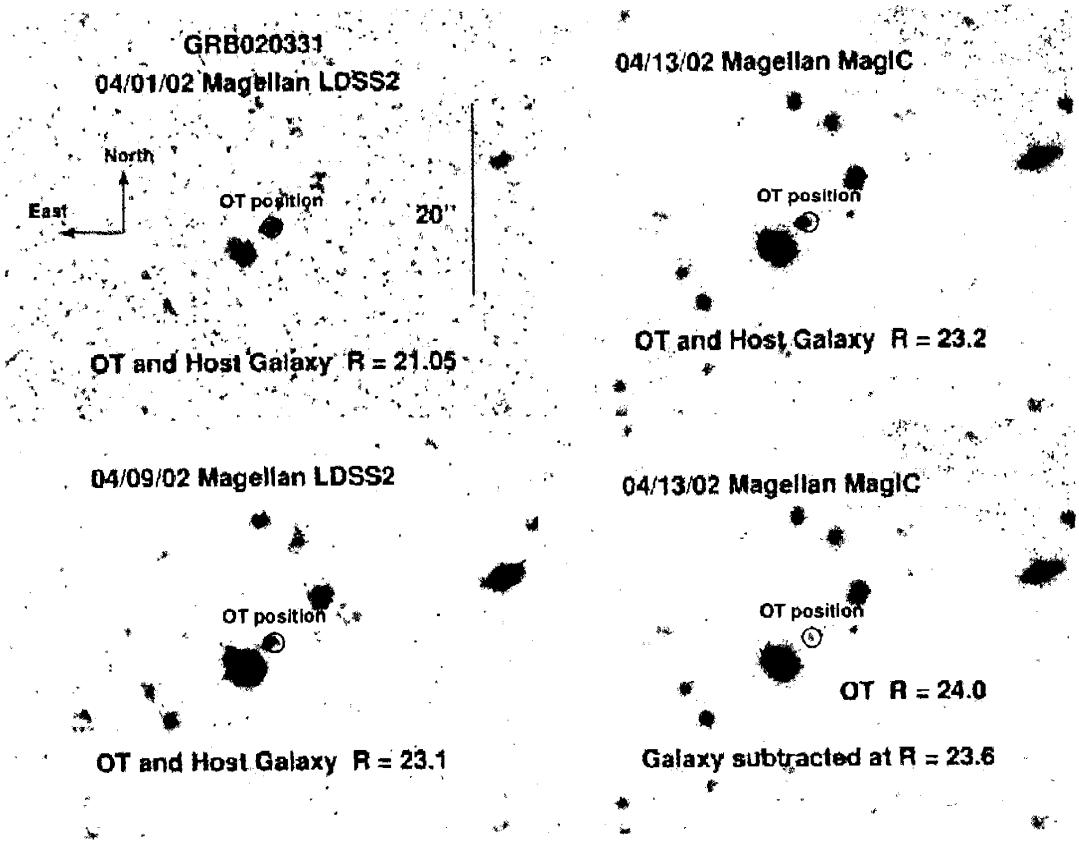

Figure 5-4: *Magellan* images of GRB 020331 at three Epochs. *Top left:* First epoch observations with *Magellan*/LDSS-2 shows the optical transient at $R = 20.05$. The OT position from this image is used in all four images. *Bottom left:* Second epoch observations with *Magellan*/LDSS-2, the optical transient has faded below the host galaxy, so the centroid is seen to shift to the galaxy position. *Top right:* Third epoch observations with *Magellan*/MagIC. This higher resolution image shows the galaxy offset 0.8 $''$ from the original OT position. Bottom right: Third epoch MagIC image, a point source at $R = 23.6$ is PSF-subtracted from the galaxy position revealing a weak detection of the OT.

Table 5.5: Optical observations of the *HETE* error box of GRB 020331 with the *Magellan* 6.5m Baade telescope on three nights between April 1 and 13, 2002.

Mo/Day (2002)	Delay (days)	Instrument	GCN #	Coverage	Filter	*OT*
04/01	0.53	LDSS-2	1339	100%	R	21.05 ± 0.11
04/09	8.37	LDSS-2	1346	OT	R	23.1 ± 0.1
04/13	12.53	MagIC	1382	OT	R	23.2 ± 0.1

We obtained second epoch observations at *Magellan* on 2002 April 9.06 UT using LDSS-2. Second epoch observations took place 8.37 days after the burst, and 7.84 days after our first epoch observations. Two 200s R-band exposures were used to image a $7.5'$ diameter region centered on the coordinates of the the OT. We detect the OT at $R = 23.1 \pm 0.1$. In comparison to our first epoch measurement, with exactly the same instrument configuration, the afterglow candidate declined by 2.0 ± 0.2 magnitudes in R.

We obtained third epoch observations at *Magellan* on 2002 April 13.21 UT using MagIC. Third epoch observations took place 12.53 days after the burst, and 12.00 days after our first epoch observations. One 300s and three 600s R-band exposures were stacked to image a $2.4'$ square region centered on the OT. The OT is detected at $R = 23.2 \pm 0.1$. In this observation, the centroid position of the OT is offset by $0.8'' \pm 0.1''$ to the east, and the source is extended in the east-west direction, through the original OT position. We interpret the extended source to be the host galaxy of the optical counterpart: the GRB optical counterpart has faded below the directly-detectable limit. Our *Magellan* observations are summarized in Table 5.2.1.

5.2.2 Light curve and host galaxy

We have constructed an R-band light curve based on our *Magellan* observations at three epochs and two other detections reported as GCN Circulars (Table 5.2.1): Kato et al. (2002) (R=17.9 at 0.033 days), and Price & Begam (2002) (R=19.5 at 0.10 days). Because of the close $0.8''$ separation between the center of the host galaxy and the GRB afterglow, all photometric measurements represent the sum of both

components. Optical afterglows are not well studied at very early times (a few hours of the burst), but theory and observations (Section 1.2) suggest that the power-law decay will not have a constant slope over the range of times in the observations, 0.033 days to 12.53 days. However, there is insufficient sampling of the lightcurve to fit for more than one power-law.

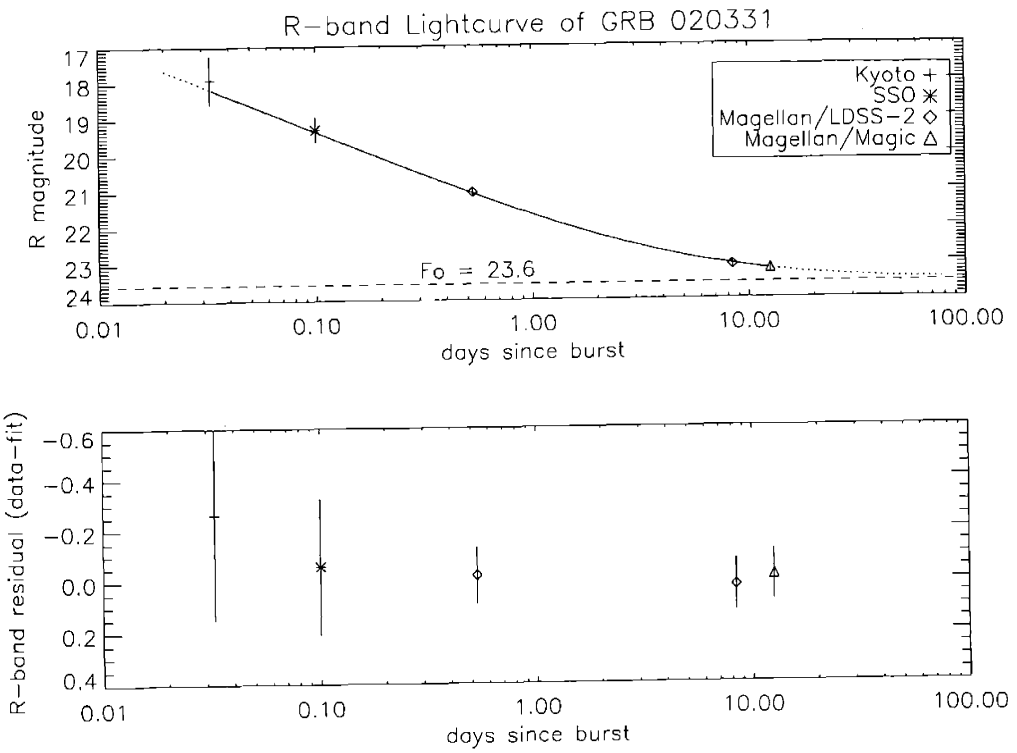

Figure 5-5: *Top panel:* R-band lightcurve of GRB020331 (see Table 5.2.1) showing a fit with decay-law $\alpha = 1.00$ plus a constant component $R_{gal} = 23.6$. Extrapolation of the lightcurve before and after the data is shown as a dotted line. There is insufficient data to constrain changes in α at early times. The constant component, which we interpret as a host galaxy, has $R_{gal} = 23.6 \pm 0.1$ (dashed line). *Bottom panel:* Residuals of data minus fit for the R-band lightcurve.

We perform a least-squares fit of the R-band flux to a power-law for the afterglow plus a constant term for the host galaxy: $F_R(t) = F_0 + F_1 t^{\alpha}$. Figure 5-5 shows the fit to all 5 R-band data points. Taking F_0 to correspond to the R-band magnitude of the galaxy, R_{gal}, we find $\alpha = 1.00$, $R_{gal} = 23.6$, and $\chi^2/d.o.f. = 0.18$. To account for a

possible change in α with time, we repeat the fit with the earliest data point (R=17.9 at 0.033 days) excluded and find the same result but with $\chi^2/d.o.f. = 0.11$. Our fit is consistent with an unchanging α, but the sampling is insufficient to exclude a possible change in α. However, accurate measurements at late times with *Magellan* effectively constrain the measurement of $R_{gal} = 23.6 \pm 0.1$.

The fit to the R-band photometric data treats the sum of the galaxy and OT light, but the two objects are marginally resolved in the third epoch *Magellan* data with MagIC, making it possible to examine each separately. We find that PSF subtraction of a $R = 23.6$ point source from the position of the galaxy effectively removes the galaxy light except for a faint source at $R = 24.3 \pm 0.2$ at the original OT position (Figure 5-4. This is reasonably consistent with the lightcurve fit which predicts $R_{OT} = 24.6$ at this epoch.

5.2.3 GRB 020331: Conclusions

GRB 020331 is the fifth *HETE* localization to yield an afterglow counterpart detection. We find that the R-band lightcurve between 47 minutes and 12.35 days after the burst is consistent with a power-law decay $\alpha = 1.00$ plus a constant component at $R = 23.6$, which we attribute to the GRB host galaxy. In our second and third epoch observations, the optical transient is dimmer than the galaxy and can be seen offset by $0.8'' \pm 0.1''$ to the east.

Chapter 6

X-Ray Observations of GRB 011130 with *Chandra*

X-ray follow-up observations of GRB error boxes have proven to be an effective tool for studying GRBs (section 1.2). Observations of GRB 970228 with *BeppoSAX* identified a fading X-ray counterpart, the first identification of a GRB counterpart at any wavelength. Late time X-ray observations of GRB 970508, combined with optical and radio data allowed observers to map out the broadband afterglow spectrum, providing a remarkable corroboration of the predictions of the fireball model (Galama et al. (1998b), Section 1.2.5). Several X-ray afterglow observations have detected line emission, which is used to study the circum-burst medium. The list of discoveries is impressive, but there is reason to believe that future X-ray afterglow observations will yield an even greater bounty.

As part of this thesis, we undertook an ongoing program to study the X-ray afterglow of *HETE*-localized GRBs with the *Chandra X-ray Observatory* (hereafter *Chandra*). In this chapter, I will describe our scientific motivation and goals in this program, along with our strategy to achieve these goals. As part of this program, we observed *HETE*-localized GRB 011130 with *Chandra* at two separate epochs. The first epoch was a 30 ksec observation 10 days after the burst, and the second epoch was a 16 ksec observation 82 days after the burst. Of the 60+ X-ray point sources identified, none could be unambiguously identified as an X-ray counterpart.

6.1 Scientific motivation

A significant fraction ($\sim 1/2$) of GRBs are found to be "optically dark" (Section 1.5.2). This is likely because the optical light is extinguished by dust, or they occur at very high redshifts ($z > 5$) and their optical afterglow is absorbed by the LY-α forest (Section 1.5.3). However, medium energy ($E > 2keV$) X-ray observations are not susceptible to extinction by dust or the $Ly\alpha$ forest, so it is possible that all GRBs have potentially detectable X-ray afterglows. In fact, observations today are consistent with this. (Some observations have not detected an unambiguous afterglow, but it is likely that this is because they were too late or not deep enough to catch the rapidly fading afterglow.) So, follow-up observations with a sensitive X-ray instrument such as *Chandra* provide the only efficient means of detecting an afterglow counterpart (Ricker et al., 2001d; Monnelly et al., 2001; Butler et al., 2002; Fox, 2002a,b) for dark GRBs.

The ~arc-second localizations provided by *Chandra* can enable further studies with radio and optical telescopes. *Hubble* observations may be able to detect a very faint afterglow; or set a sensitive upper limit. In the Hubble Deep Field, the density of galaxies per square degree is 1.8×10^5 for $R \leq 25$ and 8×10^5 for $R \leq 28$. Within an arc-second radius *Chandra* error circle, we then expect 0.04 galaxies at $R \leq 25$ and 0.2 galaxies at $R \leq 28$, so if *Hubble* detects a galaxy at $R \leq 25$ then it is likely that it is the host galaxy of the GRB. Discovery of a host galaxy can be used to determine the GRB redshift.

Another important use of X-ray follow-up observations is the spectroscopic study of afterglow emission. X-ray line features are detected in six afterglows thus far (Section 1.3). The observed spectral lines are generally interpreted as redshifted iron of nickel (Section 1.3). Potentially, such measurements provide a powerful tool to study the properties of the medium surrounding the burst. Piro et al. (2000) interpret line emission seen from GRB 991216 by *Chandra* to imply, according to the supranova scenario (Vietri & Stella (1998); Section 1.4), that the GRB was preceded by a supernova that ejected $\sim 0.1 M_\odot$ of iron at a velocity of $\sim 0.1c$. Recent observations

of GRB 011211 by Reeves et al. (2002) detect X-ray lines that may come from elements other than iron (such as nickel or cobalt). However, each of the six X-ray line features detect thus far is of marginal significance, and most interpretations, such as the amount of iron in the ejecta, are model-dependent and are thus inconclusive. Further X-ray observations of GRB afterglows, within 1-2 days of the burst while the afterglow is still relatively bright, are needed to better understand the X-ray line emission and its relation to the circumburst medium and GRB progenitors.

6.2 *HETE* localization of GRB 011130

The *HETE* Wide-field X-ray Monitor (WXM) detected GRB 011130 as a 7σ GRB trigger on 30 November at 6:19:35 UT, with no gamma-ray emission detected by FREGATE. This event was a long, soft, X-ray rich burst, detected with a high significance in the WXM. The burst was well-localized by the WXM, but difficulties in determining spacecraft aspect resulted in three GCN Circulars being released, each with an improved localization. Because of its soft spectrum and lack of gamma-ray emission, GRB 011130 is classified as an X-ray Flash/X-ray Rich GRB (Section 1.5.1), and is alternatively referred to as XRF 011130. This class of GRBs is poorly understood due to lack of effective follow-up observation. *BeppoSAX* detected 39 X-ray Flashes in the Wide Field Camera (WFC) in its first 5 years of operation (Heise, 2002). By definition, these events weren't seen in the Gamma Ray Burst Monitor (GRBM) which provides triggers, so they were detected with large delays as untriggered events. Because they are unexplored at early times, providing a prompt localization of an XRF such as GRB 011130 has potential to be particularly valuable.

The burst occurred before dusk and only 2.5 hours before the full moon. The bright moon saturates the *HETE* boresight star cameras, which would otherwise be used to determine real-time spacecraft aspect. Instead, two ground-based methods were used to determine aspect 1-2 hours after the burst: one using the ACS cameras, and one using the on-board sun sensors and magnetometers. However, because the use of ACS cameras was not at the time routine, and the magnetometers had limited

calibration for the satellite roll angle at the time of the burst, initial estimates of the spacecraft roll were in error by $\sim 4°$. Because of this, two initial GCN Circulars (Ricker et al. (2001c), Ricker et al. (2001e)) were released 4 and 6 hours after the burst, with $\sim 4°$errors in their location.

Further review of the star camera data led to an accurate estimate of the spacecraft roll. With this new constraint in hand, both methods of determining aspect converged on the correct solution. The Crab Nebula was within the field of view of the WXM at the time of GRB011130, and calculation of the Crab's location from its WXM position yielded coordinates only 6 arcminutes from the Crab's known location, giving added confidence in the new aspect solution. A third GCN Circular (Ricker et al. (2001f)) was sent out about 10 hours after the burst with the new burst coordinates which differed by $\sim 4°$from those in the first two Notice.

6.3 Optical and radio observations of GRB 011130

A number of optical observations of the *HETE* error region of GRB 011130 were performed within the first few nights after the burst, but all observations were limited by the full moon near the burst location. No fading optical counterparts were found. The earliest observation, with the Calar Alto 1.23-m telescope, occurred 16.5 hrs after the burst trigger. These observations achieved a limiting magnitude of 18.5 - 19 in both bands R and I bands (Greiner et al., 2001).

The error region was observed by the VLA on December 3.73 UT, using five pointings at 4.86 GHz (Berger & Frail, 2001). In comparison to the NRAO VLA Sky Survey (NVSS), which was taken at 1.43 GHz (Condon et al., 1998), one source was found that was not in the NVSS catalog. A number of optical observations targeted this source. Early evidence that it faded (Garnavich et al. (2001a), Garnavich et al. (2001b)) prompted spectroscopic observations with the Magellan consortium's 6.5m Baade telescope at Las Campanas (hereafter *Magellan*) on December 7.15 UT (Jha et al. (2001)) that identified a galaxy at $z = 0.50$ at the location of the radio source. However, the source didn't show further fading, and later radio observations showed

a constant flux and flat spectrum, which likely identify the source as an AGN (Frail (2001)).

6.3.1 *Magellan* observations of GRB 011130

We targeted the *HETE* error box of GRB 011130 with the *Magellan* 6.5m Baade telescope on five nights between December 5 and 10, 2002. Observations are summarized in Table 6.3.1. The first two observations were significantly contaminated by full moon. The first observation covered the entire *HETE* error region with a mosaic of seven pointings; four subsequent observations targeted the Berger & Frail (2001) radio source (above), and thus only $\sim 1/5$ of the error region was covered. No fading sources were detected in comparison among the five epochs.

Table 6.1: Optical observations of the *HETE* error box of GRB 011130 with the *Magellan* 6.5m Baade telescope on five nights between December 5 and 10, 2002.

Day	Delay (days)	Instrument	Filter	Coverage	m_{limit}	seeing ($''$)	comment
12/04	3.97	LDSS-2	R	full mosaic	21.5	1	full moon
12/05	4.97	MagIC	R	radio source	22	0.7	full moon
12/06	5.89	MagIC	R	radio source	23.5	0.7	some moon
12/07	6.87	LDSS-2	R	radio source	23.5	0.7	no moon
12/10	9.80	LDSS-2	R	radio source	23.5	0.7	no moon

6.4 First epoch *Chandra* observations of GRB 011130

Because no optical counterpart was found in the first few days after the burst, we triggered our *Chandra* target of opportunity (TOO) program to observe optically dark GRBs. On 10 December, from 00:38 UT - 09:27 UT, beginning 9.77 days after the burst, the Chandra Observatory targeted the field of the X-ray rich gamma-ray burst GRB 011130. The observation duration was 30 ksec. The revised *HETE* error circle (Ricker et al. (2001f)) fit completely within the field-of-view of the ACIS-I array. Our observation proposal included a plan to establish accurate locations of the brightest X-ray sources in the *HETE* field and publish the result as a GCN Circular within one

day of receipt of the data. Special arrangements were made by the Chandra Science Center to expedite the pre-processing of the data from our observation.

6.4.1 X-ray point source detection

The data were processed using the *Chandra Interactive Analysis of Observations* (CIAO) software package[1] from the *Chandra* X-ray Center. We searched for point sources using the CIAO *Celldetect* and *Wavdetect* tools. The goal of the analysis was to completely and accurately detect all significant point sources, and to publish, via the *GRB Coordinates Network* (GCN), a list of sources, with accurate astrometry, within 24 hours of receipt of the data, so as to allow rapid broadband follow-up observations.

Celldetect uses the "sliding cell" method that has been successfully used with previous X-ray missions such as *Einstein* and *ROSAT*. The signal-to-noise (S/N) ratio of source counts to background counts is computed in each detect cell, and candidate sources are identified when the S/N exceeds a threshold. The detect cell is sized according to the point spread function (PSF), so it is considerably larger at the edge of the field of view. *Celldetect* effectively detects faint sources, except when the field is crowded or when there are extended sources. Our observation turned out not to have source crowding or extended sources, but to make sure our point source detections were robust, we also analyzed the data with the *Wavdetect* tool.

Wavdetect uses a wavelet correlation function with limited spatial extent and overall normalization zero. The wavelet has a quasi-Gaussian core surrounded by a negatively valued annulus, referred to as a "Mexican Hat" function. Point sources are most easily detected by a wavelet whose core size is similar to the PSF; the data are searched with a variety of spatial scales to account for the variable PSF. The advantages of *Wavdetect* are that it can detect extended sources and separate point sources in crowded fields. However, *Wavdetect* is computationally intensive, and even on a fast computer, it would have taken longer than the 10 hours. This

[1] http://asc.harvard.edu/ciao

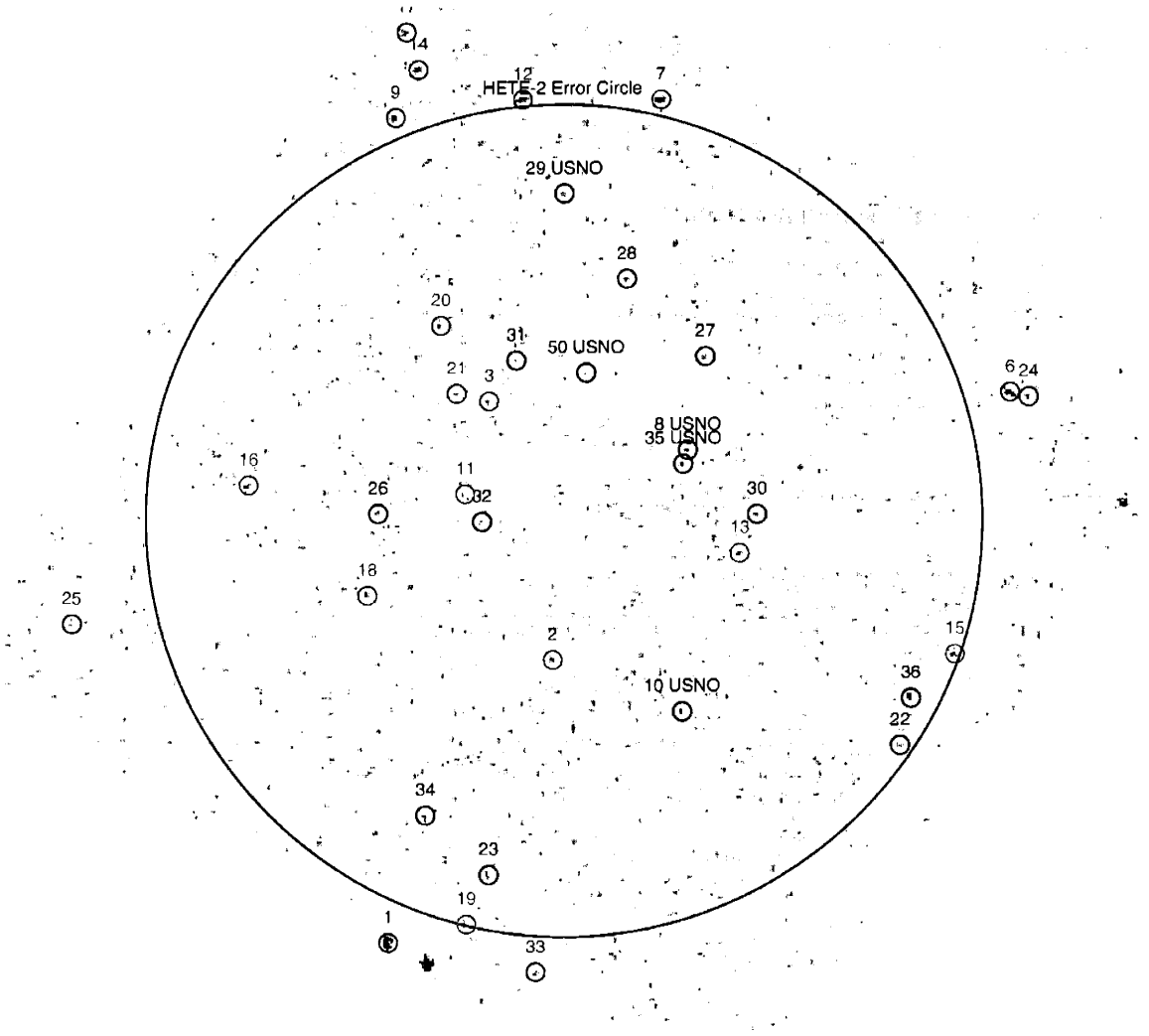

Figure 6-1: 30 ksec Chandra observation of *HETE* error circle (7.6 ′ radius, 90% confidence) of GRB011130. Sources are listed in Table 6.2. The green circles identify the ten brightest sources in the HETE error circle. The blue circles identify the next ten brightest sources in the HETE error circle. The black circles identify the USNO astrometric calibration stars. The red circles identify significant sources found outside the HETE error circle.

was problematic because we wanted to publish our results in a GCN Circular with minimal delay. We solved this problem by running *Wavdetect* in parallel on multiple computers, which sped up processing to an acceptable rate.

Wavdetect and *Celldetect* were each run with a S/N the threshold of 2. This is a low threshold that could possibly lead to false source detections, but we wanted to make sure we did not miss any real sources even if they were only marginally detected. Further, marginally significant sources detected in the *Chandra* data could be compared to optical images, and if a decaying optical source were seen at the location, the afterglow counterpart could be identified. *Wavdetect* and *Celldetect* identified an almost identical set of sources, and measured very similar significance and source counts for each source.

6.4.2 Astrometric calibration with USNO stars

We refined the *Chandra* aspect solution by correlating against the known position of three USNO stars detected in the *Chandra* observation (a few X-ray bright USNO stars are typically detected in a *Chandra* exposure of this duration). We determined the overall shift and rotation of the *Chandra* aspect solution needed for consistency with the optical USNO star positions, which are known to within 0.25 $''$. Uncertainty in our positions were established by summing the following in quadrature: the error reported by *Celldetect*, the error in determining the proper shift and rotation, and the error estimate from the USNO catalog.

6.4.3 First epoch detected sources

On December 11.33 UT, within a day of completion of the *Chandra* observations, and less than 10 hours after receiving the data from the Chandra X-ray center, we published a GCN Circular (Ricker et al. (2001d)) listing the position and source counts from the ten brightest sources within the 7.6$'$ radius *HETE* error circle. One day later, on December 12.27 UT, we published a second GCN Circular (Monnelly et al. (2001)) in which we completed the list of detected sources by presenting all sources

found in the entire ACIS-I detector field-of-view down to a limit of 10 detected counts. Listed separately, we included all the sources that were outside the *HETE* error circle, and we provided a link to a web page[2] listing additional sources down to the detection limit of the observation. A full image of the field is shown in Figure 6-1, and the full list of detected sources, down to a limit of 3 detected counts, is shown in Table 6.2.

To estimate the limiting sensitivity of these observations we calculate the $2-10keV$ flux corresponding to 5 counts in the 30 ksec observation. The SNR of a 5 count detection depends on the background count rate within the detection cell, whose size varies over the field of view with the changing mirror PSF. Typically, 5 counts corresponds to $\sim 3\sigma$. We actually extend our search even lower to 3 counts ($\sim 2\sigma$), but this level of significance is below a reasonable definition of limiting sensitivity, so we use 5 counts. We use $N_H = 1.1 \times 10^{21} cm^{-2}$ as the galactic H I column density in the direction of the burst from the survey of Dickey & Lockman (1990). We assume the GRB X-ray afterglow at this time has the expected spectral index of $\beta \simeq 1.2$ (Section 1.2). The unabsorbed $2 - 10keV$ limiting flux corresponding to 5 counts is $F_X = 2.1 \times 10^{-15}$ergs cm$^{-2}s^{-1}$.

6.4.4 Optical observations of X-ray sources

With only a single epoch of X-ray observations, it is difficult to identify an afterglow counterpart unless it is either remarkably bright, or can be seen to fade during the observation. Neither of these are likely to be the case for our observation, which occurred 10 days after the burst. However, comparing the X-ray source positions to previous and subsequent optical and radio observations provides a useful method for identifying the counterpart. A number of observers performed such a search (Mirabal & Halpern (2001a), Mirabal & Halpern (2001b)), and several potential counterparts were identified (Frail (2001)), but none were seen to exhibit a fading behavior (Halpern et al. (2001)).

[2]http://space.mit.edu/HETE/Bursts/GRB011130

Table 6.2: Epoch 1 *Chandra* sources indexed by counts detected with *Wavdetect*. The green circles identify the ten brightest sources in the *HETE* error region. The blue circles identify the next ten brightest sources in the *HETE* error region. The black circles identify the astrometric calibration stars. The red circles identify significant sources found outside the *HETE* error region.

Num	Chandra Name	RA	DEC	ΔRA(s)	ΔDEC(″)	Cts	SNR	R(′)
		Sources within *HETE* error circle						
2	CXOU J030527.9+034657	3:5:27.70	3:46:56.46	0.057	1.18	128	56.6	2.6
3	CXOU J030532.5+035140	3:5:32.32	3:51:39.79	0.057	1.18	105	49.6	2.5
11	CXOU J030534.3+034958	3:5:34.08	3:49:58.35	0.057	1.18	37	18.8	1.8
13	CXOU J030514.2+034854	3:5:14.03	3:48:53.56	0.057	1.19	32	15.4	3.3
15	CXOU J030458.7+034702	3:4:58.46	3:47:02.31	0.067	1.28	31	8.0	7.5
16	CXOU J030550.1+035009	3:5:49.88	3:50:08.80	0.058	1.20	28	11.5	5.8
18	CXOU J030541.4+034808	3:5:41.25	3:48:07.26	0.057	1.19	23	11.5	3.8
19	CXOU J030534.2+034208	3:5:34.07	3:42:08.24	0.062	1.33	22	7.0	7.6
20	CXOU J030536.0+035303	3:5:35.83	3:53:02.99	0.058	1.19	20	9.7	4.2
21	CXOU J030534.7+035147	3:5:34.68	3:51:47.96	0.057	1.19	18	8.8	3.0
22	CXOU J030502.4+034522	3:5:02.44	3:45:22.41	0.071	1.30	18	5.8	7.4
23	CXOU J030532.4+034301	3:5:32.44	3:43:01.87	0.062	1.29	17	6.0	6.6
26	CXOU J030540.5+034936	3:5:40.45	3:49:36.96	0.057	1.19	15	7.8	3.4
27	CXOU J030516.5+035229	3:5:16.48	3:52:29.34	0.059	1.19	14	7.3	4.0
28	CXOU J030522.2+035354	3:5:22.21	3:53:54.43	0.059	1.19	14	7.1	4.6
30	CXOU J030512.9+034936	3:5:12.75	3:49:36.22	0.057	1.19	12	6.5	3.5
31	CXOU J030530.3+035224	3:5:30.31	3:52:24.48	0.057	1.18	11	6.0	3.0
32	CXOU J030532.9+034927	3:5:32.86	3:49:27.94	0.057	1.19	11	6.0	1.5
34	CXOU J030537.0+034406	3:5:37.04	3:44:06.95	0.059	1.25	10	4.6	6.0
36	CXOU J030501.6+034613	3:5:01.65	3:46:13.94	0.061	1.24	10	3.9	7.1
37	CXOU J030535.7+034639	3:5:35.68	3:46:39.88	0.057	1.19	9	5.0	3.6
38	CXOU J030552.0+034714	3:5:52.03	3:47:14.30	0.060	1.29	8	3.7	6.7

Continued on next page

Num	Chandra Name	RA	DEC	ΔRA(s)	ΔDEC(″)	Cts	SNR	R(′)
			Continued from previous page					
40	CXOU J030509.5+035217	3:5:09.50	3:52:17.74	0.060	1.19	8	4.0	5.2
41	CXOU J030515.1+034457	3:5:15.12	3:44:57.02	0.058	1.23	8	3.6	5.4
42	CXOU J030509.4+035027	3:5:09.42	3:50:27.17	0.058	1.20	7	3.8	4.5
43	CXOU J030544.9+034338	3:5:44.89	3:43:38.95	0.062	1.27	7	3.0	7.4
44	CXOU J030527.8+035548	3:5:27.81	3:55:48.09	0.058	1.20	7	3.5	6.3
45	CXOU J030532.7+035624	3:5:32.71	3:56:24.25	0.060	1.21	7	3.4	7.0
46	CXOU J030521.7+034628	3:5:21.72	3:46:28.81	0.058	1.20	6	3.4	3.3
47	CXOU J030534.5+035442	3:5:34.48	3:54:42.42	0.060	1.20	6	3.2	5.5
48	CXOU J030527.1+035632	3:5:27.10	3:56:32.92	0.060	1.28	6	2.7	7.0
49	CXOU J030525.1+034910	3:5:25.10	3:49:10.84	0.058	1.18	5	3.1	0.6
51	CXOU J030517.4+034829	3:5:17.43	3:48:29.35	0.058	1.19	5	3.0	2.6
52	CXOU J030546.4+035240	3:5:46.39	3:52:40.75	0.063	1.24	5	2.6	5.8
53	CXOU J030538.0+034817	3:5:37.95	3:48:17.14	0.058	1.19	4	2.5	3.0
54	CXOU J030517.7+034927	3:5:17.71	3:49:27.30	0.057	1.19	4	2.5	2.3
55	CXOU J030532.0+035313	3:5:31.99	3:53:13.04	0.057	1.19	4	2.5	3.9
56	CXOU J030535.1+035350	3:5:35.06	3:53:50.53	0.058	1.19	4	2.5	4.8
57	CXOU J030518.5+035433	3:5:18.54	3:54:33.92	0.059	1.19	4	2.4	5.5
58	CXOU J030522.6+034935	3:5:22.56	3:49:35.15	0.057	1.19	3	2.1	1.1
59	CXOU J030519.7+034641	3:5:19.74	3:46:41.85	0.058	1.19	3	2.0	3.3
60	CXOU J030515.9+035037	3:5:15.92	3:50:37.27	0.058	1.18	3	2.0	3.0
61	CXOU J030533.7+035007	3:5:33.67	3:50:07.75	0.057	1.19	3	2.0	1.8
			Sources outside *HETE* error circle					
1	CXOU J030539.8+034148	3:5:39.79	3:41:48.82	0.060	1.23	132	26.0	8.3
6	CXOU J030454.4+035149	3:4:54.39	3:51:49.41	0.066	1.25	52	11.7	8.4
7	CXOU J030519.7+035711	3:5:19.67	3:57:11.99	0.062	1.21	50	14.8	7.9
9	CXOU J030539.1+035652	3:5:39.09	3:56:52.21	0.063	1.21	42	12.4	8.0
12	CXOU J030529.8+035711	3:5:29.79	3:57:11.93	0.063	1.21	36	12.3	7.7
14	CXOU J030537.4+035744	3:5:37.41	3:57:44.79	0.065	1.22	32	8.5	8.6
17	CXOU J030538.3+035825	3:5:38.28	3:58:25.95	0.067	1.26	24	7.4	9.4

Continued on next page

Num	Chandra Name	RA	DEC	ΔRA(s)	ΔDEC(″)	Cts	SNR	R(′)
			Continued from previous page					
24	CXOU J030453.0+035144	3:4:53.04	3:51:44.28	0.070	1.25	16	5.3	8.7
25	CXOU J030602.8+034737	3:6:02.77	3:47:37.64	0.074	1.39	16	4.8	9.1
33	CXOU J030529.0+034115	3:5:29.02	3:41:15.90	0.065	1.38	11	4.0	8.3
			USNO Aspect Stars					
8	USNO-a2 0900-00717077	3:5:17.79	3:50:46.95	0.057	1.18	44	22.0	2.6
10	USNO-a2 0900-00717107	3:5:18.26	3:46:00.36	0.058	1.19	41	17.1	4.1
29	USNO-a2 0900-00717661	3:5:26.77	3:55:28.89	0.062	1.20	14	6.0	6.0
35	USNO-a2 0900-00717105	3:5:18.13	3:50:31.81	0.058	1.18	10	5.4	2.4
50	USNO-a2 0900-00717551	3:5:25.20	3:52:11.41	0.057	1.19	5	3.0	2.7

6.5 Second epoch *Chandra* observations of GRB 011130

On 20 February, from 10:02 UT - 14:30 UT, beginning 82.15 days after the burst, *Chandra* targeted the field of GRB 011130 for a second epoch observation. This was a 16 ksec observation with ACIS-I, following up the 30 ksec first epoch observation. The goal of this observation was to identify any sources whose X-ray flux decayed significantly between the two epochs. The two epochs had different exposures (30 ksec versus. 16 ksec) and slightly different pointing, so in comparing the epochs, we correct for exposure, effective area, and point-spread-function (PSF) of the *Chandra* mirrors.

6.5.1 Comparison with first epoch

Whereas the analysis of the first epoch data focused on identifying point sources and calibrating astrometry, analysis of second epoch data focused on checking for decay behavior in any of the epoch 1 sources. The catalog of sources, and their positions, are determined from the epoch 1 *Wavdetect* results (Table 6.2). For each source i, we measure in each epoch the background-subtracted count rates C_{1i}, C_{2i} within an extraction region defined by the 95% encircled energy radius of each position. We use

a parameterized fit of the 95% encircled energy radius

$$R_{95\%EE}(\theta) = 2.05 - 0.55\theta + 0.18\theta^2$$

where $R_{95\%EE}$ is in arc-seconds and θ is in arc-minutes (Feigelson et al., 2000). An overall background rate (counts/arcsec^2) is calculated for each epoch, then multiplied by the area $\pi R^2_{95\%EE}$ to give background counts in each extraction region, B_{1i} and B_{2i}. Finally, we predict $E(C_{2i})$, the expected epoch 2 count rate if the sources are constant from epoch 1,

$$E(C_{2i}) = C_{1i}\frac{T_2 A_{2i}}{T_1 A_{1i}}$$

where T is the exposure and A is the effective area.

To search for afterglow candidates, we compare C_{2i} to $E(C_{2i})$ and search for sources that have faded by a fraction consistent with afterglow decay, or below detection threshold in epoch 2. According to GRB afterglow theory and observations, the X-ray flux should exhibit a power-law decay $F(t) \propto t^{-\alpha}$ where $\alpha \simeq 1.3$ before the jet break time (Section 1.2.6) and $\alpha \simeq 2.4$ after. Frail et al. (2001) measured jet-break times of typically 1-25 days in a sample of 17 GRBs, with GRB 990712 > 47.7 days. Given the time of each epoch since the GRB, $T_1 = 9.77d$ and $T_2 = 82.15d$, and assuming $1.3 \leq \alpha \leq 2.4$, the corresponding limits on the expected source flux ratio are $0.06 \leq F_2/F_1 \leq 0.006$. This ratio is compared directly to the ratio $E(C_{2i})/C_{1i}$. All but the brightest few sources with $E(C_{2i}) \geq 15cts$ are expected to fade to < 1 count if they are a GRB afterglow.

6.5.2 Results

Of the 20 brightest sources reported in the first epoch (Monnelly et al. (2001)), none were observed to fade in a manner that is consistent with the power-law behavior that is characteristic of gamma-ray burst afterglows (Section 6.5.1). Corrected for exposure, the largest fade for any of the sources in the list was by a factor of 3. We note that our brightest epoch 1 source (CXOU J030527.9+034657), which appears to

be associated with a 20th magnitude galaxy (Mirabal & Halpern (2001b)), faded by a factor of of approximately 2, which is quite reasonable if the source is an AGN.

For sources less brighter than the top 20, $E(C_{2i})$ becomes small enough that there is a significant probability that an intrinsically constant source will appear to fade away due to chance fluctuations, and this probability increases as fainter sources are included in the search. To quantify the probability of a false detection, we adopted a reasonable criterion for an afterglow candidate as a source whose background counts C fade to below the level of a 1σ background fluctuation, $\sqrt{B_{2i}}$. Then we search successively fainter sources in our catalog calculating the probability that each source would be a false detection, and the cumulative probability that at least one of the sources brighter than the current source is a false detection.

For a given source with expected counts λ, and no background, the probability of detecting x counts simply comes from the Poisson distribution, $p(x, \lambda) = e^{-\lambda}\lambda^x/x!$. To add in the effect of background B, consider that C is background subtracted counts, so we need to substitute $\lambda = E(C) + B$ and $x = C + B$ giving:

$$p(C, E(C)) = \frac{e^{-(E(C)+B)}(E(C)+B)^C}{C!}.$$

The false detection probability, defined as the probability that $C < \sqrt{B}$, is then

$$P_i(C < \sqrt{B}, E(C) = \sum_{x=0}^{x<(B+\sqrt{B})} \frac{e^{-(E(C)+B)}(E(C)+B)^x}{x!}.$$

Now, if this is the false detection probability, $1 - P_i$ is the probability of no false detection, and if N sources are examined, then

$$\prod_{i=1}^{N}(1 - P_i)$$

is the probability that none are false detections. As we examine fainter sources in the catalog, we keep a running tally of the probability that we have falsely detected a fading source.

Table 6.3: Comparison of *Chandra* sources between first and second observations. Here C_1 denotes the epoch 1 background subracted (net) counts for the source, B_1 the epoch 1 background counts estimate, $E(C_2)$ the expected epoch 2 counts based on epoch 1, C_2 the observed net counts in epoch 2, and B_2 the epoch 2 background counts estimate.

Num	Chandra Name	RA	DEC	C_1	B_1	$E(C_2)$	C_2	B_2
2	CXOU J030527.9+034657	3:5:27.70	3:46:56.46	128.9	1.1	63.8	29.5	0.5
3	CXOU J030532.5+035140	3:5:32.32	3:51:39.79	106.9	1.1	50.9	46.1	0.9
11	CXOU J030534.3+034958	3:5:34.08	3:49:58.35	37.0	1.0	17.6	33.4	0.6
13	CXOU J030514.2+034854	3:5:14.03	3:48:53.56	34.8	1.2	16.5	13.5	0.5
15	CXOU J030458.7+034702	3:4:58.46	3:47:02.31	36.9	7.1	17.7	10.8	2.2
16	CXOU J030550.1+035009	3:5:49.88	3:50:08.80	31.6	3.4	15.1	15.3	2.7
18	CXOU J030541.4+034808	3:5:41.25	3:48:07.26	32.5	1.5	15.4	21.1	0.9
19	CXOU J030534.2+034208	3:5:34.07	3:42:08.24	21.6	7.4	10.3	10.9	2.1
20	CXOU J030536.0+035303	3:5:35.83	3:53:02.99	19.3	1.7	8.8	14.2	1.8
21	CXOU J030534.7+035147	3:5:34.68	3:51:47.96	17.9	1.1	8.5	10.9	1.1
22	CXOU J030502.4+034522	3:5:02.44	3:45:22.41	16.2	6.8	14.2	24.2	1.8
23	CXOU J030532.4+034301	3:5:32.44	3:43:01.87	20.0	5.0	9.6	8.6	1.4
26	CXOU J030540.5+034936	3:5:40.45	3:49:36.96	18.7	1.3	8.5	4.1	0.9
27	CXOU J030516.5+035229	3:5:16.48	3:52:29.34	14.5	1.5	7.3	2.8	1.2
28	CXOU J030522.2+035354	3:5:22.21	3:53:54.43	17.0	2.0	8.1	3.1	1.9
30	CXOU J030512.9+034936	3:5:12.75	3:49:36.22	21.6	1.4	10.5	14.4	0.6
31	CXOU J030530.3+035224	3:5:30.31	3:52:24.48	12.8	1.2	6.1	6.9	1.1
32	CXOU J030532.9+034927	3:5:32.86	3:49:27.94	11.1	0.9	5.5	6.5	0.5
34	CXOU J030537.0+034406	3:5:37.04	3:44:06.95	16.3	3.7	8.1	8.8	1.2
36	CXOU J030501.6+034613	3:5:01.65	3:46:13.94	14.1	5.9	7.0	9.3	1.7
37	CXOU J030535.7+034639	3:5:35.68	3:46:39.88	14.6	1.4	7.3	17.4	0.6
38	CXOU J030552.0+034714	3:5:52.03	3:47:14.30	8.9	5.1	4.2	4.1	2.9
40	CXOU J030509.5+035217	3:5:09.50	3:52:17.74	10.5	2.5	4.9	2.4	1.6

Continued on next page

Num	Chandra Name	RA	DEC	C_1	B_1	$E(C_2)$	C_2	B_2
			Continued from previous page					
41	CXOU J030515.1+034457	3:5:15.12	3:44:57.02	8.1	2.9	4.0	-0.7	0.7
42	CXOU J030509.4+035027	3:5:09.42	3:50:27.17	14.1	1.9	6.9	3.1	0.9
43	CXOU J030544.9+034338	3:5:44.89	3:43:38.95	17.1	6.9	8.1	13.4	2.6
44	CXOU J030527.8+035548	3:5:27.81	3:55:48.09	13.8	4.2	6.5	-1.3	4.3
45	CXOU J030532.7+035624	3:5:32.71	3:56:24.25	13.0	6.0	5.9	4.9	6.1
46	CXOU J030521.7+034628	3:5:21.72	3:46:28.81	7.8	1.2	3.9	3.5	0.5
47	CXOU J030534.5+035442	3:5:34.48	3:54:42.42	7.0	3.0	3.2	4.8	3.2
48	CXOU J030527.1+035632	3:5:27.10	3:56:32.92	15.1	5.9	6.4	9.1	5.9
49	CXOU J030525.1+034910	3:5:25.10	3:49:10.84	5.0	1.0	5.9	5.5	0.5
51	CXOU J030517.4+034829	3:5:17.43	3:48:29.35	9.0	1.0	4.5	2.5	0.5
52	CXOU J030546.4+035240	3:5:46.39	3:52:40.75	10.5	3.5	6.1	9.7	3.3
53	CXOU J030538.0+034817	3:5:37.95	3:48:17.14	6.9	1.1	3.2	3.3	0.7
54	CXOU J030517.7+034927	3:5:17.71	3:49:27.30	5.1	0.9	2.4	2.5	0.5
55	CXOU J030532.0+035313	3:5:31.99	3:53:13.04	7.5	1.5	3.5	7.4	1.6
56	CXOU J030535.1+035350	3:5:35.06	3:53:50.53	17.8	2.2	8.6	6.6	2.4
57	CXOU J030518.5+035433	3:5:18.54	3:54:33.92	10.1	2.9	4.6	1.3	2.7
58	CXOU J030522.6+034935	3:5:22.56	3:49:35.15	4.0	1.0	1.7	2.5	0.5
59	CXOU J030519.7+034641	3:5:19.74	3:46:41.85	3.8	1.2	1.9	-0.5	0.5
60	CXOU J030515.9+035037	3:5:15.92	3:50:37.27	3.8	1.2	1.8	0.4	0.6
61	CXOU J030533.7+035007	3:5:33.67	3:50:07.75	4.1	0.9	1.9	1.4	0.6

We note that 1st epoch sources sources 41 and 44 (Table 6.2) faded to levels consistent with the background. Source 41 had $C_2 = -0.7$ counts (negative because of background subtraction) with $E(C_2) = 4.0$. Source 44 had $C_2 = -1.3$ counts with $E(C_2) = 6.5$. These sources were the 24^{st} and 27^{th} brightest sources, excluding USNO stars and sources outside the *HETE* error circle. We estimate a 50% probability for chance fading to the background in one or more of our 24 brightest sources; we estimate a 75% probability for chance fading to the background in one or more of our 27 brightest sources.

6.6 Conclusions: upper limits

Optical follow-up observations of GRB 011130 were limited on the first two nights following the burst by full moon presence. After that, most observations focused on the radio transient of Berger & Frail (2001), which was later found to be a nearly constant source. In a case such as this with no optical detection, it is interesting to ask whether this is due to lack of optical observations that were quick enough and deep enough, or because the source is intrinsically dark (Section 1.5.2). Typically, detectable optical transients 18 hours after the burst have a magnitude of $R \sim 20-24$ (Reichart & Yost, 2002). This level of sensitivity was not reached until more than four days after the burst (Table 6.3.1), leaving open the possibility that the optical transient was not detected because observations were not early enough and deep enough.

With no optical transient found, we observed the error region with first epoch *Chandra* observations for 30 ksec 9.77 days after the burst, in hopes of detecting an X-ray transient. Of 61 point sources detected in this observation, down to a limiting sensitivity of $F_X(2-10keV) = 2.1 \times 10^{-15}$ ergs cm^{-2}s^{-1}, none was found to correspond to a fading radio or optical source. We re-observed the field with second epoch *Chandra* observations for 16 ksec 82.15 days after the burst to search for fading behavior in the epoch 1 sources. For expected afterglow behavior, we expected all but the brightest few epoch 1 sources to fade below detection threshold in the second epoch, so we searched the epoch 1 positions in the epoch 2 data for sources that appeared to have faded away. We found two sources that faded to a level consistent with the background, but the significance of the fading was very marginal. We estimate a $> 50\%$ probability the detection of fading behavior was spurious, so without detection of a radio or optical counterpart at the location of one of our sources, we cannot identify either as the counterpart to the GRB.

Chapter 7

Conclusions

Since its successful launch in October of 2000, the *HETE* program has demonstrated that a nearly autonomous, low cost, small satellite can be built in a University setting and operated by a small team of scientists (the operations team consisted of 6–8 people for pre-launch and post-launch operations.) As of May 2002, *HETE* has localized 18 GRBs, leading to 4 optical counterparts (GRB 010921, GRB 020124, GRB 020305, and GRB 020331) and 1 radio counterpart (GRB 020127). Three localizations have led to *Chandra* observations (GRB 011130, GRB 020127, and GRB 020531), 8 have been classified as X-ray Rich GRBs (GRB 010213, GRB 010225, GRB 010326B, GRB 010629, GRB 011019, GRB 011130, GRB 011212, GRB 020317), and the localization of short/hard burst GRB 020531 marked the first time that a short/hard localization has led to deep, early, broad-band follow-up observations.

The *HETE* Burst Alert Network, consisting of 14 low cost ground stations has achieved nearly continuous coverage enabling *HETE* to report GRB detections on a near real-time basis. The WXM in-flight analysis has correctly localized 6 GRBs in near real-time, although technical "glitches" prevented immediate distribution to the astronomical community (distribution was typically delayed by a few hours or less). However, there is also every reason to believe that *HETE* will soon produce its first near real-time localization.

Much has been learned about GRBs in the past decade, but many questions remain, including the nature of the central engine, the connection between GRBs

and Type Ib/Ic supernovae, the properties of short/hard GRBs, the nature of X-ray rich GRBs, and the existence of high-redshift GRBs. *HETE*'s FREGATE, WXM and SXC instruments will address these questions using the currently unique combination of broad energy coverage and the ability to promptly provide precise localizations that are rapidly disseminated to the observer community. We have learned through experience that each new localized GRB may have unique properties that provide new insights. We expect *HETE* operations to last until 2004, and during that time produce a total of $\sim$ 60 GRB localizations. These localizations will continue to trigger broad-band follow-up observations in radio, optical, and X-ray wavelengths by the *HETE* science team and the observer community. These efforts are expected to generate $\sim$ 25 optical afterglows, $\gtrsim$ 25 redshifts, and a wealth of new knowledge about GRBs.

The design and performance of the SXC was described in Chapter 3, followed by a description of its imaging properties and sensitivity in Chapter 4. The SXC cocsists of two orthogonally-oriented, one-dimensional coded-aperture units. The SXC pairs the precise position resolution of X-ray CCDs with an electroformed coded aperture mask to achieve sub-arcminute localizations over a wide field of view of over 60°. SXC is currently localizing sources with a 20″ RMS accuracy, corresponding to a two dimensional 90 percent confidence error radius of 43″. This combination of wide field of view and precise angular resolution is unprecedented among previous X-ray coded aperture systems flown in space missions.

The SXC's outer optical blocking filters were lost after launch, but the inner Beryllium optical blocking filters remain intact, shielding one of the two CCDs in each SXC module from optical light contamination. Despite the loss of half of the CCD collecting area, and the inability to operate within 4–5 days of the full moon, the SXC has demonstrated its ability to reliably detect and localize transient X-ray sources with detections of numerous Galactic X-ray transients. As of May 2002, the SXC has not yet localized a GRB, but recent adjustments of CCD readout have provided a 50% sensitivity increase. For the majority of WXM-localized GRBs, excluding bursts that occur outside the SXC FOV or at times when the SXC is turned off due to full

moon, we expect the SXC with its increased sensitivity to provide at least a one sided localization.

GRB 0111212 (Chapter 5) was detected by FREGATE and localized by WXM with a 10 hour delay. Though slower than typical *HETE* performance, this localization was sufficiently prompt to enable several deep optical observations covering the error region, reaching a limiting magnitude of $R = 22.7$ one day after the burst and $R = 24.5$ two days after the burst. We performed deep follow-up observations at later epochs, detecting several candidates, but none were compelling because they were all close to the limiting magnitude of the observation. With early, deep optical observations and no detected transient, GRB 011212 can be classified as an "optically dark" GRB, providing evidence that the progenitor is surrounded by a dense circumburst medium that is extinguishing the optical afterglow.

GRB 020331 (Chapter 5), was detected by FREGATE and localized by WXM with a 40 minute delay. A fading optical counterpart was detected two days later by Fox et al. (2002). The counterpart was subsequently identified in optical observations by Kato et al. (2002) taken just 47 minutes after the burst, one of the earliest optical counterpart detections to date. Combining our three epochs of *Magellan* observations with other published data, we find that the R-band lightcurve between 47 minutes and 12.35 days after the burst is consistent with a power-law decay $\alpha = 1.00$ plus a constant component at $R = 23.6$, which we attribute to the GRB host galaxy. In our second and third epoch observations (8.4 and 12.5 days after the GRB), the optical transient is dimmer than the galaxy and is offset by $0.8'' \pm 0.1''$ to the east.

GRB 011130 was detected and localized by WXM with no emission detected by FREGATE, making it an X-ray Rich GRB. Optical observations, hampered during the first few days by a full moon, did not detect an optical transient. We observed the error region with first epoch *Chandra* observations for 30 ksec at 9.77 days after the burst, in hopes of detecting an X-ray transient as part of our program to provide precise X-ray positions of optically dark GRBs. None of the 61 point sources detected in this observation, down to a limiting sensitivity of $F_X(2 - 10keV) = 2.1 \times 10^{-15}$ ergs cm^{-2}s^{-1}, corresponded to a fading radio or optical source. In an

effort to search for fading X-ray sources among our epoch 1 sources, we re-observed the field with second epoch *Chandra* observations for 16 ksec at 82.15 days after the burst. We found two sources that faded to a level consistent with the background, but the significance of the fading was very marginal and without corroboration from radio or optical observations, we cannot confidently identify either source as a counterpart to the GRB.

This paragraph is included as an addendum after final revisions of this thesis were completed. In August of 2002, the SXC provided its first two GRB localizations. On August 13, GRB 020813 was detected by FREGATE, WXM, and SXC as a long, bright burst. The WXM flight localization was reported 4 minutes and 14 seconds after the burst, and the SXC localization from ground-based analysis was reported 184 minutes after the burst. Follow-up efforts led to optical and X-ray counterparts, and a redshift of $z = 1.254$. Six days later, GRB 020819 was also detected by FREGATE, WXM, and SXC as moderately bright, long GRB. The WXM and SXC reported localizations with delays of 98 and 176 minutes, respectively. Follow-up observations have not yet detected a counterpart.

Bibliography

Abel, T., Bryan, G. L., & Norman, M. L. (2002). The Formation of the First Star in the Universe. *Science*, **295**, 93–98.

Andersen, M. I., Hjorth, J., Pedersen, H., Jensen, B. L., Hunt, L. K., Gorosabel, J., Møller, P., Fynbo, J., Kippen, R. M., Thomsen, B., Olsen, L. F., Christensen, L., Vestergaard, M., Masetti, N., Palazzi, E., Hurley, K., Cline, T., Kaper, L., & Jaunsen, A. O. (2000). VLT identification of the optical afterglow of the gamma-ray burst GRB 000131 at z=4.50. *Astronomy and Astrophysics*, **364**, L54–L61.

Antonelli, L. A., Piro, L., Vietri, M., Costa, E., Soffitta, P., Feroci, M., Amati, L., Frontera, F., Pian, E., Zand, J. J. M. i., Heise, J., Kuulkers, E., Nicastro, L., Butler, R. C., Stella, L., & Perola, G. C. (2000). Discovery of a Redshifted Iron K Line in the X-Ray Afterglow of GRB 000214. *The Astrophysical Journal*, **545**, L39–L42.

Atteia, J.-L., Boer, M., Cotin, F., Couteret, J., Dezalay, J.-P., Ehanno, M., Evrard, J., Lagrange, D., Niel, M., Olive, J.-F., Rouaix, G., Souleille, P., Vedrenne, G., Hurley, K., Ricker, G., Vanderspek, R., Crew, G., Doty, J., & Butler, N. (2002). In flight performance and first results of FREGATE. In *AIP Conf. Proc.: Woods Hole Conference on Gamma-Ray Burst and Afterglow Astronomy 2001, in press*, pages 4+.

Band, D., Matteson, J., Ford, L., Schaefer, B., Palmer, D., Teegarden, B., Cline, T., Briggs, M., Paciesas, W., Pendleton, G., Fishman, G., Kouveliotou, C., Meegan,

C., Wilson, R., & Lestrade, P. (1993). BATSE observations of gamma-ray burst spectra. I - Spectral diversity. *The Astrophysical Journal*, **413**, 281–292.

Band, D. L., Hartmann, D. H., & Schaefer, B. E. (1999). A Statistical Treatment of the Gamma-Ray Burst "No Host Galaxy" Problem.II. Energies of Standard Candle Bursts. *The Astrophysical Journal*, **514**, 862–868.

Barraud, C., Olive, J.-F., Lestrade, J., Atteia, J.-L., Hurley, K., Ricker, G., Lamb, D. Q., Kawai, N., Boer, M., Dezalay, J.-P., Pizzichini, G., Vanderspek, R., Crew, G., Doty, J., Monnelly, G., Villasenor, J., Butler, N., Levine, A., Yoshida, A., Shirasaki, Y., Sakamoto, T., Tamagawa, T., Torii, K., Matsuoka, M., Fenimore, E. E., Galassi, M., Tavenner, T., Donaghy, T. Q., Graziani, C., & Jernigan, J. (2002). Spectral analysis of 24 GRBs/XRFs observed with HETE-2/FREGATE. *Astronomy and Astrophysics, submitted (astro-ph/0206380)*.

Berger, E. & Frail, D. A. (2001). GRB011130, radio observations. *GRB Circular Network*, **1173**, 1+.

Blandford, R. D. & McKee, C. F. (1976). Fluid dynamics of relativistic blast waves. *Physics of Fluids*, **19**, 1130–1138.

Bloom, J. S. & Kulkarni, S. R. (2001). The Observed Offset Distribution of GRBs about Their Hosts. In *Gamma-ray Bursts in the Afterglow Era*, pages 209+.

Bloom, J. S., Kulkarni, S. R., Djorgovski, S. G., Eichelberger, A. C., Cote, P., Blakeslee, J. P., Odewahn, S. C., Harrison, F. A., Frail, D. A., Filippenko, A. V., Leonard, D. C., Riess, A. G., Spinrad, H., Stern, D., Bunker, A., Dey, A., Grossan, B., Perlmutter, S., Knop, R. A., Hook, I. M., & Feroci, M. (1999). The unusual afterglow of the gamma-ray burst of 26 March 1998 as evidence for a supernova connection. *Nature*, **401**, 453–456.

Bloom, J. S., Frail, D. A., & Sari, R. (2001a). The Prompt Energy Release of Gamma-Ray Bursts using a Cosmological k-Correction. *The Astronomical Journal*, **121**, 2879–2888.

Bloom, J. S., Djorgovski, S. G., & Kulkarni, S. R. (2001b). The Redshift and the Ordinary Host Galaxy of GRB 970228. *The Astrophysical Journal*, **554**, 678–683.

Boer, M., Greiner, J., Kahabka, P., Motch, C., & Voges, W. (1993). Gamma-ray burst quiescent counterparts in the ROSAT all-sky survey data. *Astronomy and Astrophysics Supplement*, **97**, 69+.

Borozdin, K. & Trudolyubov, S. (2002). Observations of the x-ray afterglows of grb 011211 and grb 001025 by xmm-newton. astro-ph/0205208.

Brainerd, J. J. (1992). Gamma-ray bursts in the Galactic halo. *Nature*, **355**, 522–524.

Briggs, M. S., Paciesas, W. S., Pendleton, G. N., Meegan, C. A., Fishman, G. J., Horack, J. M., Brock, M. N., Kouveliotou, C., Hartmann, D. H., & Hakkila, J. (1996). BATSE Observations of the Large-Scale Isotropy of Gamma-Ray Bursts. *The Astrophysical Journal*, **459**, 40+.

Bulik, T., Lamb, D. Q., & Coppi, P. S. (1998). Gamma-Ray Bursts from High-Velocity Neutron Stars. *The Astrophysical Journal*, **505**, 666–687.

Butler, N., Monnelly, G., Ricker, G., Doty, J., Ford, P., Vanderspek, R., Crew, G., Dullighan, A., Lamb, D., & Plucinsky, P. (2002). GRB011130 (XRF011130) second epoch Chandra observations. *GRB Circular Network*, **1272**, 1+.

Cavallo, G. & Rees, M. J. (1978). A qualitative study of cosmic fireballs and gamma-ray bursts. *Monthly Notices of the Royal Astronomical Society*, **183**, 359–365.

Condon, J. J., Cotton, W. D., Greisen, E. W., Yin, Q. F., Perley, R. A., Taylor, G. B., & Broderick, J. J. (1998). The NRAO VLA Sky Survey. *The Astronomical Journal*, **115**, 1693–1716.

Costa, E., Frontera, F., Heise, J., Feroci, M., in 't Zand, J., Fiore, F., Cinti, M. N., dal Fiume, D., Nicastro, L., Orlandini, M., Palazzi, E., Rapisarda, M., Zavattini, G., Jager, R., Parmar, A., Owens, A., Molendi, S., Cusumano, G., Maccarone, M. C., Giarrusso, S., Coletta, A., Antonelli, L. A., Giommi, P., Muller, J. M., Piro,

L., & Butler, R. C. (1997a). Discovery of an X-ray afterglow associated with the gamma-ray burst of 28 February 1997. *Nature*, **387**, 783–785.

Costa, E., Feroci, M., Piro, L., Cinti, M. N., Frontera, F., Zavattini, G., Nicastro, L., Palazzi, E., dal Fiume, D., Orlandini, M., in 't Zand, J., Heise, J., Jager, R., Parmar, A., Owens, A., Molendi, S., Cusumano, G., Maccarone, M. C., Giarrusso, S., Antonelli, L. A., Fiore, F., Giommi, P., Muller, J. M., Salotti, L., Gennaro, G., Stornelli, M., Crisigiovanni, G., Ricci, R., Coletta, A., Butler, R. C., Frail, D. A., & Kulkarni, S. R. (1997b). GRB 970228. *IAU Circular*, **6576**, 1+.

Costa, E., Feroci, M., Frontera, F., Zavattini, G., Nicastro, L., Palazzi, E., Spoliti, G., di Ciolo, L., Coletta, A., D'Andreta, G., Muller, J. M., Jager, R., Heise, J., & in 't Zand, J. (1997c). GRB 970228. *IAU Circular*, **6572**, 1+.

Covino, S., Lazzati, D., Ghisellini, G., Saracco, P., Campana, S., Chincarini, G., di Serego, S., Cimatti, A., Vanzi, L., Pasquini, L., Haardt, F., Israel, G. L., Stella, L., & Vietri, M. (1999). GRB 990510: linearly polarized radiation from a fireball. *Astronomy and Astrophysics*, **348**, L1–L4.

Dickey, J. M. & Lockman, F. J. (1990). H I in the Galaxy. *Annual Reviews of Astronomy and Astrophysics*, **28**, 215–261.

Djorgovski, S. G., Kulkarni, S. R., Bloom, J. S., & Frail, D. A. (1999). GRB 970228: redshift and properties of the host galaxy. *GRB Circular Network*, **289**, 1+.

Djorgovski, S. G., Frail, D. A., Kulkarni, S. R., Bloom, J. S., Odewahn, S. C., & Diercks, A. (2001). The Afterglow and the Host Galaxy of the Dark Burst GRB 970828. *The Astrophysical Journal*, **562**, 654–663.

Dooling, D. & Finckenor, M. (1999). Material Selection Guidelines to Limit Atomic Oxygen Effects on Spacecraft Surfaces, NASA/TP -1999-209260 , Prepared for NASA's Space Environments and Effects (SEE) Program. Technical report, D2 Associates.

Doty, J. P. (1988). The All Sky Monitor for the X-ray Timing Explorer. In *X-ray instrumentation in astronomy II; Proceedings of the Meeting, San Diego, CA, Aug. 15-17, 1988 (A89-40276 17-35). Bellingham, WA, Society of Photo-Optical Instrumentation Engineers, 1988, p. 164-172.*, volume 982, pages 164–172.

Esin, A. A. & Blandford, R. (2000). Dust Echoes from Gamma-Ray Bursts. *The Astrophysical Journal*, **534**, L151–L154.

Feigelson, E. D., Broos, P., Chartas, G., Koch, S. K., Maeda, Y., Sambruna, R., Sanwal, D., Townsley, L., Tsuboi, Y., Wolovitz, J., Miyaji, T., & Ptak, A. (2000). Some Data Analysis Techniques for Chandra ACIS. *AAS/High Energy Astrophysics Division*, **32**, 0+.

Fishman, G. J. & Meegan, C. A. (1995). Gamma-Ray Bursts. *Annual Reviews of Astronomy and Astrophysics*, **33**, 415–458.

Fox, D. W. (2002a). GRB020127: Chandra observations and prospective counterparts. *GRB Circular Network*, **1241**, 1+.

Fox, D. W. (2002b). GRB020127: comparison of Chandra epochs and identification of possible count erparts. *GRB Circular Network*, **1249**, 1+.

Fox, D. W., Price, P. A., Yost, S. A., Burruss, W. R., Tinney, C. G., Begam, M., & Schmidt, B. P. (2002). GRB 020331: candidate optical afterglow. *GRB Circular Network*, **1334**, 1+.

Frail, D. A. (2001). GRB 011130, Radio/X-ray comparison. *GRB Circular Network*, **1207**, 1+.

Frail, D. A., Kulkarni, S. R., Nicastro, S. R., Feroci, M., & Taylor, G. B. (1997). The radio afterglow from the gamma-ray burst of 8 May 1997. *Nature*, **389**, 261–263.

Frail, D. A., Waxman, E., & Kulkarni, S. R. (2000). A 450 Day Light Curve of the Radio Afterglow of GRB 970508: Fireball Calorimetry. *The Astrophysical Journal*, **537**, 191–204.

Frail, D. A., Kulkarni, S. R., Sari, R., Djorgovski, S. G., Bloom, J. S., Galama, T. J., Reichart, D. E., Berger, E., Harrison, F. A., Price, P. A., Yost, S. A., Diercks, A., Goodrich, R. W., & Chaffee, F. (2001). Beaming in Gamma-Ray Bursts: Evidence for a Standard Energy Reservoir. *The Astrophysical Journal*, **562**, L55–L58.

Fruchter, A. S., Thorsett, S. E., Metzger, M. R., Sahu, K. C., Petro, L., Livio, M., Ferguson, H., Pian, E., Hogg, D. W., Galama, T., Gull, T. R., Kouveliotou, C., Macchetto, D., van Paradijs, J., Pedersen, H., & Smette, A. (1999a). Hubble Space Telescope and Palomar Imaging of GRB 990123: Implications for the Nature of Gamma-Ray Bursts and Their Hosts. *The Astrophysical Journal*, **519**, L13–L16.

Fruchter, A. S., Pian, E., Thorsett, S. E., Bergeron, L. E., González, R. A., Metzger, M., Goudfrooij, P., Sahu, K. C., Ferguson, H., Livio, M., Mutchler, M., Petro, L., Frontera, F., Galama, T., Groot, P., Hook, R., Kouveliotou, C., Macchetto, D., van Paradijs, J., Palazzi, E., Pedersen, H., Sparks, W., & Tavani, M. (1999b). The Fading Optical Counterpart of GRB 970228, 6 Months and 1 Year Later. *The Astrophysical Journal*, **516**, 683–692.

Fryer, C. L., Woosley, S. E., & Heger, A. (2001). Pair-Instability Supernovae, Gravity Waves, and Gamma-Ray Transients. *The Astrophysical Journal*, **550**, 372–382.

Galama, T., Groot, P. J., Vanparadijs, J., Kouveliotou, C., Robinson, C. R., Fishman, G. J., Meegan, C. A., Sahu, K. C., Livio, M., Petro, L., Macchetto, F. D., Heise, J., Int Zand, J., Strom, R. G., Telting, J., Rutten, R. G. M., Pettini, M., Tanvir, N., & Bloom, J. (1997). The Decay of Optical Emission from the gamma-Ray Burst GRB970228. *Nature*, **387**, 479+.

Galama, T. J., Vreeswijk, P. M., van Paradijs, J., Kouveliotou, C., Augusteijn, T., Bohnhardt, H., Brewer, J. P., Doublier, V., Gonzalez, J.-F., Leibundgut, B., Lidman, C., Hainaut, O. R., Patat, F., Heise, J., in 't Zand, J., Hurley, K., Groot, P. J., Strom, R. G., Mazzali, P. A., Iwamoto, K., Nomoto, K., Umeda, H., Nakamura, T., Young, T. R., Suzuki, T., Shigeyama, T., Koshut, T., Kippen, M., Robinson, C., de Wildt, P., Wijers, R. A. M. J., Tanvir, N., Greiner, J., Pian, E., Palazzi, E.,

Frontera, F., Masetti, N., Nicastro, L., Feroci, M., Costa, E., Piro, L., Peterson, B. A., Tinney, C., Boyle, B., Cannon, R., Stathakis, R., Sadler, E., Begam, M. C., & Ianna, P. (1998a). An unusual supernova in the error box of the gamma-ray burst of 25 April 1998. *Nature*, **395**, 670–672.

Galama, T. J., Wijers, R. A. M. J., Bremer, M., Groot, P. J., Strom, R. G., Kouveliotou, C., & van Paradijs, J. (1998b). The Radio-to-X-Ray Spectrum of GRB 970508 on 1997 May 21.0 UT. *The Astrophysical Journal*, **500**, L97–+.

Galama, T. J., Briggs, M. S., Wijers, R. A. M., Vreeswijk, P. M., Rol, E., Band, D., van Paradijs, J., Kouveliotou, C., Preece, R. D., Bremer, M., Smith, I. A., Tilanus, R. P. J., de Bruyn, A. G., Strom, R. G., Pooley, G., Castro-Tirado, A. J., Tanvir, N., Robinson, C., Hurley, K., Heise, J., Telting, J., Rutten, R. G. M., Packham, C., Swaters, R., Davies, J. K., Fassia, A., Green, S. F., Foster, M. J., Sagar, R., Pandey, A. K., Nilakshi, Yadav, R. K. S., Ofek, E. O., Leibowitz, E., Ibbetson, P., Rhoads, J., Falco, E., Petry, C., Impey, C., Geballe, T. R., & Bhattacharya, D. (1999). The effect of magnetic fields on gamma-ray bursts inferred from multi-wavelength observations of the burst of 23 January 1999. *Nature*, **398**, 394–399.

Galama, T. J., Tanvir, N., Vreeswijk, P. M., Wijers, R. A. M. J., Groot, P. J., Rol, E., van Paradijs, J., Kouveliotou, C., Fruchter, A. S., Masetti, N., Pedersen, H., Margon, B., Deutsch, E. W., Metzger, M., Armus, L., Klose, S., & Stecklum, B. (2000). Evidence for a Supernova in Reanalyzed Optical and Near-Infrared Images of GRB 970228. *The Astrophysical Journal*, **536**, 185–194.

Garnavich, P., Jha, S., Kirshner, R. P., & Garnavich, P. M. (2001a). GRB011130, optical observations. *GRB Circular Network*, **1179**, 1+.

Garnavich, P., Jha, S., & Kirshner, R. P. (2001b). GRB011130, optical observations. *GRB Circular Network*, **1181**, 1+.

Gnedin, N. Y. & Ostriker, J. P. (1997). Reionization of the Universe and the Early Production of Metals. *The Astrophysical Journal*, **486**, 581+.

Graziani, C. & The HETE Science Team (2002). Astrometric Calibration and Estimate of the Systematic Error in WXM Localizations Obtained By the Chicago Bayesian Method. In *AIP Conf. Proc.: Woods Hole Conference on Gamma-Ray Burst and Afterglow Astronomy 2001, in press*, pages 4+.

Greiner, J., Klose, S., Henden, A. A., Riffeser, A., & Castro-Tirado, A. J. (2001). GRB011130 (=XRF011130), optical observations. *GRB Circular Network*, **1171**, 1+.

Groot, P. J., Galama, T. J., van Paradijs, J., Kouveliotou, C., Wijers, R. A. M. J., Bloom, J., Tanvir, N., Vanderspek, R., Greiner, J., Castro-Tirado, A. J., Gorosabel, J., von Hippel, T., Lehnert, M., Kuijken, K., Hoekstra, H., Metcalfe, N., Howk, C., Conselice, C., Telting, J., Rutten, R. G. M., Rhoads, J., Cole, A., Pisano, D. J., Naber, R., & Schwarz, R. (1998). A Search for Optical Afterglow from GRB 970828. *The Astrophysical Journal*, **493**, L27–+.

Halpern, J. P., Mirabal, N., Gotthelf, E. V., & Kemp, J. (2001). GRB 011130: optical observations of X-ray and radio sources. *GRB Circular Network*, **1208**, 1+.

Harrison, F. A., Bloom, J. S., Frail, D. A., Sari, R., Kulkarni, S. R., Djorgovski, S. G., Axelrod, T., Mould, J., Schmidt, B. P., Wieringa, M. H., Wark, R. M., Subrahmanyan, R., McConnell, D., McCarthy, P. J., Schaefer, B. E., McMahon, R. G., Markze, R. O., Firth, E., Soffitta, P., & Amati, L. (1999). Optical and Radio Observations of the Afterglow from GRB 990510: Evidence for a Jet. *The Astrophysical Journal*, **523**, L121–L124.

Harrison, F. A., Yost, S. A., Sari, R., Berger, E., Galama, T. J., Holtzman, J., Axelrod, T., Bloom, J. S., Chevalier, R., Costa, E., Diercks, A., Djorgovski, S. G., Frail, D. A., Frontera, F., Hurley, K., Kulkarni, S. R., McCarthy, P., Piro, L., Pooley, G. G., Price, P. A., Reichart, D., Ricker, G. R., Shepherd, D., Schmidt, B., Walter, F., & Wheeler, C. (2001). Broadband Observations of the Afterglow of GRB 000926: Observing the Effect of Inverse Compton Scattering. *The Astrophysical Journal*, **559**, 123–130.

Hartmann, D. H. (2002). GRB 020331 optical observations. *GRB Circular Network*, **1318**, 1+.

Heise, J. (2002). X-ray flashes and X-ray rich Gamma Ray Bursts. talk at the 200th AAS meeting.

Heise, J., in't Zand, J., Kippen, R. M., & Woods, P. M. (2001). X-Ray Flashes and X-Ray Rich Gamma Ray Bursts. In *Gamma-ray Bursts in the Afterglow Era*, pages 16+.

Henden, A. (2002). GRB020331 field photometry. *GRB Circular Network*, **1319**, 1+.

Hogg, D. W. & Fruchter, A. S. (1999). The Faint-Galaxy Hosts of Gamma-Ray Bursts. *The Astrophysical Journal*, **520**, 54–58.

Hudec, R., Ceplecha, Z., Spurný, P., Florián, J., Kolář , A., Boček, J., Borovička, J., & Kroll, P. (1999). Real-time and pre-burst optical data for GRBs. *Astronomy and Astrophysics Supplement*, **138**, 591–592.

Hurley, K., Guidorzi, C., Montanari, E., Frontera, F., Cline, T., Mazets, E., & Golenetskii, S. (2001a). IPN triangulation of GRB010612. *GRB Circular Network*, **1065**, 1+.

Hurley, K., Cline, T., Mazets, E., & Golenetskii, S. (2001b). IPN triangulation of GRB010613. *GRB Circular Network*, **1067**, 1+.

Hurley, K., Cline, T., Mitrofanov, I., Anfimov, D., Kozyrev, A., Litvak, M., Sanin, A., Boynton, W., Fellows, C., Harshman, K., Shinohara, C., Starr, R., Ricker, G., Atteia, J.-L., Kawai, N., Lamb, D., Woosley, S., Doty, J., Vanderspek, R., Villasenor, J., Crew, G., Monnelly, G., Butler, N., Jernigan, J. G., Levine, A., Martel, F., Morgan, E., Prigozhin, G., Braga, J., Manchanda, R., Pizzichini, G., Shirasaki, Y., Graziani, C., Matsuoka, M., Tamagawa, T., Torii, K., Sakamoto, T., Yoshida, A., Fenimore, E., Galassi, M., Tavenner, T., Donaghy, T., Boer, M., Olive, J.-F., & Dezalay, J.-P. (2002). IPN triangulation of the short, hard GRB020531 (=H2042). *GRB Circular Network*, **1402**, 1+.

Infante, L., Garnavich, P. M., Stanek, K. Z., & Wyrzykowski, L. (2001). GRB011121: possible redshift, continued decay. *GRB Circular Network*, **1152**, 1+.

Jha, S., Kirshner, R. P., Matheson, T., Garnavich, P. M., Monnelly, G. P., Vanderspek, R. K., & Ricker, G. R. (2001). GRB 011130: magellan spectroscopy. *GRB Circular Network*, **1183**, 1+.

Kato, T., Yamaoka, H., Ishioka, R., & Uemura, M. (2002). GRB 020331 kyoto observation on March 31. *GRB Circular Network*, **1363**, 1+.

Katz, J. I. (1994). Two populations and models of gamma-ray bursts. *The Astrophysical Journal*, **422**, 248–259.

Kawai, N., Urata, Y., Kohama, M., Torii, K., Yoshida, A., Ayani, K., Kawabata, T., Chaya, M., Shibata, H., Sakamoto, K., & Yamauchi, M. (2002). GRB020331 optical observations with RIMOTS. *GRB Circular Network*, **1344**, 1+.

Kinugasa, K., Hashimoto, O., Kambe, E., Urata, Y., Kohama, M., Torii, K., Kawai, N., Yoshida, A., & Yamaoka, H. (2001). GRB011212: optical observations at gunma. *GRB Circular Network*, **1210**, 1+.

Klebesedal, R. W., Strong, I. B., & Olson, R. A. (1973). *The Astrophysical Journal*, **182**, L85.

Klose, S., Dannerbauer, H., Greiner, J., Vrba, F. J., Henden, A., Hartmann, D. H., Snigula, J., Thiele, U., Castro-Tirado, A. J., Gorosabel, J., & Pian, E. (2002). GRB 020331, NIR observations. *GRB Circular Network*, **1317**, 1+.

Kommers, J. M., Lewin, W. H. G., Kouveliotou, C., van Paradijs, J., Pendleton, G. N., Meegan, C. A., & Fishman, G. J. (2000). The Intensity Distribution of Faint Gamma-Ray Bursts Detected with BATSE. *The Astrophysical Journal*, **533**, 696–709.

Kouveliotou, C., Meegan, C. A., Fishman, G. J., Bhat, N. P., Briggs, M. S., Koshut, T. M., Paciesas, W. S., & Pendleton, G. N. (1993). Identification of two classes of gamma-ray bursts. *The Astrophysical Journal*, **413**, L101–L104.

Krimm, H. A., Vanderspek, R. K., & Ricker, G. R. (1996). Searches for optical counterparts of BATSE gamma-ray bursts with the Explosive Transient Camera. *Astronomy and Astrophysics Supplement*, **120**, C251–+.

Kulkarni, S. R., Djorgoski, S. G., Ramaprakash, A. N., Goodrich, R., Bloom, J. S., Adelberger, K. L., Kundic, T., Lubin, L., Frail, D. A., Frontera, F., Feroci, M., Nicastro, L., Barth, A. J., Davis, M., Filippenko, A. V., & Newman, J. (1998a). Identification of a host galaxy at redshift Z = 3.42 for the gamma-ray burst of 14 December 1997. *Nature*, **393**, 35–39.

Kulkarni, S. R., Frail, D. A., Wieringa, M. H., Ekers, R. D., Sadler, E. M., Wark, R. M., Higdon, J. L., Phinney, E. S., & Bloom, J. S. (1998b). Radio emission from the unusual supernova 1998bw and its association with the gamma-ray burst of 25 April 1998. *Nature*, **395**, 663–669.

Kulkarni, S. R., Berger, E., Bloom, J. S., Chaffee, F. H., Diercks, A. H., Djorgovski, S. G., Frail, D. A., Galama, T. J., Goodrich, R., Harrison, F. A., Sari, R., & Yost, S. A. (2000). Afterglows of gamma-ray bursts. In *Proc. SPIE Vol. 4005, p. 9-21, Discoveries and Research Prospects from 8- to 10-Meter-Class Telescopes, Jacqueline Bergeron; Ed.*, volume 4005, pages 9–21.

Lamb, D. Q. (1995). The Distance Scale to Gamma-Ray Bursts. *Publications of the Astronomical Society of the Pacific*, **107**, 1152+.

Lamb, D. Q. & Reichart, D. E. (2000). Gamma-Ray Bursts as a Probe of the Very High Redshift Universe. *The Astrophysical Journal*, **536**, 1–18.

Lazzati, D., Ramirez-Ruiz, E., & Rees, M. J. (2002). Soft X-Ray Emission Lines in the Early Afterglow of Gamma-Ray Bursts. *The Astrophysical Journal*, **572**, L57–L60.

Lloyd, N. M. & Petrosian, V. . (1999). Distribution of Spectral Characteristics and the Cosmological Evolution of Gamma-Ray Bursts. *The Astrophysical Journal*, **511**, 550–561.

Lloyd, N. M. & Petrosian, V. . (2000). Synchrotron Radiation as the Source of Gamma-Ray Burst Spectra. *The Astrophysical Journal*, **543**, 722–732.

Lloyd-Ronning, N. M. & Petrosian, V. . (2002). Interpreting the Behavior of Time-resolved Gamma-Ray Burst Spectra. *The Astrophysical Journal*, **565**, 182–194.

MacFadyen, A. I. & Woosley, S. E. (1999). Collapsars: Gamma-Ray Bursts and Explosions in "Failed Supernovae". *The Astrophysical Journal*, **524**, 262–289.

Meegan, C. A., Pendleton, G. N., Briggs, M. S., Kouveliotou, C., Koshut, T. M., Lestrade, J. P., Paciesas, W. S., McCollough, M. L., Brainerd, J. J., Horack, J. M., Hakkila, J., Henze, W., Preece, R. D., Mallozzi, R. S., & Fishman, G. J. (1996). The Third BATSE Gamma-Ray Burst Catalog. *The Astrophysical Journal Supplement*, **106**, 65+.

Meszaros, P. & Rees, M. J. (1993). Relativistic fireballs and their impact on external matter - Models for cosmological gamma-ray bursts. *The Astrophysical Journal*, **405**, 278–284.

Meszaros, P. & Rees, M. J. (1997). Optical and Long-Wavelength Afterglow from Gamma-Ray Bursts. *The Astrophysical Journal*, **476**, 232+.

Meszaros, P., Laguna, P., & Rees, M. J. (1993). Gasdynamics of relativistically expanding gamma-ray burst sources - Kinematics, energetics, magnetic fields, and efficiency. *The Astrophysical Journal*, **415**, 181–190.

Metzger, M. R., Djorgovski, S. G., Kulkarni, S. R., Steidel, C. C., Adelberger, K. L., Frail, D. A., Costa, E., & Frontera, F. (1997). Spectral constraints on the redshift of the optical counterpart to the gamma-ray burst of 8 May 1997. *Nature*, **387**, 878–880.

Mirabal, N. & Halpern, J. P. (2001a). GRB 011130: optical observations of Chandra sources. *GRB Circular Network*, **1186**, 1+.

Mirabal, N. & Halpern, J. P. (2001b). GRB 011130: optical observations of Chandra sources. *GRB Circular Network*, **1187**, 1+.

Monnelly, G., Butler, N., Ricker, G., Ford, P., Vanderspek, R., & Lamb, D. (2001). GRB011130 (=XRF011130): further analysis of Chandra target of. *GRB Circular Network*, **1190**, 1+.

Monnelly, G., Dullighan, A., Butler, N., Vanderspek, R., & Ricker, G. (2002). GRB020331: optical observations of afterglow candidate. *GRB Circular Network*, **1339**, 1+.

Monnelly, G., Villasenor, J., Jernigan, G., Prighozin, G., Vanderspek, R., Crew, G., Doty, J., Ricker, G., & Levine, A. (2002). HETE Soft X-ray Camera Imaging: Calibration, Performance, and Sensitivity. In *AIP Conf. Proc.: Woods Hole Conference on Gamma-Ray Burst and Afterglow Astronomy 2001, in press*, pages 4+.

Narayan, R., Paczynski, B., & Piran, T. (1992). Gamma-ray bursts as the death throes of massive binary stars. *The Astrophysical Journal*, **395**, L83–L86.

Ohta, K. & Akiyama, M. (2002). GRB02033 NIR observation at KPNO. *GRB Circular Network*, **1320**, 1+.

Paciesas, W. S., Meegan, C. A., Pendleton, G. N., Briggs, M. S., Kouveliotou, C., Koshut, T. M., Lestrade, J. P., McCollough, M. L., Brainerd, J. J., Hakkila, J., Henze, W., Preece, R. D., Connaughton, V., Kippen, R. M., Mallozzi, R. S., Fishman, G. J., Richardson, G. A., & Sahi, M. (1999). The Fourth BATSE Gamma-Ray Burst Catalog (Revised). *The Astrophysical Journal Supplement*, **122**, 465–495.

Paczynski, B. (1986). Gamma-ray bursters at cosmological distances. *The Astrophysical Journal*, **308**, L43–L46.

Paczynski, B. (1998). Are Gamma-Ray Bursts in Star-Forming Regions? *The Astrophysical Journal*, **494**, L45–+.

Paczynski, B. & Rhoads, J. E. (1993). Radio Transients from Gamma-Ray Bursters. *The Astrophysical Journal*, **418**, L5–+.

Panaitescu, A., Wen, L., Laguna, P., & Meszaros, P. (1997). Impact of Relativistic Fireballs on External Matter: Numerical Models of Cosmological Gamma-Ray Bursts. *The Astrophysical Journal*, **482**, 942+.

Phinney, E. S. (1991). The rate of neutron star binary mergers in the universe - Minimal predictions for gravity wave detectors. *The Astrophysical Journal*, **380**, L17–L21.

Pian, E., Amati, L., Antonelli, L. A., Butler, R. C., Costa, E., Cusumano, G., Danziger, J., Feroci, M., Fiore, F., Frontera, F., Giommi, P., Masetti, N., Muller, J. M., Nicastro, L., Oosterbroek, T., Orlandini, M., Owens, A., Palazzi, E., Parmar, A., Piro, L., in't Zand, J. J. M., Castro-Tirado, A., Coletta, A., Dal Fiume, D., Del Sordo, S., Heise, J., Soffitta, P., & Torroni, V. (2000). BEPPOSAX Observations of GRB 980425: Detection of the Prompt Event and Monitoring of the Error Box. *The Astrophysical Journal*, **536**, 778–787.

Piran, T. (1994). Fireballs. In *AIP Conf. Proc. 307: Gamma-Ray Bursts*, pages 495+.

Piro, L., Costa, E., Feroci, M., Frontera, F., Amati, L., dal Fiume, D., Antonelli, L. A., Heise, J., in 't Zand, J., Owens, A., Parmar, A. N., Cusumano, G., Vietri, M., & Perola, G. C. (1999). The X-Ray Afterglow of the Gamma-Ray Burst of 1997 May 8:Spectral Variability and Possible Evidence of an Iron Line. *The Astrophysical Journal*, **514**, L73–L77.

Piro, L., Garmire, G., Garcia, M., Stratta, G., Costa, E., Feroci, M., Mészáros, P., Vietri, M., Bradt, H., Frail, D., Frontera, F., Halpern, J., Heise, J., Hurley, K., Kawai, N., Kippen, R. M., Marshall, F., Murakami, T., Sokolov, V. V., Takeshima, T., & Yoshida, A. (2000). Observation of X-ray Lines from a Gamma-Ray Burst (GRB991216): Evidence of Moving Ejecta from the Progenitor. *Science*, **290**, 955–958.

Podsiadlowski, P., Rees, M. J., & Ruderman, M. (1995). Gamma-ray bursts and the structure of the Galactic halo. *Monthly Notices of the Royal Astronomical Society*, **273**, 755–771.

Preece, R. D., Briggs, M. S., Mallozzi, R. S., Pendleton, G. N., Paciesas, W. S., & Band, D. L. (2000). The BATSE Gamma-Ray Burst Spectral Catalog. I. High Time Resolution Spectroscopy of Bright Bursts Using High Energy Resolution Data. *The Astrophysical Journal Supplement*, **126**, 19–36.

Price, P. A. & Begam, M. C. (2002). GRB 020331: optical observations. *GRB Circular Network*, **1316**, 1+.

Price, P. A., Kulkarni, S. R., Berger, E., Djorgovski, S. G., Frail, D. A., Mahabal, A., Fox, D. W., Harrison, F. A., Bloom, J. S., Yost, S. A., Reichart, D. E., Henden, A. A., Ricker, G. R., van der Spek, R., Hurley, K., Atteia, J.-L., Kawai, N., Fenimore, E., & Graziani, C. (2002a). GRB 010921: Discovery of the First High Energy Transient Explorer Afterglow. *The Astrophysical Journal*, **571**, L121–L125.

Price, P. A., Tinney, C. G., & Schmidt, B. P. (2002b). GRB 020331: NIR observations. *GRB Circular Network*, **1322**, 1+.

Rees, M. J. & Meszaros, P. (1992). Relativistic fireballs - Energy conversion and time-scales. *Monthly Notices of the Royal Astronomical Society*, **258**, 41P–43P.

Rees, M. J. & Meszaros, P. (1994). Unsteady outflow models for cosmological gamma-ray bursts. *The Astrophysical Journal*, **430**, L93–L96.

Reeves, J. N., Watson, D., Osborne, J. P., Pounds, K. A., O'Brien, P. T., Short, A. D. T., Turner, M. J. L., Watson, M. G., Mason, K. O., Ehle, M., & Schartel, N. (2002). The signature of supernova ejecta in the X-ray afterglow of the γ-ray burst 011211. *Nature*, **416**, 512–515.

Reichart, D. & Yost, S. (2002). Turning to the Dark Side: Evidence for Circumburst Extinction of Gamma-Ray Bursts with Dark Optical Afterglows. *The Astrophysical Journal, submited (astro-ph/0107545)*.

Reichart, D. E. (1999). GRB 970228 Revisited: Evidence for a Supernova in the Light Curve and Late Spectral Energy Distribution of the Afterglow. *The Astrophysical Journal*, **521**, L111–L115.

Reichart, D. E. (2001). Light Curves and Spectra of Dust Echoes from Gamma-Ray Bursts and Their Afterglows: Continued Evidence That GRB 970228 Is Associated with a Supernova. *The Astrophysical Journal*, **554**, 643–659.

Reichart, D. E. & Price, P. A. (2002). Evidence for a Molecular Cloud Origin of Gamma-Ray Bursts: Implications for the Nature of Star Formation in the Universe. *The Astrophysical Journal*, **565**, 174–181.

Ricker, G. (2001a). GRB010213 detected by HETE. *GRB Circular Network*, **934**, 1+.

Ricker, G. (2001b). GRB010326B: localization by HETE (2nd GRB for this date). *GRB Circular Network*, **1018**, 1+.

Ricker, G., Lamb, D., Woosley, S., Vanderspek, R., Crew, G., Doty, J., Monnelly, G., Villasenor, J., Butler, N., Cline, T., Jernigan, J. G., Levine, A., Martel, F., Morgan, E., Pizzichini, G., Prigozhin, G., Kawai, N., Matsuoka, M., Shirasaki, Y., Tamagawa, T., Torii, K., Sakamoto, T., Yoshida, A., Fenimore, E., Galassi, M., Graziani, C., Atteia, J.-L., Boer, M., Olive, J.-F., Dezalay, J.-P., & Hurley, K. (2001a). GRB010629: A burst localized by HETE. *GRB Circular Network*, **1075**, 1+.

Ricker, G., Lamb, D., Woosley, S., Crew, G., Vanderspek, R., Doty, J., Monnelly, G., Villasenor, J., Butler, N., Cline, T., Jernigan, J. G., Levine, A., Martel, F., Morgan, E., Prigozhin, G., Braga, J., Manchanda, R., Pizzichini, G., Kawai, N., Matsuoka, M., Shirasaki, Y., Tamagawa, T., Torii, K., Sakamoto, T., Yoshida, A., Fenimore, E., Galassi, M., Tavenner, T., Donaghy, T., Graziani, C., Atteia, J.-L., Boer, M., Olive, J.-F., Dezalay, J.-P., & Hurley, K. (2001b). GRB010928(=H1770): localization of a long GRB by HETE. *GRB Circular Network*, **1103**, 1+.

Ricker, G., Lamb, D., Woosley, S., Vanderspek, R., Crew, G., Doty, J., Monnelly, G., Villasenor, J., Butler, N., Cline, T., Jernigan, J. G., Levine, A., Martel, F., Morgan, E., Prigozhin, G., Braga, J., Manchanda, R., Pizzichini, G., Kawai, N., Matsuoka, M., Shirasaki, Y., Tamagawa, T., Torii, K., Sakamoto, T., Yoshida, A., Fenimore, E., Galassi, M., Donaghy, T., Graziani, C., Atteia, J.-L., Boer, M., Olive, J.-F., Dezalay, J.-P., & Hurley, K. (2001c). GRB011130 (=H1864): an X-ray rich GRB detected by HETE. *GRB Circular Network*, **1165**, 1+.

Ricker, G., Ford, P., Monnelly, G., Butler, N., Vanderspek, R., Lamb, D., & Vanderspek, R. (2001d). GRB011130 (XRF011130) Chandra observations. *GRB Circular Network*, **1185**, 1+.

Ricker, G., Lamb, D., Woosley, S., Butler, N., Crew, G., Doty, J., Monnelly, G., Prigozhin, G., Vanderspek, R., Villasenor, J., Cline, T., Jernigan, J. G., Levine, A., Martel, F., Morgan, E., Braga, J., Manchanda, R., Pizzichini, G., Graziani, C., Kawai, N., Matsuoka, M., Shirasaki, Y., Tamagawa, T., Torii, K., Sakamoto, T., Yoshida, A., Fenimore, E., Galassi, M., Tavenner, T., Donaghy, T., Atteia, J.-L., Boer, M., Olive, J.-F., Dezalay, J.-P., & Hurley, K. (2001e). GRB011130 (=XRF011130): revised localization of an X-ray. *GRB Circular Network*, **1169**, 1+.

Ricker, G., Lamb, D., Woosley, S., Vanderspek, R., Butler, N., Crew, G., Doty, J., Monnelly, G., Prigozhin, G., Villasenor, J., Cline, T., Jernigan, J. G., Levine, A., Martel, F., Morgan, E., Braga, J., Manchanda, R., Pizzichini, G., Graziani, C., Shirasaki, Y., Kawai, N., Matsuoka, M., Tamagawa, T., Torii, K., Sakamoto, T., Yoshida, A., Fenimore, E., Galassi, M., Tavenner, T., Donaghy, T., Atteia, J.-L., Boer, M., Olive, J.-F., Dezalay, J.-P., & Hurley, K. (2001f). GRB011130 (=XRF011130): second revised localization by HETE. *GRB Circular Network*, **1178**, 1+.

Ricker, G., Lamb, D., Woosley, S., Butler, N., Crew, G., Doty, J., Monnelly, G., Prigozhin, G., Vanderspek, R., Villasenor, J., Cline, T., Jernigan, J. G., Levine,

A., Martel, F., Morgan, E., Braga, J., Manchanda, R., Pizzichini, G., Kawai, N., Matsuoka, M., Shirasaki, Y., Tamagawa, T., Torii, K., Sakamoto, T., Yoshida, A., Fenimore, E., Galassi, M., Tavenner, T., Graziani, C., Donaghy, T., Atteia, J.-L., Boer, M., Olive, J.-F., & Dezalay, J.-P. (2001g). GRB011212 (=H10001): an X-ray rich GRB detected by HETE. *GRB Circular Network*, **1194**, 1+.

Ricker, G., Lamb, D., Woosley, S., Vanderspek, R., Crew, G., Doty, J., Monnelly, G., Villasenor, J., Butler, N., Cline, T., Jernigan, J. G., Levine, A., Martel, F., Morgan, E., Prigozhin, G., Braga, J., Manchanda, R., Pizzichini, G., Kawai, N., Matsuoka, M., Shirasaki, Y., Tamagawa, T., Torii, K., Sakamoto, T., Yoshida, A., Fenimore, E., Galassi, M., Donaghy, T., Graziani, C., Atteia, J.-L., Boer, M., Olive, J.-F., Dezalay, J.-P., & Hurley, K. (2001h). H1761: A Bright GRB Detected by HETE. *GRB Circular Network*, **1096**, 1+.

Ricker, G., Atteia, J.-L., Kawai, N., Lamb, D., Woosley, S., Crew, G., Vanderspek, R., Doty, J., Monnelly, G., Villasenor, J., Butler, N., Cline, T., Jernigan, J. G., Levine, A., Martel, F., Morgan, E., Prigozhin, G., Braga, J., Manchanda, R., Pizzichini, G., Matsuoka, M., Shirasaki, Y., Tamagawa, T., Torii, K., Sakamoto, T., Yoshida, A., Fenimore, E., Galassi, M., Tavenner, T., Donaghy, T., Graziani, C., Boer, M., Olive, J.-F., Dezalay, J.-P., & Hurley, K. (2002a). GRB020124(=H1896): localization of a long GRB by HETE. *GRB Circular Network*, **1220**, 1+.

Ricker, G., Atteia, J.-L., Kawai, N., Lamb, D., Woosley, S., Crew, G., Vanderspek, R., Doty, J., Monnelly, G., Villasenor, J., Butler, N., Cline, T., Jernigan, J. G., Levine, A., Martel, F., Morgan, E., Prigozhin, G., Braga, J., Manchanda, R., Pizzichini, G., Matsuoka, M., Shirasaki, Y., Tamagawa, T., Torii, K., Sakamoto, T., Yoshida, A., Fenimore, E., Galassi, M., Tavenner, T., Donaghy, T., Graziani, C., Boer, M., Olive, J.-F., Dezalay, J.-P., & Hurley, K. (2002b). GRB020127(=H1902): localization of a double-peaked GRB by HETE. *GRB Circular Network*, **1229**, 1+.

Ricker, G., Atteia, J.-L., Kawai, N., Lamb, D., Woosley, S., Villasenor, J., Vander-

spek, R., Crew, G., Doty, J., Monnelly, G., Butler, N., Cline, T., Jernigan, J. G., Levine, A., Martel, F., Morgan, E., Prigozhin, G., Braga, J., Manchanda, R., Pizzichini, G., Matsuoka, M., Shirasaki, Y., Tamagawa, T., Torii, K., Sakamoto, T., Yoshida, A., Fenimore, E., Galassi, M., Tavenner, T., Donaghy, T., Graziani, C., Boer, M., Olive, J.-F., Dezalay, J.-P., Lestrade, P., & Hurley, K. (2002c). GRB020305 (=H1939): localization of a GRB by HETE. *GRB Circular Network*, **1262**, 1+.

Ricker, G., Atteia, J.-L., Kawai, N., Lamb, D., Woosley, S., Villasenor, J., Vanderspek, R., Crew, G., Doty, J., Monnelly, G., Butler, N., Cline, T., Jernigan, J. G., Levine, A., Martel, F., Morgan, E., Prigozhin, G., Braga, J., Manchanda, R., Pizzichini, G., Matsuoka, M., Shirasaki, Y., Tamagawa, T., Torii, K., Sakamoto, T., Yoshida, A., Fenimore, E., Galassi, M., Tavenner, T., Donaghy, T., Graziani, C., Boer, M., Olive, J.-F., Dezalay, J.-P., & Hurley, K. (2002d). GRB020317 (=H1959): localization by HETE of a low fluence GRB. *GRB Circular Network*, **1280**, 1+.

Ricker, G., Atteia, J.-L., Kawai, N., Lamb, D., Woosley, S., Vanderspek, R., Villasenor, J., Crew, G., Doty, J., Monnelly, G., Butler, N., Cline, T., Jernigan, J. G., Levine, A., Martel, F., Morgan, E., Prigozhin, G., Braga, J., Manchanda, R., Pizzichini, G., Shirasaki, Y., Matsuoka, M., Tamagawa, T., Torii, K., Sakamoto, T., Yoshida, A., Fenimore, E., Galassi, M., Tavenner, T., Donaghy, T., Graziani, C., Boer, M., Olive, J.-F., Dezalay, J.-P., & Hurley, K. (2002e). GRB020331(=H1963): the "Easter" burst detected by HETE. *GRB Circular Network*, **1315**, 1+.

Ricker, G., Atteia, J.-L., Kawai, N., Lamb, D., Woosley, S., Doty, J., Vanderspek, R., Villasenor, J., Crew, G., Monnelly, G., Butler, N., Cline, T., Jernigan, J. G., Levine, A., Martel, F., Morgan, E., Prigozhin, G., Braga, J., Manchanda, R., Pizzichini, G., Shirasaki, Y., Graziani, C., Matsuoka, M., Tamagawa, T., Torii, K., Sakamoto, T., Yoshida, A., Fenimore, E., Galassi, M., Tavenner, T., Donaghy, T., Boer, M., Olive, J.-F., Dezalay, J.-P., & Hurley, K. (2002f). GRB020531(=H2042): a short, hard burst localized by HETE. *GRB Circular Network*, **1399**, 1+.

Ricker, G., Lamb, D., Hurley, K., Vanderspek, R., & Woosley, S. (2002g). The High Energy Transient Explorer (HETE): Mission and Science Overview. In *AIP Conf. Proc.: Woods Hole Conference on Gamma-Ray Burst and Afterglow Astronomy 2001, in press*, pages 4+.

Ricker G., Butler N., Vanderspek R., Crew G., Doty J., Monnelly G., Villasenor J., Cline T., Jernigan J.G., Levine A., Martel F., Morgan E., Prigozhin G., Braga J., Manchanda R., Pizzichini G., Kawai N., Matsuoka M., Shirasaki Y., Tamagawa T., Torri K., Sakamoto T., Yoshida A., Fenimore E., Galassi M., Tavenner T., Donaghy T., Graziani C., Atteia J.-L., Boer M., Olive J.-F., & Dezalay J.-P. and Hurley K. (2001). GRB011019: A faint, X-ray rich GRB localized by HETE. *GRB Circular Network*, **1109**, 1+.

Rybicki, G. & Lightman, A. (1979). *Radiative processes in astrophysics.* John Wiley & Sons.

Sahu, K. C., Livio, M., Petro, L., Macchetto, F. D., van Paradijs, J., Kouveliotou, C., Fishman, G. J., Meegan, C. A., Groot, P. J., & Galama, T. (1997). The optical counterpart to gamma-ray burst GRB 970228 observed using the Hubble Space Telescope. *Nature*, **387**, 476–478.

Saracco, P., Covino, S., Ghisellini, G., Fugazza, D., Masetti, N., Palazzi, E., Pian, E., Antonelli, A., Fiore, F., Israel, G. L., Stella, L., & Desidera, S. (2001). GRB 011212: optical observation at asiago. *GRB Circular Network*, **1205**, 1+.

Sari, R. (1997). Hydrodynamics of Gamma-Ray Burst Afterglow. *The Astrophysical Journal*, **489**, L37–+.

Sari, R., Narayan, R., & Piran, T. (1996). Cooling Timescales and Temporal Structure of Gamma-Ray Bursts. *The Astrophysical Journal*, **473**, 204+.

Sari, R., Piran, T., & Narayan, R. (1998). Spectra and Light Curves of Gamma-Ray Burst Afterglows. *The Astrophysical Journal*, **497**, L17–+.

Sari, R., Piran, T., & Halpern, J. P. (1999). Jets in Gamma-Ray Bursts. *The Astrophysical Journal*, **519**, L17–L20.

Schaefer, B. E. (1992). Severe new limits on extragalactic models of gamma-ray bursts. In *Gamma-Ray Bursts - Observations, Analyses and Theories*, pages 107–112.

Schmidt, M. (2001). Luminosity Function of Gamma-Ray Bursts Derived without Benefit of Redshifts. *The Astrophysical Journal*, **552**, 36–41.

Shirasaki, Y., Kawai, N., Yoshida, A., Matsuoka, M., Tamagawa, T., Torii, K., Sakamoto, T., Fenimore, E., Galassi, M., Vanderspek, R., & the HETE-2 Science Team (2002). Astrometric Calibration and Estimate of the Systematic Error in HETE WXM Localizations Obtained by the RIKEN Cross Correlation Method. In *AIP Conf. Proc.: Woods Hole Conference on Gamma-Ray Burst and Afterglow Astronomy 2001, in press*, pages 3+.

Shklovskii, I. S. & Mitrofanov, I. G. (1985). On the astronomical nature of the sources of gamma-ray bursts. *Monthly Notices of the Royal Astronomical Society*, **212**, 545–551.

Stanek, K. Z., Garnavich, P. M., Kaluzny, J., Pych, W., & Thompson, I. (1999). BVRI Observations of the Optical Afterglow of GRB 990510. *The Astrophysical Journal*, **522**, L39–L42.

Strohmayer, T. E., Fenimore, E. E., Murakami, T., & Yoshida, A. (1998). X-Ray Spectral Characteristics of GINGA Gamma-Ray Bursts. *The Astrophysical Journal*, **500**, 873+.

Torii, K., Kato, T., Yamaoka, H., & Yoshida, A. (2002). GRB 020124: optical observations. *GRB Circular Network*, **1378**, 1+.

van Paradijs, J., Groot, P. J., Galama, T., Kouveliotou, C., Strom, R. G., Telting, J., Rutten, R. G. M., Fishman, G. J., Meegan, C. A., Pettini, M., Tanvir, N., Bloom, J., Pedersen, H., Nordgaard-Nielsen, H. U., Linden-Vornle, M., Melnick,

J., van der Steene, G., Bremer, M., Naber, R., Heise, J., in 't Zand, J., Costa, E., Feroci, M., Piro, L., Frontera, F., Zavattini, G., Nicastro, L., Palazzi, E., Bennet, K., Hanlon, L., & Parmar, A. (1997). Transient optical emission from the error box of the gamma-ray burst of 28 February 1997. *Nature*, **386**, 686–689.

Vanderspek, R., Villaseñor, J., Doty, J., Jernigan, J. G., Levine, A., Monnelly, G., & Ricker, G. R. . (1999). GRB observations with the HETE soft X-ray cameras. *Astronomy and Astrophysics Supplement*, **138**, 565–566.

Vietri, M. (1997). The Soft X-Ray Afterglow of Gamma-Ray Bursts, A Stringent Test for the Fireball Model. *The Astrophysical Journal*, **478**, L9–+.

Vietri, M. & Stella, L. (1998). A Gamma-Ray Burst Model with Small Baryon Contamination. *The Astrophysical Journal*, **507**, L45–L48.

Vietri, M. & Stella, L. (1999). Supranova Events from Spun-up Neutron Stars: an Explosion in Search of an Observation. *The Astrophysical Journal*, **527**, L43–L46.

Villasenor, J., Dill, R., Monnelly, G., Vanderspek, R., Ricker, G., Kissel, S., & Prigozhin, G. (2002). An Overview of the HETE Soft X-ray Camera. In *AIP Conf. Proc.: Woods Hole Conference on Gamma-Ray Burst and Afterglow Astronomy 2001, in press*, pages 4+.

Waxman, E. (1997). Angular Size and Emission Timescales of Relativistic Fireballs. *The Astrophysical Journal*, **491**, L19–+.

Waxman, E., Kulkarni, S. R., & Frail, D. A. (1998). Implications of the Radio Afterglow from the Gamma-Ray Burst of 1997 May 8. *The Astrophysical Journal*, **497**, 288+.

Wijers, R. A. M. J., Vreeswijk, P. M., Galama, T. J., Rol, E., van Paradijs, J., Kouveliotou, C., Giblin, T., Masetti, N., Palazzi, E., Pian, E., Frontera, F., Nicastro, L., Falomo, R., Soffitta, P., & Piro, L. (1999). Detection of Polarization in the Afterglow of GRB 990510 with the ESO Very Large Telescope. *The Astrophysical Journal*, **523**, L33–L36.

Woosley, S. E. (1993). Gamma-ray bursts from stellar mass accretion disks around black holes. *The Astrophysical Journal*, **405**, 273–277.

Yoshida, A., Namiki, M., Otani, C., Kawai, N., Murakami, T., Ueda, Y., Shibata, R., & Uno, S. (1999). What did ASCA see in the GRB 970828 afterglow? *Astronomy and Astrophysics Supplement*, **138**, 433–434.